

UNIVERSITÀ DELLA CALABRIA



UNIVERSITA' DELLA CALABRIA

Dipartimento di Fisica

Dottorato di Ricerca in

Scienze e Tecnologie Fisiche, Chimiche e dei Materiali in convenzione con il CNR

CICLO

XXXI

**ADVANCED PLASMONIC DEVICES: ENHANCEMENT OF THE PROPERTIES
OF ORGANIC AND PEROVSKITE SOLAR CELLS THROUGH
GOLD NANOPARTICLES**

Settore Scientifico Disciplinare CHIM/02

Coordinatore: Ch.mo Prof. Vincenzo Carbone

Firma Vincenzo Carbone

Supervisori: Dott. Roberto Termine

Firma Roberto Termine

Prof. Attilio Golemme

Firma Attilio Golemme

Dottorando: Dott. Alessandro Servidio

Firma Alessandro Servidio

Contents

Abstract	i
Sintesi	iii
List of abbreviations	v
Introduction	1
Thesis outline	3
References	5
Chapter 1. METALLIC NANOSTRUCTURES: PLASMONIC PROPERTIES AND SYNTHESIS	
1. 1 Introduction	6
1.2 Volume, surface and localized surface plasmons	7
1.3 Nanofabrication of plasmonic gold nanoparticles	15
1.3.1 Synthesis of gold nanoplates	17
1.3.2 Synthesis of gold-silica core-shell nanoparticles	20
1.4 References	23
Chapter 2. ORGANIC AND PEROVSKITE SOLAR CELLS INTEGRATING PLASMONIC NANOSTRUCTURES	
2.1 Introduction	26
2.2 Characterization of photovoltaic cells	27
2.2.1 Photovoltaic parameters	27
2.2.2 Quantum efficiency	31
2.2.3 Equivalent circuit of organic solar cells	32
2.3 Inorganic and organic semiconductors	34
2.4 Architectures of organic solar cells	36
2.4.1 Single Layer	36
2.4.2 Bilayer heterojunction	38
2.4.3 Bulk heterojunction	39

2.5 Working mechanism of bulk heterojunction organic solar cells	41
2.5.1 Photons absorption and excitons generation	42
2.5.2 Exciton diffusion	42
2.5.3 Excitons dissociation at the D/A interface	44
2.5.4 Charge transport to the electrodes	44
2.5.5 Charge collection at the electrodes	45
2.6 Plasmonic enhanced organic solar cells	47
2.6.1 Plasmonic light trapping in organic solar cells	48
2.6.2 Beyond light harvesting effect induced by plasmonic nanoparticle in organic solar cells	50
2.6.3 Plasmonic organic solar cells	52
2.7 Perovskite for photovoltaic applications	56
2.7.1 Structure and composition	56
2.7.2 Optoelectronic properties	57
2.8 Perovskite thin film deposition	59
2.8.1 Co-Evaporation method	60
2.8.2 One-Step Solution methods	60
2.8.3 Two-Step Solution methods	62
2.9 Perovskite solar cell architectures	62
2.10 Hysteresis	65
2.11 Plasmonic light trapping enhancement in perovskite solar cells	66
2.11.1 Effects of plasmonic nanoparticles incorporation in perovskite solar cells	68
2.12 References	71

Chapter 3. *PLASMONIC ANISOTROPIC GOLD NANOPARTICLES: SYNTHESIS AND CHARACTERIZATION*

3. 1 Introduction	81
3.2 Anisotropic Au@PVP nanoparticles	81
3.2.1 Synthetic procedure	81
3.2.2 Purification procedure	82
3.2.3 Nanoparticles characterizations	82
3.3.4 Tuning the size of Au@PVP nanoparticles	84

3.3 Synthesis of Au@SiO₂ nanoparticles from Au@PVP nanoparticles	85
3.3.1 Synthesis, purification and characterization of Au@SiO ₂ : initial protocol	86
3.3.2 Synthesis, purification and characterization of Au@SiO ₂ : a modified protocol	91
3.4 References	95
Chapter 4. <i>PLASMONIC ORGANIC SOLAR CELLS</i>	
4. 1 Introduction	96
4.2 Optimization of the protocol for the fabrication of the reference cells	96
4.3 Optimization of the Au@PVP nanoparticles incorporation in PEDOT:PSS thin film	101
4.4 Effect of Au@PVP nanoparticles concentration in PEDOT:PSS on the performance of the devices	103
4.5 Incorporation of Au@PVP and Au@SiO ₂ nanoparticles at PEDOT:PSS/P3HT:PC ₆₁ BM interface	110
4.6 References	116
CHAPTER 5. <i>PLASMONIC PEROVSKITE SOLAR CELLS</i>	
5.1 Introduction	117
5.2 Plasmonic perovskite solar cells integrating anisotropic Au@PVP nanoparticles in PEDOT:PSS	119
5.2.1 Device fabrication	119
5.2.2 Characterization and results	120
5.3 Plasmonic perovskite solar cells integrating anisotropic Au@PVP nanoparticles at the poly-TPD/perovskite interface	126
5.3.1 Device fabrication	126
5.3.2 Characterization and results	127
5.4 References	133
Chapter 6. <i>CONCLUSION AND FUTURE WORKS</i>	134
List of publications and conference presentations	138

Abstract

The ability to meet global energy needs through renewable sources by eliminating dependence on fossil resources is one of the main priorities for the sustainable development of humanity. Silicon based photovoltaic technology allows conversion efficiencies of up to 26%, but the high manufacturing costs of solar panels greatly limit their application. The search for alternative solutions has led to the development of solar cells based on organic semiconductors and hybrid organic-inorganic perovskites. The use of inexpensive materials, the production through solutions-based and low temperature processes compatible with large-scale production techniques also on flexible substrates, make these cells particularly interesting for the reduced fabrication costs and for potential applications in portable devices or as building integrated photovoltaics. The main obstacle to the commercialization of organic solar cells is the low efficiency (about 10% for the most efficient cells) determined by the reduced amount of light absorbed by the active layer, whose thickness is limited due to the low charge mobility and restricted diffusion length of excitons in organic semiconductors. On the other hand, perovskite-based devices reach an efficiency of more than 22%, but contain lead, which is a toxic element.

The studies reported in the present work concern the integration of plasmonic nanoparticles in organic and perovskite solar cells and the investigation of their effects on the properties and performances of the devices. The introduction of plasmonic nanoparticles in solar cells allows enhancing the amount of light absorbed by the active layer without increasing its thickness, exploiting plasmonic effects such as light-scattering and near-field enhancement. This strategy is particularly useful in organic solar cells where efficiency can not be improved by increasing the thickness of the active layer; furthermore, it can be used to compensate the light absorption losses in perovskite cells produced with a thin active layer with the aim to reduce their lead content.

The first part of the thesis concerns the synthesis and characterization of anisotropic gold nanoparticles coated with polyvinylpyrrolidone (PVP). The anisotropic form gives particular plasmonic properties to the nanoparticles and allows their integration into the solar cells with minimal morphological disturbances to the layers of the device. PVP coating ensures good stability to nanoparticles, but it is not enough thick to guarantee their electrical insulation. Metallic nanoparticles in contact with the active layer of solar cells can lead to

unwanted charge recombination or exciton quenching if they are not electrically isolated. Therefore, a procedure was implemented to cover the gold anisotropic nanoparticles stabilized by PVP with a thin silica shell, adapting the conditions of the Stöber method and exploiting the ability of PVP to act as a primer.

In the second part of the work, the synthesized nanoparticles were used to fabricate plasmonic organic devices. The nanoparticles coated with PVP were integrated at different concentrations within the hole transport layer (HTL) and the study of optical, electrical and morphological effects on the devices was conducted. Since the effects of the nanoparticles on the devices vary according to the position in which they are located, a further investigation was carried out by integrating the nanoparticles, coated with PVP and silica, at the interface between the HTL and the active layer.

The analysis of the effects of plasmonic nanoparticles in thin-film solar cells was extended, in the third part of the thesis, to devices based on organic-inorganic hybrid perovskites, whose mechanisms of photogeneration and charge transport are different with respect to organic semiconductors. The study was carried out by integrating the nanoparticles in devices characterized by different thickness of the active layer, in order to understand the contribution of the nanoparticles in compensating the efficiency losses in devices with very thin active layers.

Sintesi

La capacità di soddisfare il fabbisogno energetico globale attraverso fonti rinnovabili eliminando la dipendenza dalle risorse fossili è una delle priorità principali per lo sviluppo sostenibile dell'umanità. La tecnologia fotovoltaica basata sul silicio consente di ottenere efficienze di conversione fino al 26%, ma gli elevati costi di fabbricazione dei pannelli solari ne limitano notevolmente l'applicazione. La ricerca di soluzioni alternative ha portato allo sviluppo di celle solari basate su semiconduttori organici e su perovskiti ibride organico-inorganiche. L'utilizzo di materiali poco costosi, la produzione attraverso processi basati sull'uso di soluzioni e realizzati a bassa temperatura, pertanto compatibili con tecniche di produzione su larga scala e anche su substrati flessibili, rendono queste celle particolarmente interessanti per i ridotti costi di fabbricazione e per le potenziali applicazioni in dispositivi portatili o come fotovoltaico architettonicamente integrato. Il limite principale alla commercializzazione delle celle solari organiche è la bassa efficienza (circa il 10% per le celle più efficienti) determinata dalla ridotta quantità di luce assorbita dallo strato attivo, il cui spessore è limitato a causa della bassa mobilità di carica e della ristretta lunghezza di diffusione degli eccitoni nei semiconduttori organici.

D'altra parte, i dispositivi a base di perovskite raggiungono un'efficienza superiore al 22%, ma contengono piombo che è un elemento tossico.

Gli studi riportati nel presente lavoro riguardano l'integrazione di nanoparticelle plasmoniche in celle solari organiche e a base di perovskite e l'investigazione dei loro effetti sulle proprietà e sulle prestazioni dei dispositivi. L'introduzione di nanoparticelle plasmoniche nelle celle solari permette di incrementare la quantità di luce assorbita dallo strato attivo senza aumentarne lo spessore, sfruttando gli effetti plasmonici di light-scattering e near-field enhancement. Questa strategia è particolarmente utile nelle celle solari organiche in cui l'efficienza non può essere migliorata aumentando lo spessore dello strato attivo; inoltre, può essere impiegata per compensare le perdite di assorbimento di luce in celle a perovskite prodotte con uno strato attivo sottile per ridurre il contenuto in piombo.

La prima parte della tesi ha riguardato la sintesi e la caratterizzazione di nanoparticelle anisotropiche d'oro ricoperte da polivinilpirrolidone (PVP). La forma anisotropa conferisce particolari proprietà plasmoniche alle nanoparticelle e ne consente l'integrazione nelle celle

solari con minimi disturbi morfologici agli strati del dispositivo. Il ricoprimento di PVP assicura una buona stabilità alle nanoparticelle, ma non è sufficientemente spesso da garantirne l'isolamento elettrico. Le nanoparticelle metalliche a contatto con lo strato attivo di celle solari possono portare a fenomeni indesiderati di ricombinazione di cariche o quenching di eccitoni se non sono isolate elettricamente. Pertanto, è stata implementata una procedura per ricoprire le nanoparticelle anisotrope d'oro stabilizzate da PVP con un sottile strato isolante di silice, adattando le condizioni del metodo di Stöber e sfruttando la capacità del PVP di agire da primer.

Nella seconda parte del lavoro le nanoparticelle sintetizzate sono state impiegate per la realizzazione di dispositivi plasmonici organici. Le nanoparticelle ricoperte di PVP sono state integrate a differenti concentrazioni all'interno dello strato trasportatore di lacune (HTL) e lo studio degli effetti ottici, elettrici e morfologici sui dispositivi è stato condotto. Dato che gli effetti delle nanoparticelle sui dispositivi variano in funzione della posizione in cui sono inserite, è stata realizzata una successiva investigazione integrando le nanoparticelle, ricoperte da PVP e da silice, all'interfaccia tra l'HTL e lo strato attivo.

L'analisi degli effetti delle nanoparticelle plasmoniche in celle solari a film sottile è stata estesa, nella terza parte della tesi, a dispositivi basati su perovskiti ibride organico-inorganiche, i cui meccanismi di fotogenerazione e trasporto di carica sono diversi rispetto ai semiconduttori organici. Lo studio è stato condotto integrando le nanoparticelle in dispositivi caratterizzati da diverso spessore dello strato attivo, al fine di comprendere il contributo delle nanoparticelle nel compensare le perdite di efficienza nei dispositivi con strati attivi molto sottili.

List of abbreviations

AFM	Atomic Force Microscopy
AM	Air Mass
BCP	Bathocuproine
BHJ	Bulk HeteroJunction
CB	Chlorobenzene
DMF	Dimethylformamide
DMSO	Dimethyl sulfoxide
DSSCs	Dye-Sensitized Solar Cells
EQE	External Quantum Efficiency
ETL	Electron Transport Layer
FF	Fill Factor
FRET	Forster Resonance Energy Transfer
FTO	Fluorine doped Tin Oxide
GBL	γ -butyrolactone
HET	Hot Electron Transfer
HOMO	Highest Occupied Molecular Orbital
HTL	Hole Transport Layer
HTM	Hole Transport Material
ILs	Interlayers
ITO	Indium Tin Oxide
J_{sc}	Short-Circuit current density
LSPR	Localized Surface Plasmon Resonance
LUMO	Lowest Unoccupied Molecular Orbital
OSCs	Organic Solar Cells
P3HT	poly(3-hexylthiophene-2,5-diyl)
PC₆₁BM	[6,6]-Phenyl C61 butyric acid methyl ester
PCE	Power Conversion Efficiency
PEDOT:PSS	Poly(3,4-ethylenedioxythiophene)-poly(styrenesulfonate)
Poly-TPD	Poly[N,N'-bis(4-butylphenyl)- N,N'-bis(phenyl)-benzidine]
PRET	Plasmon Resonant Energy Transfer
PSCs	Perovskite Solar Cells
PVP	Polyvinylpyrrolidone
QDSCs	Quantum Dot Solar Cells
SEM	Scanning Electron Microscope
SERS	Surface-Enhanced Raman Spectroscopy
SPPs	Surface Plasmon Polaritons
TCO	Transparent Conducting Oxide

TE	Transparent Electrode
TEM	Transmission Electron Microscope
TEOS	Tetraethyl orthosilicate
V_{oc}	Open Circuit Voltage

Introduction

The study of nano-sized materials represents one of the most hot topic in the field of material science because the engineering of the matter at the nanoscale makes possible the exploitation of phenomena that induce very particular properties, otherwise negligible at the macroscale. Nano-shaped materials can therefore be used to boost the performance of the devices in many fields, such as sensing, catalysis, nanomedicine and energy. This last topic is very interesting since in the last decades, world energy demand is increased rapidly due to the growth of the population and the development of new emerging economies. According to the projections shown in the International Energy Outlook 2016 report^[1], the world energy consumption will rise by 48% between 2012 and 2040. Nowadays, over the 85% of the energy is produced by the combustion of fossil fuels (oil, coal and natural gas) that are not sustainable energy sources because of their limited availability and the damaging impact on the environment. The use of these sources determines a huge release of carbon dioxide (CO₂) in atmosphere, contributing to the increase of the greenhouse effect and therefore of the global warming responsible of climatic change. The replacement of fossil fuels with renewable energy sources like the wind and the sun is the most promising strategy for a sustainable production of energy. The scientific community is making great efforts to develop new cost effective green technologies and, in this context, the research in photovoltaic field is particularly intense.

At present the photovoltaic market is dominated by the silicon solar cells, but their fabrication costs are still relatively high, because of crystalline silicon production requires high temperature processes with great energy consumptions and a significant environmental impact. The objective of researchers is to overcome silicon based technology with new thin film solar cells that permit to lower the production cost while preserving high efficiency of conversion.

Solar cells based on organic semiconductors are one of the most promising alternatives to the silicon devices. Low cost, lightweight, flexibility of such materials and the compatibility of fabrication processes with roll-to-roll technology are interesting features of the organic solar cells. However, they have not yet reached power conversion efficiency high enough to be competitive with silicon cells. Short exciton diffusion lengths and low charge mobility typical

of organic semiconductors impose a limited active layer thickness in OSCs, generally below 100 nm, reducing light absorption.

Another interesting photovoltaic technology developed in the last years involves the use of organohalide lead perovskites as photoactive materials that permit to manufacture solar cells with a certified efficiency up to 22.1%. However, the reduced stability of the materials together with their content of toxic lead limit the commercialization of perovskite based devices.

A promising approach to boost these emerging photovoltaic technologies is based on the use of plasmonic nanoparticles for their ability to concentrate and manipulate the light at the nanoscale^[2].

In response to an incident electromagnetic field, the highly polarizable electron clouds in metallic nanoparticles are displaced from their equilibrium position and, subjected to the restoring force due to the electrostatic attraction of the nuclei, begin to oscillate. When the frequency of the incident light is equal to that of the electron oscillations, the phenomenon known as localized plasmonic surface resonance (LSPR) occurs. As a consequence of this resonant interaction, several processes take place that can be exploited for different application including sensing^[3,4], catalysis^[5], photothermal cancer therapy^[6], bioimaging^[7], surface-enhanced Raman spectroscopy (SERS)^[8], solar energy technology^[9]. The intensity and frequency of the LSPR depend on the composition, size, shape and dielectric environment of the metallic nanostructures^[10]. Therefore, the possibility to modulate their properties with the aim to obtain the optimal response for the specific application of interest has stimulated the development of several nanofabrication techniques for their production.

The incorporation of plasmonic nanoparticles in solar cells constitutes an effective strategy to enhance the absorption of sunlight without increasing the thickness of the active layer. The two main effects involved are the light-scattering and the near field enhancement, deriving from the radiative damping of the plasmonic resonance that occurs spontaneously within few femtosecond after the excitation. The first increases the light path inside the cell, while the latter boosts the absorption cross section of materials. For these reasons, the integration of plasmonic nanoparticles in organic solar cells leads to an enhancement of their efficiency as a consequence of the increased light harvesting ability of the active layer. On the other hand, it is possible to exploit plasmonic nanoparticles to compensate the light

absorption losses in perovskite cells having a very thin active layer and therefore a low lead content.

In this thesis work, anisotropic gold nanoparticles appropriately synthesized have been integrated in organic and perovskite solar cells and their effects on the optical and electrical properties of the devices have been investigated. This work is motivated by the many interesting properties possessed by gold nanoplates, particularly suitable for improving the performance of solar cells, and by the fact that their use has never been reported before.

Thesis outline

Chapter 1 provides an overview of the phenomena involved in the interaction between light and metals from bulk to nanoscale. The localized surface plasmon resonance of the metallic nanoparticles is discussed and the influence of different parameters (metal composition, size, shape, dielectric environment and particle-particle coupling) is described.

After a brief discussion of the main aspects to consider in the choice of the most appropriate type of nanoparticles for the successive incorporation in solar cells, a description of the more interesting synthetic procedures reported in literature is made. Finally, considering that, due to their metallic nature, the nanoparticles could lead to harmful electrical effects when they are incorporated into solar devices, effective strategies for coating the nanoparticles with an insulating layer are discussed.

In Chapter 2 a brief discussion of the evolution of the photovoltaic technology and of the characterization of solar devices is provided. After an overview of the main properties of organic and inorganic semiconductors, the principal organic device architectures and their working principles are detailed discussed to explain the factors that limit their efficiency. The different strategies to exploit the beneficial plasmonic effects of metallic nanoparticles integrated in bulk heterojunction organic solar cells to enhance their efficiency are presented and several pertaining works in literature are considered. A description of perovskite materials, of the main optoelectronic properties and the most common deposition methods used to fabricate solar cells is given. The integration of plasmonic nanoparticles to reduce the thickness of the active layer and in turns the toxic lead content without reduce the efficiency of the devices is discussed, with a particular attention towards plasmonic inverted perovskite solar cells.

In Chapter 3 the synthesis and characterization of anisotropic polyvinylpyrrolidone stabilized gold (Au@PVP) nanoparticles are reported. The versatility of the method used, adapted from one described in the literature, allows to obtain nanoparticles with different size and in turns plasmonic properties. A synthetic protocol to coat the anisotropic gold nanoparticle with a thin insulating silica shell (Au@SiO₂) is developed. A detailed description of the different steps accomplished to optimize the conditions of reaction and the subsequent purification process is given.

In Chapter 4 the optimization of the procedure for the fabrication of an organic solar cell to use as a reference for the investigation of the effects resulting from the subsequent integration of plasmonic nanoparticles is reported. Au@PVP nanoparticles were embedding in the hole transport layer of the cell. After a preliminary optimization of the incorporation procedure, a study of the effects of the nanoparticle concentration on the cells was accomplished through electrical, optical and morphological characterizations. Further experiments in which the Au@PVP and Au@SiO₂ nanoparticles were integrated at the interface between the hole transport layer and the active layer of the organic solar cell were reported.

Chapter 5 presents the integration of plasmonic Au@PVP nanoparticles in the hole transport layer of a reference inverted perovskite solar cell. Electrical and optical characterization demonstrated that, in contrast with the results obtained for organic cells, no performance improvement was observed, probably for the high light harvesting ability of the perovskite. A further study in which the nanoparticles were integrated in a different reference perovskite device with a reduced active layer thickness is reported. Due to the instability of the nanoparticles in the solution of the different hole transport material (HTL), Au@PVP nanoparticles were deposited at the interface between the HTL and the active layer. The electrical characterization demonstrated a notable improvement of the cell performances as a consequence of the nanoparticles integration. The results of the preliminary characterization to investigate the origin of the ameliorating effects produced by the nanoparticles in the devices are reported.

Finally, a summary of the main results obtained in this thesis and proposals for future works are shown in chapter 6.

References

- [1] J. Conti et al., International energy outlook 2016 with projections to 2040. *USDOE Energy Information Administration (EIA), Washington, DC (United States). Office of Energy Analysis*, **2016**.
- [2] M. A. García, Surface plasmons in metallic nanoparticles: fundamentals and applications. *Journal of Physics D: Applied Physics*, **2011**, 44, 283001.
- [3] K. Saha et al., Gold nanoparticles in chemical and biological sensing. *Chemical reviews*, **2012**, 112, 2739-2779.
- [4] A. Taylor et al., Single-molecule plasmon sensing: current status and future prospects. *ACS sensors*, **2017**, 2, 1103-1122.
- [5] W. Hou et al., A review of surface plasmon resonance-enhanced photocatalysis. *Advanced Functional Materials*, **2013**, 23, 1612-1619.
- [6] X. Huang et al., Plasmonic photo-thermal therapy (PPTT). *Alexandria journal of medicine*, **2011**, 47, 1-9.
- [7] E. Hutter et al., Gold nanoparticles and quantum dots for bioimaging. *Microscopy research and technique*, **2011**, 74, 592-604.
- [8] S. Schlücker, Surface-Enhanced Raman spectroscopy: Concepts and chemical applications. *Angewandte Chemie International Edition*, **2014**, 53, 4756-4795.
- [9] E. Stratakis et al., Nanoparticle-based plasmonic organic photovoltaic devices. *Materials Today*, **2013**, 16, 133-146.
- [10] K. L. Kelly et al., The optical properties of metal nanoparticles: the influence of size, shape, and dielectric environment. *The Journal of Physical Chemistry B*, **2003**, 107, 668-677.

Chapter 1

Metallic nanostructures: plasmonic properties and synthesis

1. 1 Introduction

The incorporation of plasmonic metal nanoparticles in thin-film solar cells is an effective strategy to enhance their properties by exploiting the ability of the nanoparticles to manipulate light at the nanoscale. This ability derives from the presence in metal nanoparticles of highly polarizable electron clouds that in particular conditions may strongly interact with the light. The nanometric size is another fundamental requirement that allows the resonant interaction and this explain why it does not occur in bulk metal. By changing the composition and the geometrical properties of the nanoparticles it is possible to modulate their plasmonic properties, in order to take full advantage of their beneficial effects in the solar cells in which they are incorporated.

In the following, a more detailed description of the phenomena involved in the interaction between light and metals from bulk to nanoscale will be given. Furthermore, the influence of several parameters on the plasmonic properties of metallic nanoparticles will be discussed.

Advances in nanofabrication have led to the development of a variety of techniques, including chemical synthesis, electron-beam lithography, wet-chemical etching, focused ion beam, laser ablation, for producing customized nanoparticles with suitable properties for many different applications. In this field, chemical synthesis is one of the most used approaches because of their versatility, low cost and the possibility to be accomplished without the need of too specific equipment. After a brief discussion of the main aspects to consider in the choice of the most appropriate type of nanoparticles for the subsequent incorporation in solar cells, a description of the more interesting synthetic procedures reported in literature will be made. Furthermore, considering that, due to their metallic nature, the nanoparticles could lead to harmful electrical effects when they are incorporated into solar devices, effective strategies for coating the nanoparticles with an insulating layer will be discussed.

1.2 Volume, surface and localized surface plasmons

Free electrons in bulk metals behave like a gas of free charge carriers within a lattice made of positively charged ions. In particular conditions (incident electron beam^[1]) it is possible to induce the collective oscillation of the electron cloud that occurs at a characteristic frequency, called plasma frequency (ω_p):

$$\omega_p = \sqrt{\frac{Ne^2}{m_{\text{eff}}\epsilon_0}} \quad (1.1)$$

where N is the density of electrons, m_{eff} is the effective mass of the free electrons, e is the elementary charge and ϵ_0 is the permittivity of free space^[2,3]. The collective oscillations of free electrons in a bulk metal are called volume plasmons. The oscillations correspond to longitudinal waves that propagate with well defined frequency and wavevector. The excitation of plasmons by an electromagnetic radiation is not possible in bulk metal because a photon of the same frequency in a free space has a wavevector smaller than that of the corresponding plasmon and consequently is not possible the momentum conservation, a required condition to have the resonance.

The plasma frequency of metals is determined experimentally through electron loss spectroscopy and its value is comprised in the range 5-15 eV for most materials^[4]. This means that the bulk plasma frequency for most metals is higher than the frequency of visible light^[5]. When an electromagnetic radiation is incident at a frequency higher than the plasma frequency, the electrons can not respond quickly enough to the driving force of the incident field and the light will be transmitted through the metal or absorbed in the interband transitions^[1,2]. Instead, in the case of light with a frequency smaller than the plasma frequency, the electrons will oscillate 180° out of phase with the incident light, causing a strong reflection.

If a thin metallic film is considered instead of the bulk metal, it is possible to excite, in particular conditions, the collective oscillations of free electrons at the interface between the metallic layer and a dielectric layer. These oscillations, known as surface plasmon polaritons (SPPs), are highly localized at the interface and can propagate along it for a relatively long distance (also few micrometers)^[6]. The intensity of these evanescent waves decay exponentially with the distance from the interface and the decay rate is much higher

in metal than in dielectric. The difficulty in exciting SPPs directly with incident light is due to a momentum mismatch that exists between the light and SPPs of the same frequency.

To overcome these limitations different strategies can be adopted such as the use of Otto geometry^[7], grating on the metal surface^[8], topological defects on the surface, like sub-wavelength apertures, slits and holes^[9,10]. The surface plasmon polaritons have a frequency (ω_{SPP}), related to the bulk plasmon frequency ω_p and to the the permittivity of the dielectric material (ϵ_d) coupled to the metal, given by the following equation:

$$\omega_{SPP} = \frac{\omega_p}{\sqrt{(1 + \epsilon_d)}} \quad (1.2)$$

More interesting is the case of the interaction between an incident electromagnetic wave and a metallic nanoparticle with sizes much smaller than the wavelength of the wave. The free electrons in the nanoparticles are displaced from their equilibrium position by the interaction with the wave electric field (figure 1.1); at the same time the electron cloud is subject to a restoring force due to the attraction of the nuclei, whereby the electrons begin to oscillate with a characteristic oscillation frequency.

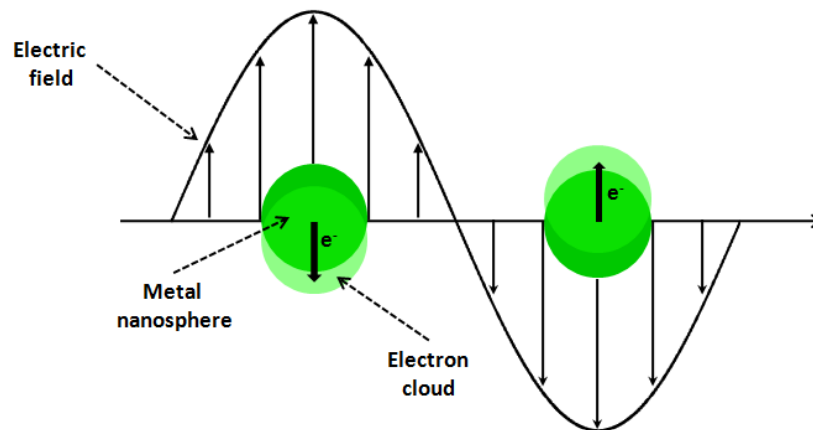


Figure 1.1 Schematic representation of the interaction between the electromagnetic radiation and a spherical nanoparticle.

When the frequency of the incident electromagnetic field is equal to that of the oscillations, the phenomenon known as localized surface plasmon resonance (LSPR) occurs. The frequency of LSPR (ω_{LSPR}) is given by the following equation^[3]:

$$\omega_{LSPR} = \frac{\omega_p}{\sqrt{(1 + 2\epsilon_d)}} \quad (1.3)$$

Localized surface plasmons are transverse standing waves^[5], therefore no momentum matching conditions are required for their excitation, which can be obtained directly by an incident electromagnetic field.

The LSPR frequency depends on the polarizability (α) of the nanoparticle. Considering for simplicity a spherical one:

$$\alpha = 4\pi\epsilon_0 r^3 \left(\frac{\epsilon_m + \epsilon_d}{\epsilon_m + 2\epsilon_d} \right) \quad (1.4)$$

where r is the sphere radius and ϵ_m and ϵ_d are the permittivities of the metal and dielectric material that surrounds the nanoparticle, respectively. The LSPR occurs for the condition that maximize the polarizability, i.e. when $\epsilon_m = -2\epsilon_d$.

Mie theory allows to determine the optical properties for spherical nanoparticles assuming that they are not interacting. This means that the distance between the nanoparticles is large enough so that each nanoparticle is not affected by the field created by the neighbor ones^[11]. For nanoparticles with sizes much smaller than the wavelength of the incident light (quasistatic regime) the scattering cross-section (σ_{scat}) and the absorption cross-section (σ_{abs}) of the nanoparticles are defined by the following equations:

$$\sigma_{\text{scat}} = \frac{k^4}{6\pi} \left| \frac{\alpha}{\epsilon_0} \right|^2 = \frac{8\pi}{3} k^4 r^6 \left| \frac{\epsilon_m - \epsilon_d}{\epsilon_m + 2\epsilon_d} \right| \quad (1.5)$$

$$\sigma_{\text{abs}} = k \text{Im} \left(\frac{\alpha}{\epsilon_0} \right) = 4\pi k r^3 \text{Im} \left| \frac{\epsilon_m - \epsilon_d}{\epsilon_m + 2\epsilon_d} \right| \quad (1.6)$$

where $k = 2\pi/\lambda$ and Im denotes the imaginary part. Equations 1.5 and 1.6 show that for very small nanoparticles, the scattering cross-section decrease more rapidly than the absorption. Therefore, it can be concluded that for small nanoparticles (size smaller than 50 nm for Au) the predominant phenomenon is the absorption, while scattering effect is preferred in big nanoparticles.

In resonance conditions, the confined electron oscillations in plasmonic nanostructure produce an intense local electromagnetic field that can be several orders of magnitude greater than the incident one^[3]. This local field, known as near-field, decays exponentially

with the distance from the nanostructure (figure 1.2), typically within 10-30 nm from the surface^[12,13].

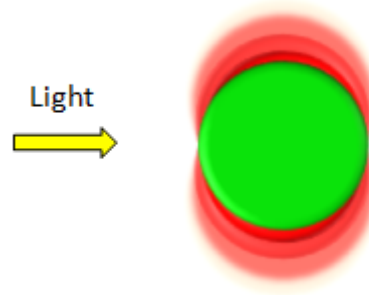


Figure 1.2 Schematic illustration of the electromagnetic near-field (red) in proximity of a spherical nanoparticle (green) at plasmon resonance.

Both the plasmonic effects of light scattering and near-field enhancement can be exploited to increase the efficiency of solar cells. A description of the mechanisms involved will be given in Chapter 2.

The equations from 1.3 to 1.6 clearly state that the LSPR parameters depend on the composition, size, shape and dielectric environment of the metallic nanostructures. Therefore, by changing these parameters it is possible to tune the plasmonic properties of the nanoparticles.

Nanoparticle composition

The dependence of the LSPR frequency from the composition of the nanostructure is obvious considering that it is determined by the density of the conduction electrons. Combining equations 1.1 and 1.3 this dependence can be explicated:

$$\omega_{\text{LSP}} = \sqrt{\frac{Ne^2}{m_{\text{eff}}\epsilon_0(1 + 2\epsilon_d)}} \quad (1.7)$$

Applying equation 1.7 to calculate the resonance frequency of gold and silver nanospheres with the same geometrical properties, the obtained values are close because of their similar electronic density, i.e. $N = 5.90 \times 10^{22} \text{ cm}^{-3}$ (gold) and $5.86 \times 10^{22} \text{ cm}^{-3}$ (silver). However, this result is in contrast with the experimental measurements from which it can be observed that the surface plasmon absorption band for silver is located at higher frequency than gold (figure 1.3).

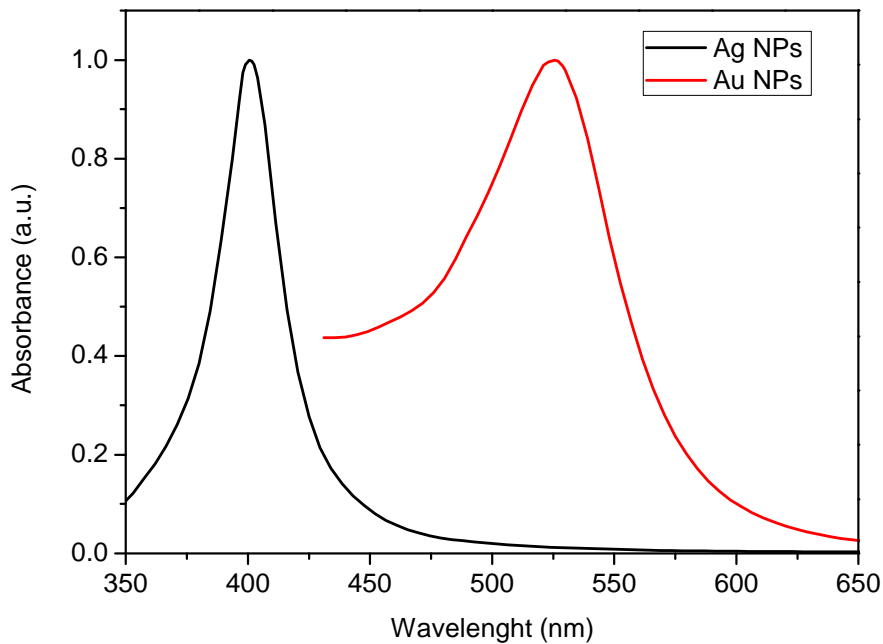


Figure 1.3 Normalized absorption spectra of Ag and Au nanospheres with diameters of 20 nm.

This can be explained considering that equation 1.7 is strictly valid for free electrons behavior. In real metals deviations from this behavior must be considered. In particular, for noble metals the inter-band transition between d-band and conduction band and the intra-band transition within conduction band as well as the relativistic effect related to the core electrons have a great influence on the electronic properties of the metals^[14].

Therefore the dielectric function is integrated with an additional terms ϵ_q that take into account these effects^[15]. The bulk plasmon frequency of noble metals is given by equation:

$$\omega_{LSP} = \sqrt{\frac{Ne^2}{m_{eff}\epsilon_0(\epsilon_q + 2\epsilon_d)}} \quad (1.8)$$

Nanoparticle size

The size of the nanoparticles is another factor that affects significantly their plasmonic properties.

As already described, for small size nanoparticles absorption is significant, while is low for big nanoparticles for which the scattering is predominant.

In nanoparticles with sizes smaller than the wavelength of the incident light, the phase of the electromagnetic field is constant over the extension of the nanoparticle, the polarization

of the electron cloud is coherent in all metal and consequently only dipolar plasmon oscillations are excited^[4,16].

When the size of the nanoparticles is comparable to the resonant electromagnetic wavelength, due to the finite velocity of light, the electric field distribution along each nanoparticle is not uniform. The effect is that higher multipolar modes beyond the dipolar one are excited^[17]. As a consequence of the non-uniformity of the field distribution, the interference of the coulomb fields in different points of the nanoparticle is not always constructive. Therefore the restoring force of the electron cloud is weakened and this produces the red-shift of the dipolar resonance with the increase in the size of the nanoparticle (figure 1.4).

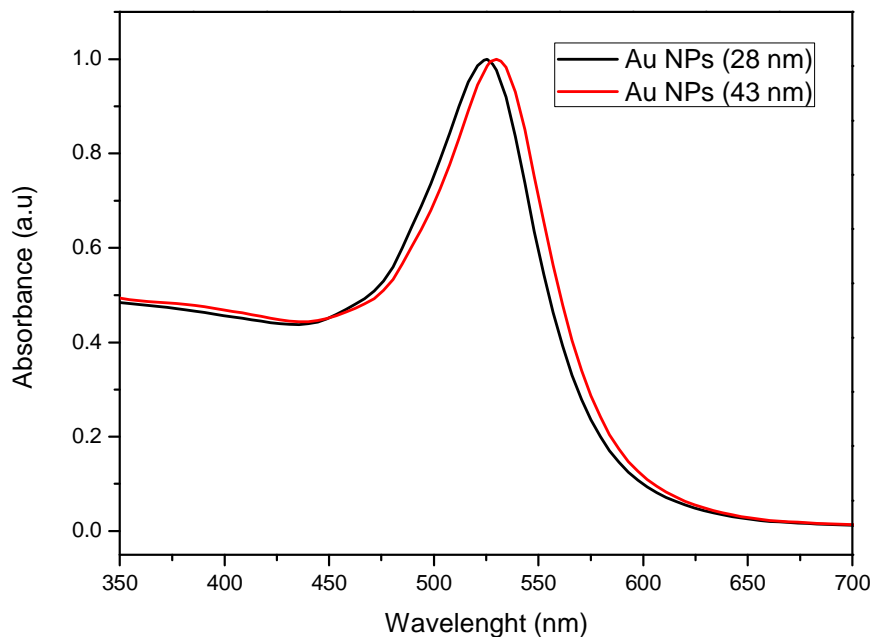


Figure 1.4 Normalized absorption spectra of gold nanoparticles with different sizes.

Nanoparticle shape

The shape of the nanoparticles has a strong influence on the plasmonic resonance properties. Reducing the symmetry of a nanoparticle by changing its geometry is an effective method to modify the frequency, intensity and resonance modes of LSPR^[18].

Whereas in the case of spherical nanoparticles only one plasmonic band centered at a certain frequency is observed, when the symmetry is reduced to a cylinder, such in the case of the nanorods, two plasmonic resonance bands appear. The first one, related to the

collective electron oscillation along the minor axis (transverse mode), is slightly blue-shifted compared to the resonance band in an equivalent sphere, while the latter, corresponding to the excitation along the major axis (longitudinal mode), is more intense and shifted towards lower frequency. It follows that by increasing the ratio between the main and minor axis, that is the aspect ratio (R), it is possible to displace the second band towards greater wavelength^[19,20,21]. Instead, the short-axis resonance is only weakly affected by the aspect ratio of the nanoparticle. Figure 1.5^[22] shows this behavior for two gold nanorods with different aspect ratio.

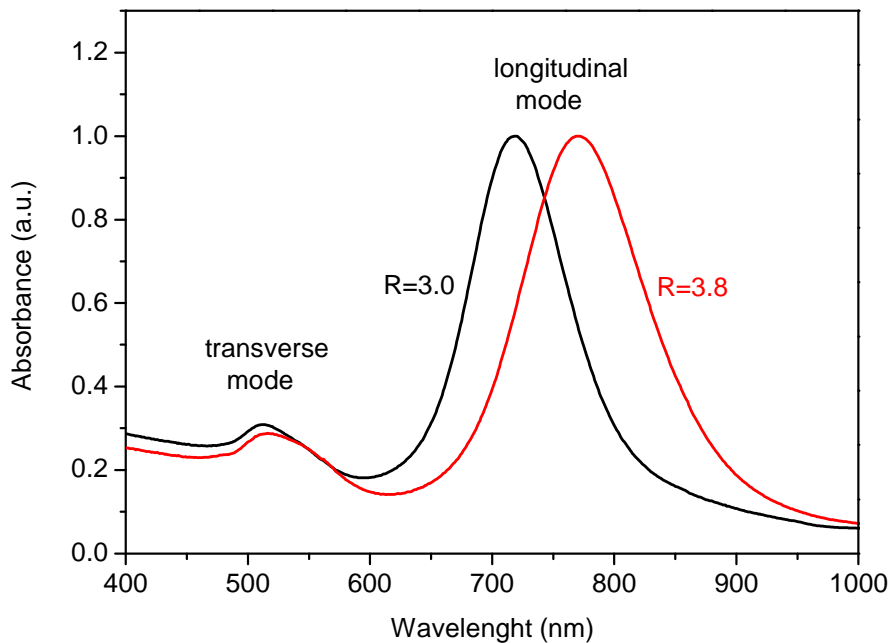


Figure 1.5 Normalized absorption spectra of gold nanorods with different aspect ratio.

Dielectric environment

The dielectric properties of the medium surrounding the nanoparticles significantly affect the frequency of LSPR. In particular, an increase of the dielectric constant of the environment leads to a decrease of the plasmonic frequency, as effect of the polarization of the medium that partially screen the Coulombic restoring force, reducing its intensity^[23]. Since the dielectric constant of a material is linked to the refractive index (n) by the following equation:

$$n = \epsilon_r^{1/2} \quad (1.9)$$

results that an increase of the refractive index produces a red-shift of the plasmon resonance wavelength. More generally, any variation of the refractive index in the local medium around the nanoparticle, such as solvent or presence of adsorbate/surface-capping molecules, leads to a variation of the resonance frequency^[24,25].

In figure 1.6^[26] are reported the calculated extinction spectra for a 60 nm gold nanoparticle with different surrounding media. It can be observed that the increase of the refractive index of the medium produces the shift of the extinction peak toward longer wavelength. In particular, the extinction peak is centered at 508 nm for air, 536 nm for water and 560 nm for silica. As an effect of the higher refractive index of the medium, the extinction cross-section of the nanoparticle also increases.

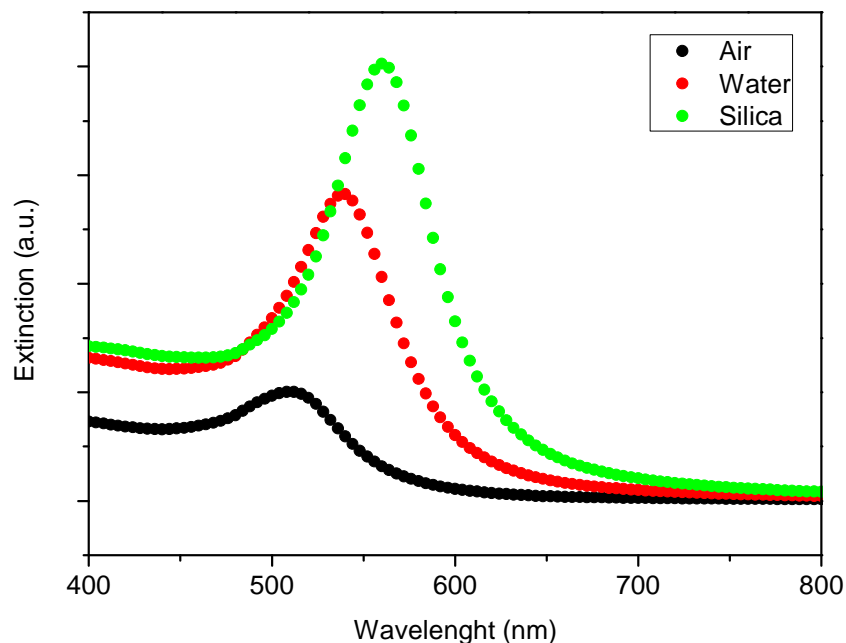


Figure 1.6 Calculated extinction spectra for a 60 nm gold nanosphere in air ($n=1.0$), water ($n=1.33$), silica ($n=1.5$).

Particle-particle coupling

The interaction between plasmonic nanoparticles is another phenomenon that affects the plasmon resonance. Depending on the relative distance between nanoparticles two types of coupling can occur: near-field and far-field couplings. When the inter-particle distance is smaller or comparable to the particles size, the near-field coupling takes place. The electric field felt by each nanoparticle is the contribution of the incident field and the near-field of the neighbors nanoparticles. The coupling results in a red-shift of the frequency of plasmonic

resonance of about hundreds of meV at small particle spacing^[23,27]. Moreover, within the gap between two adjacent nanoparticles the electric field is dramatically enhanced^[28].

If the distance between the nanoparticles is greater than their size, near-field coupling is weak and radiative interaction is predominant. In this condition, the scattered electromagnetic field of a particle can enhance or reduce the coulomb restoring force of another nanoparticle depending on the distance and relative phase of the field^[29].

As a consequence, a blue-shift or red-shift of the plasmonic resonance band can be observed, whose magnitude is at most of the order of tens of meV^[23].

1.3 Nanofabrication of plasmonic gold nanoparticles

Metallic nanoparticles can be produced by top-down or bottom-up approaches. The first include all the methods that starting from metal bulk allow to reduce the size of the sample to the nanometric scale, while the latter exploit chemical or physical force operating at the nanoscale to assemble basic units into larger structures^[30,31]. The main top-down processes exploit lithographic (for instance, electron-beam lithography) and etching techniques (wet-chemical etches, focused ion beam, laser ablation)^[32]. Although they are essential for specific applications, they require expensive equipment, long times and often vacuum or high temperature conditions. Moreover, they have an inherent limit in the minimum size accessible. For all these reasons they can not be used for the large-scale production of nanostructures. Bottom-up methods, instead, do not have the disadvantages of the top-down techniques and therefore they are the most used. Among bottom-up methods, chemical synthesis based on the reduction of metal salts by a variety of reducing agent^[33] is commonly used for its versatility in the production of metallic nanostructures. It allows to obtain nanoparticles of different shape and size dispersed in aqueous or organic solvents. Furthermore, by exploiting chemical reactions it is possible to appropriately functionalize the surface of the nanoparticle or to growth around it different concentric layer obtaining multi-shell nanostructures. An aspect that makes this approach attractive is that it does not require particular equipment or high costs, because it can be achieved by using common chemicals and laboratory equipments. The versatility of chemical synthesis is particularly useful for producing plasmonic nanoparticles with well defined optical, geometrical and stability requirements, as in the case of nanoparticles that must be integrate in thin-film solar cells in order to improve their properties.

To enhance the light harvesting of the solar cells, it is necessary that the plasmonic resonance band of the nanoparticles is well adapted to the absorption spectrum of the active layer of the solar cells. As previously explained, plasmon resonance is affected among other parameters by the material, shape and size of the nanoparticles. Silver and gold are the two most used materials for the production of plasmonic nanoparticles for the incorporation in solar cells, since they have a very intense plasmon resonance band that can be tuned from visible to near infrared frequencies. Gold has the advantage to be chemically stable; therefore nanoparticles produced with this metal are not susceptible to chemical reactions when incorporate into the solar device. The shape and size must be appropriately chosen so that the nanoparticles incorporated in the device do not disturb its structure, considering that the thickness of the layers in thin-film solar cells is of the order of tens of nanometers. Moreover, the shape and size of the nanoparticles must be carefully evaluated to obtain the desired plasmonic properties. 2D nanostructures, such as nanoplates, are particular interesting because they tend to take a flat orientation with respect to the cell substrate, so they do not produce morphological problems within the cell. Furthermore, by changing their size it is possible to tune their plasmonic resonance from visible to infrared spectral range. On the other hand, near the corners of these nanostructures, the plasmonic field is very high due to the lightning rod effect.

Another fundamental aspect to consider when choosing the nanoparticles to be used for the fabrication of plasmonic solar cells is the stability of the nanoparticles in different dispersion media. The existence of nanoparticles in the colloidal state is ensured by the presence on their surface of charged ligands (electrostatic stabilization) or of physically/chemically bound polymers (steric stabilization). To incorporate nanoparticles within a particular layer of thin-film solar cells, the nanoparticles are added to the solution of the material that constitutes the layer, before its deposition. The solvent used for the preparation of this solution can be polar or apolar depending on the properties of the material and in the case of aqueous solution, the pH of the system can be far away from neutrality. All these parameters affect the stability of the nanoparticles, which preserve their colloidal state until the repulsive forces between them exceed attractive Van der Waals forces.

Charge-stabilized nanoparticles are sensitive to the presence of electrolytes in the dispersion medium that can screen the charges causing the aggregation of the nanoparticles. In addition, they require a polar solvent. Polymer-stabilized nanoparticles have, instead, a

greater tolerance toward the increase of the ionic strength of the medium or pH variations. Moreover, steric stabilization through amphiphilic polymers is effective in both non-aqueous media and aqueous media. Therefore, for the fabrication of plasmonic solar cells, sterically stabilized nanoparticles are preferred because of their greater stability in different dispersion medium with respect to electrostatically stabilized nanoparticles. On the basis of the previous considerations, in this thesis work it was decided to adopt sterically stabilized gold nanoplates as plasmonic nanoparticles for the subsequent fabrication of plasmonic solar cells. Therefore, a bibliographic research work was carried out to identify the most interesting synthetic protocols to use for the synthesis of this typology of nanoparticles.

1.3.1 Synthesis of gold nanoplates

Numerous protocols that permit to obtain gold nanoparticles of several shapes such as nanorod, nanocube, nanostars^[34,35,36], with different sizes and high reaction yield are reported in literature. The development of these synthetic procedures has been stimulated by the interest in many fields (sensing, catalysis, medicine, etc.) towards the particular plasmonic properties deriving from the breaking of the spherical symmetry^[37]. Although there are several methods for the synthesis of gold nanoplates, they generally have some limitations^[38]: the morphological yield is usually below 70% and the nanoparticles have a high polydispersity. Furthermore, some procedures do not permit to obtain nanoplates with lateral dimensions below 100 nm^[39,40]. These difficulties are related to the fact that the formation of nanoplates is not thermodynamically favored considering that the bulk crystal structures of gold is face-centered cubic^[41].

Among the different synthetic procedure reported in the literature, here we will focus the attention on the most appropriate for the thesis. The synthetic strategies adopted in these procedures to obtain gold nanoplates can be essentially distinguished in two main categories: seed-growth and seedless syntheses.

In the seed-growth methods, small gold nanoparticles (seeds) are prepared by reduction of a gold precursor salt with a strong reducing agent in presence of a stabilizing agent. The obtained seeds are added to a growth solution containing the gold precursor and a surfactant, which binds selectively to certain crystalline faces of the seeds. At this point, a reducing agent, less reactive respect to that used for seed formation, is added to the solution. In these conditions, the reduction occurs only on the free surface of gold seeds

because they act as catalysts; consequently, the formation of new particles in solutions is hindered. Due to the presence of the surfactant, the growth is anisotropic and leads to the formation of the nanoplates^[38,42].

Also in seedless synthesis the reduction process involves the use of the gold precursor, of the shape-directing agent and of the reducing agent. However, the preliminary formation of seeds is not required and the growth step occurs directly in-situ^[41].

Scarbelli et al.^[38] have proposed a seed-growth approach for the synthesis of triangular gold nanoplates. Gold seeds were synthesized for reduction of tetrachloroauric (III) acid (HAuCl_4) by the strong reducing agent sodium borohydride (NaBH_4) in presence of cetyltrimethylammonium chloride (CTAC) as stabilizing agent. The growth of the nanoparticles was obtained in two different steps in which the seeds were added sequentially in two solution both containing HAuCl_4 , sodium iodide (NaI), CTAC and ascorbic acid but at different concentrations. In the first solution the seeds were grown into larger nanoparticles, while in the second solution the formation of gold nanotriangles was completed. Both NaI and CTAC act as shape-directing agents, while ascorbic acid is the mild reducing agent. CTAC is also the stabilizing agent. In the reaction products a considerable amount of by-products was present together with the triangular nanoplates. Therefore the authors have proposed a purification procedure to obtain monodisperse gold triangular nanoplates consisting in the flocculation of the nanoplates and in the subsequent recovery of the precipitate and re-dispersion in CTAC solution. By changing the amount of seeds added to the growth solutions and the concentration of NaI, they have demonstrated that it is possible to tune the edge lengths of the nanotriangles in the range 50-150 nm. The average thickness of the nanotriangles was of about 30 nm.

Another seed-growth method for the synthesis of nanoplates has been developed by Wang et al.^[42]. The seeds were produced through the reduction of HAuCl_4 by NaBH_4 in presence of citrate as stabilizing agent. In the growth step the seeds were added in a solution containing additional HAuCl_4 and polyvinylpyrrolidone (PVP) to induce the anisotropic shape during the growth. Finally, hydrogen peroxide (H_2O_2) was used as reducing agent. Also in this case the products obtained were not exclusively triangular nanoplates, but there were also hexagonal plates as well as some spheres. The authors have demonstrated that by changing the volume of H_2O_2 it was possible to tune the edge length of the nanoplates from 50 to 500 nm, while maintaining the thickness between 12 and 15 nm.

Chen et al.^[41] have reported a seedless synthesis of triangular gold nanoplates. The procedure consists in the addition of a solution of sodium tetrachloroaurate (NaAuCl_4) to a solution of CTAC and NaI that act as stabilizing agent and shape-directing agents, respectively. Finally, ascorbic acid is added as reducing agent and the pH of the solution is adjusted to slightly basic value for addition of sodium hydroxide (NaOH). The method described allows to obtain monodispersed triangular gold nanoplates with high morphological yield and tunable edge length in the range 45-120 nm (average thickness 15 nm) by changing the concentration of reagents. The authors do not report any purification treatment after synthesis.

The three procedures described have been compared to establish the most appropriate for producing gold nanoplates to be used in this thesis work for the subsequent incorporation in solar cells. One of the essential aspects considered is the stability of the nanoparticles. The method proposed by Wang et al. allows to directly obtain nanoplates that are sterically stabilized by PVP, while the other two protocols lead to nanoplates electrostatically stabilized by CTAC. The PVP coating offers a greater stability in aqueous dispersions in which are presents electrolytes and more tolerance for pH values far from neutrality. As will be described in the following chapters, gold nanoparticles will be incorporated in strongly acid dispersions ($\text{pH}\approx 1$) containing also a polyelectrolyte. Therefore the coating of PVP is more suitable with respect to that of CTAC. In addition, the PVP coating allows to transfer the nanoplates from aqueous solution in which they are synthesized to ethanol. Because the materials employed for the fabrication of the cells are affected by the presence of water, the possibility to have nanoparticles in ethanol permits to more easily add them in solar cells.

It is important to underline that it is possible to replace the CTAC on the nanoparticle surface with PVP or other polymeric stabilizing. However, it was reported^[42] that this process is not so simple to accomplish and often the substitution is not complete. Moreover, the replacement is generally carried out using an excess of reagents, therefore purification steps are necessary at the end of the CTAC displacement process. The purification procedure must be carefully optimized because complete removal of the excess dispersants can lead to the aggregation or precipitation of the nanoparticles^[43].

The presence of non-triangular by-products in the synthesis proposed by Wang et al. could be an advantage for the subsequent incorporation in solar cells, because they cause a widening of the plasmonic band and therefore a wider overlap with the absorption spectrum

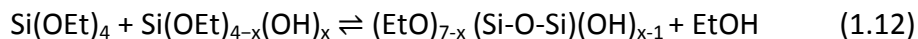
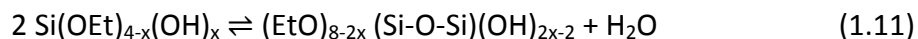
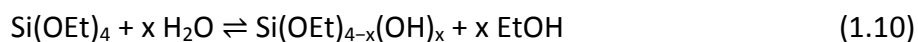
of the active layer of the solar device occurs. As effect of this broadband light harvesting, the absorption of light is greater with respect to the case in which monodisperse nanoparticles, characterized by a more sharp plasmonic band, are integrated in solar devices. It is important to underline that the dimensions of non-planar by-product are at most slightly greater than the thickness of the nanoplates, therefore they do not produce morphological problems when incorporated in the devices. The method considered, with respect to the others, shows the greater versatility to obtain nanotriangles of different sizes. Indeed, by simply changing the amount of hydrogen peroxide it is possible to modify the edge length in the range 50-500 nm, while in the others the range is more restricted.

On the basis of the previous considerations, the method proposed by Wang et al. was adopted in this thesis work as the reference procedure for the synthesis of gold nanoplates.

1.3.2 Synthesis of gold-silica core-shell nanoparticles

As previously explained, in order to take advantage of the incorporation of plasmonic gold nanoparticles in solar cells, a careful evaluation of non-plasmonic effects that the nanoparticles produce in the devices is necessary. Indeed, unfavorable morphological and electrical effects could lead to devices with worse performance compared to the devices without nanoparticles. It was reported that when metal plasmonic nanoparticles are in contact with the active layer or inside it, they can act as charge recombination centers or exciton quenchers if are not electrically insulate. The most used approach to overcome these problems is to cover the metallic core with a shell of insulating material, generally silica. A fine control of the shell thickness is required because the shell must be thick enough to allow the electrical insulation but not much otherwise the near-field deriving from the LSPR is lost inside it. The covering of metallic core with a silica shell is usually accomplished adapting the well-know Stöber method.

This method^[44] developed in 1968 allows to synthesize silica spheres with micrometric size (0.5-2 μm) by adding a silicon alkoxide, usually tetraethyl orthosilicate (TEOS), to a mixture of ammonia, ethanol and water in a well-defined ratio. The silica particles obtained have a narrow size distribution and their dimensions can be controlled by modifying the ratio between the reagents, the pH and the temperature of the solution. Below, the main reactions involved in the process are reported^[45].



TEOS molecules undergo hydrolysis in ethanol/ammonia solution producing silanol monomers, in which the ethoxyl groups (-Si-OEt) are replaced with silanol groups (-Si-OH) (equation 1.10). These groups are more reactive and can condensate between them (equation 1.11) leading to the formation of branched siloxane clusters that trigger the nucleation and growth of silica particles. At the same time, silanol monomers can also condensate with the non-hydrolyzed ethoxyl groups of TEOS (equation 1.12), contributing to the growth of particles.

TEOS hydrolysis occurs through a nucleophilic substitution reaction and since OH^- ions of ammonia are more nucleophilic than H_2O molecules, the rate of the reaction increases with ammonia concentration. In addition, the hydrolysis rate is higher when ethoxyl groups are replaced by silanol groups. This is due to the fact that these substitutions lead to an increase of positive charge on silicon atoms and to a reduction of steric hindrance, whereby the nucleophilic attack to form more silanol groups is favored. It is important to consider that for the ethoxyl groups close to highly condensed siloxane network the nucleophilic attack is obstructed by the steric hindrance, therefore the hydrolysis rate is lower. Condensation between silanol groups or silanol groups and ethoxyl groups also occurs through nucleophilic substitution reactions. In this case the nucleophilic species are the most acidic silanol groups that in basic conditions are present in their deprotonated form. The acidity of a silanol depends on the substituents linked to the silicon. As the reaction proceeds, species with a high degree of polymerization are formed, in which the siloxane substituents reduce the electronic density on the silicon and therefore determine the increase in acidity of the silanols. On the other hand, in the hydrolyzed monomer of TEOS the presence of electron attractor $-\text{OH}$ groups makes the central silicon more electrophilic and susceptible to nucleophilic attack by deprotonated species. Therefore, the condensation of silanol monomers occurs preferentially onto large siloxane network clusters rather than onto other monomers or small oligomers and this leads to the formation of strongly branched structures.

To induce the silica shell growth around the metallic nanoparticles using the Stöber method, it is essential to have a primer on their surfaces, which has a significant chemical or electrostatic affinity for silica. This approach was first demonstrated by Liz-Marzan et al.^[46]. They primed citrate-stabilized gold nanoparticles with aminopropyltrimethoxysilane thanks to the coordination of the gold surface with the nitrogen of the amino silane coupling agent. Then exploiting the reactions of hydrolysis and condensation of the methoxysilane groups present on the other side of the coupling agent, a very thin silica layer was grown using sodium silicate in aqueous basic conditions. Finally the nanoparticles were transferred in ethanol where the silica shell was further grown through Stöber method.

Later, in 2003, Graf et al. proposed a general method^[47] to coat colloids with a silica shell. The method involves the coating of generic nanoparticles with PVP that thanks to its amphiphilic nature shows affinity toward a variety of materials. Due to the presence of PVP on their surface, the nanoparticles are stable in the conditions of the Stöber method. Therefore, by exploiting the ability of PVP to act also as a primer, it is possible to achieve the silica shell growth.

H-bonding interactions are at the basis of the affinity of PVP towards silica^[48]. Due to the polymer nature of PVP numerous H-bonds can be formed between the oxygens of the amide groups and the silanol groups of silica (figure 1.7). The possibility to cover the nanoparticles with a silica shell using this approach has been exploited in this thesis work. Gold nanoplates synthesized following the method proposed by Wang et al. already have a coating of PVP because it is used during their synthesis to obtain the anisotropic shape. Therefore, to grow the silica shell it is possible to directly apply the Stöber method without the need of further steps.

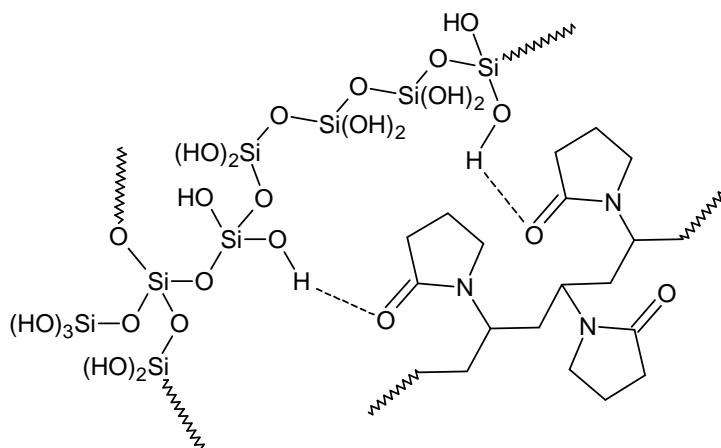


Figure 1.7 H-bonding interactions between PVP and silica.

1.4 References

- [1] B. N. Libenson, Trinal Nature of the Excitation of Bulk Plasmons by a Fast Charged Particle at Grazing Incidence on the Interface between Vacuum and a Metal with Strong Spatial Dispersion. *Journal of Experimental and Theoretical Physics*, **2018**, 127, 37–47.
- [2] N. W. Ashcroft and N. D. Mermin, Solid state physics. Cengage Learning. Inc., New York, **1976**.
- [3] M. Li et al., Plasmon-enhanced optical sensors: a review. *Analyst*, **2015**, 140, 386-406.
- [4] S. A. Maier, Plasmonics: Fundamentals and Applications. *Springer Science*, **2007**.
- [5] P. Manley et al., Design principles for plasmonic nanoparticle devices. In Progress in Nonlinear Nano-Optics. *Springer*, **2015**, 223-247.
- [6] Z. Tang et al., Light trapping in thin film organic solar cells. *Materials Today*, **2014**, 17, 390-396.
- [7] A. Otto, Excitation of nonradiative surface plasma waves in silver by the method of frustrated total reflection. *Zeitschrift für Physik A Hadrons and Nuclei*, **1968**, 216, 398-410.
- [8] R. H. Ritchie et al., Surface-plasmon resonance effect in grating diffraction. *Physical Review Letters*, **1968**, 21, 1530.
- [9] T. H. Isaac et al., Surface plasmon mediated transmission of subwavelength slits at THz frequencies. *Physical Review B*, **2008**, 77, 113411.
- [10] S.-H. Chang et al., Surface plasmon generation and light transmission by isolated nanoholes and arrays of nanoholes in thin metal films. *Optics Express*, **2005**, 13, 3150-3165.
- [11] M. A. Garcia, Surface plasmons in metallic nanoparticles: fundamentals and applications, *Journal of Physics D: Applied Physics*, **2011**, 44, 283001.
- [12] W. R. Erwin et al., Light trapping in mesoporous solar cells with plasmonic nanostructures. *Energy & Environmental Science*, **2016**, 9, 1577-1601.
- [13] V. Amendola et al., Physico-Chemical Characteristics of Gold Nanoparticles. *Comprehensive Analytical Chemistry*. Elsevier, **2014**, 66, 81-152.
- [14] M. Alvarez et al., Optical absorption spectra of nanocrystal gold molecules. *The Journal of Physical Chemistry B*, **1997**, 101, 3706-3712.
- [15] P. K. Jain, Plasmons in assembled metal nanostructures: radiative and nonradiative properties, near-field coupling and its universal scaling behavior, Georgia Institute of Technology, **2008**.
- [16] K. Uwe, and M. Vollmer, Theoretical considerations. Optical properties of metal clusters. *Springer*, Berlin, Heidelberg, **1995**, 13-201.
- [17] J. R. Krenn et al., Design of multipolar plasmon excitations in silver nanoparticles. *Applied Physics Letters*, **2000**, 77, 3379-3381.

- [18] V. Amendola et al., Surface plasmon resonance in gold nanoparticles: a review. *Journal of Physics: Condensed Matter*, **2017**, 29, 203002.
- [19] N. Harris et al., Tunable infrared absorption by metal nanoparticles: the case for gold rods and shells. *Gold Bulletin*, **2008**, 41, 5-14.
- [20] S. W. Prescott, Gold nanorod extinction spectra. *Journal of Applied Physics*, **2006**, 99, 123504.
- [21] P. K. Jain et al., Au nanoparticles target cancer. *Nano Today*, **2007**, 2, 18-29.
- [22] A. Candreva, Gold Nanoparticles: where shape becomes essence. Synthesis and characterization of an outstanding nanomaterial, *PhD Thesis, Dipartimento CTC Unical*, **2018**.
- [23] R.B. Wehrspohn et al., Photon management in solar cells. *John Wiley & Sons*, **2015**.
- [24] A. J. Haes et al. A nanoscale optical biosensor: sensitivity and selectivity of an approach based on the localized surface plasmon resonance spectroscopy of triangular silver nanoparticles. *Journal of the American Chemical Society*, **2002**, 124, 10596-10604.
- [25] S. Underwood et al., Effect of the solution refractive index on the color of gold colloids. *Langmuir*, **1994**, 10, 3427-3430.
- [26] <https://nanocomposix.com/pages/mie-theory-calculator>
- [27] L. De Sio et al., Active plasmonic nanomaterials. *CRC Press*, **2015**.
- [28] Z. Zhu et al., Plasmon-Enhanced Fluorescence in Coupled Nanostructures and Applications in DNA Detection. *ACS Applied Bio Materials*, **2018**, 1, 118–124.
- [29] C. Dahmen et al., Radiation damping in metal nanoparticle pairs. *Nano Letters*, **2007**, 7, 318-322.
- [30] A. S. H. Makhlof et al., Emerging Applications of Nanoparticles and Architectural Nanostructures: Current Prospects and Future Trends. *William Andrew*, **2018**.
- [31] M. J. Madou, *From MEMS to Bio-MEMS and Bio-NEMS: Manufacturing Techniques and Applications*. CRC Press, **2011**
- [32] A. Cunningham et al., Bottom-up Organisation of Metallic Nanoparticles. In *Amorphous Nanophotonics*. Springer, **2013**, 1-37.
- [33] S. Iravani et al., Synthesis of silver nanoparticles: chemical, physical and biological methods. *Research in pharmaceutical sciences*, **2014**, 9, 385.
- [34] S. E. Lohse et al., The quest for shape control: a history of gold nanorod synthesis. *Chemistry of Materials*, **2013**, 25, 1250-1261.
- [35] N. Li et al., Anisotropic gold nanoparticles: synthesis, properties, applications, and toxicity. *Angewandte Chemie International Edition*, **2014**, 53, 1756-1789.
- [36] P. Pallavicini et al., Gold Nanostar Synthesis and Functionalization with Organic Molecules. In *Gold Nanostars*, Springer, **2015**, 1-23.
- [37] N. D. Burrows et al. Anisotropic nanoparticles and anisotropic surface chemistry. *The journal of physical chemistry letters*, **2016**, 7, 632-641.

- [38] L. Scarabelli et al., Monodisperse gold nanotriangles: size control, large-scale self-assembly, and performance in surface-enhanced Raman scattering. *ACS Nano*, **2014**, *8*, 5833-5842.
- [39] J. S. DuChene et al., Halide Anions as Shape-Directing Agents for Obtaining High-Quality Anisotropic Gold Nanostructures. *Chemistry of Materials*, **2013**, *25*, 1392–1399.
- [40] J. E. Millstone et al., Controlling the Edge Length of Gold Nanoprisms via a Seed-Mediated Approach. *Advanced Functional Materials*, **2006**, *16*, 1209–1214.
- [41] L. Chen et al., High-yield seedless synthesis of triangular gold nanoplates through oxidative etching. *Nano Letters*, **2014**, *14*, 7201-7206.
- [42] G. Wang et al., High-yield halide-free synthesis of biocompatible Au nanoplates. *Chemical Communications*, **2016**, *52*, 398-401.
- [43] A. Lassenberger et al., Evaluation of high-yield purification methods on monodisperse PEG-grafted iron oxide nanoparticles. *Langmuir*, **2016**, *32*, 4259-4269.
- [44] W. Stöber et al., Controlled growth of monodisperse silica spheres in the micron size range. *Journal of colloid and interface science*, **1968**, *26*, 62-69.
- [45] Y. Han et al., Unraveling the Growth Mechanism of Silica Particles in the Stöber Method: In Situ Seeded Growth Model. *Langmuir*, **2017**, *33*, 5879-5890.
- [46] L. M. Liz-Marzán et al., Synthesis of nanosized gold- silica core-shell particles. *Langmuir*, **1996**, *12*, 4329-4335.
- [47] C. Graf et al., A general method to coat colloidal particles with silica. *Langmuir*, **2003**, *19*, 6693-6700.
- [48] T. Ogoshi et al., Organic–inorganic polymer hybrids prepared by the sol-gel method. *Composite Interfaces*, **2005**, *11*, 539-566.

Chapter 2

Organic and perovskite solar cells integrating plasmonic nanostructures

2.1 Introduction

The discovery of the photovoltaic effect, the process by which it is possible to convert sunlight into electricity, dates back to 1839 when Alexandre E. Becquerel observed the phenomenon during his studies on electrolytic cells^[1]. However, the development of the photovoltaic technology began in 1954, when a silicon based single p-n junction device with an efficiency of the 6% was reported by Chapin et al.^[2]. Since then, technological progress has led to the production of new photovoltaic devices based on different materials and architectures with the substantial objective to lower the cost of electricity produced^[3].

The different types of solar cells developed can be classified from a chronological point of view in first, second and third generation solar cells. First generation solar cells are based on crystalline silicon and they can reach an efficiency of 27.1%, if monocrystalline silicon is used, or 21.3% in the case of polycrystalline silicon^[4]. Nowadays silicon-based devices are predominant in the photovoltaic market although their fabrication costs are still relatively high. Indeed, the production of crystalline silicon requires high temperature processes with great energy consumptions and, therefore, it produces a significant environmental impact.

Second generation solar cells consist of thin-film solar cells based on amorphous silicon, cadmium telluride (CdTe) or copper indium gallium selenide (CIGS). The use of amorphous silicon has permitted to reduce significantly the production cost compared to the crystalline silicon. However solar cells based on amorphous silicon have lower efficiency^[5,6], around 13% and stability problems, because this material degrade upon long-term exposure to light^[7].

CIGS and CdTe solar cells permit to obtain higher efficiency, about 22%, but the high production costs and the presence of toxic Cd are the principal obstacles to their commercialization.

Third generation solar cells include Dye-Sensitized Solar Cells (DSSCs), Organic Solar Cells (OSCs), Quantum-Dot Solar Cells (QDSCs) and Perovskite Solar Cells (PSCs)^[8]. All these

emerging photovoltaic technologies show very interesting potentialities to reduce the cost of electricity production; in particular in this thesis work the attention was focused on OSCs and PSCs.

OSCs are based on the use of semiconducting organic polymers or small molecules. These cells have attracted a great interest because of their low production cost, lightweight, flexibility and for the compatibility of the fabrication processes with roll-to-roll technology to achieve large-scale production^[9]. The limiting factors of organic solar cells are still the low efficiency, generally below 10%, and the long term stability.

Perovskite solar cells are one of the most promising photovoltaic technologies because of their excellent performances and low cost. In few years the use of organolead halide perovskites has permitted to obtain solar cells with certified efficiency of 22.1%. The biggest challenges in this technology are improving the stability of perovskite and replacing toxic lead with a suitable nontoxic metal.

In the following, a brief discussion of the characterization of solar devices will be provided. After an overview of the main properties of organic and inorganic semiconductors, the principal organic device architectures and their working principles will be detailed discussed to explain the factors that limit their efficiency. The different strategies to exploit the beneficial plasmonic effects of metallic nanoparticles integrated in bulk heterojunction organic solar cell to enhance their efficiency will be presented and several pertaining works in literature will be considered. A description of perovskite materials, the main optoelectronic properties and the most common deposition methods used to fabricate solar cells will be given. The integration of plasmonic nanoparticles to reduce the thickness of the active layer and in turns the toxic lead content without reduce the efficiency of the devices will be discussed, with a particular attention towards plasmonic inverted perovskite solar cells.

2.2 Characterization of photovoltaic cells

2.2.1 Photovoltaic parameters

The performance of a solar cell is generally expressed through photovoltaic parameters that can be extracted from the current-voltage (I-V) curve obtained from the electrical characterization of the device under illumination. In practice, the I-V characteristic of a solar

cell is determined by measuring the currents generated as function of external voltages applied to the device. Since the current value depends on the active area of the photovoltaic device, the value of current density (J) is usually reported instead of the current. The current density is obtained by the ratio between the current and the active area.

An example of an I-V curve is shown in figure 2.1, where some of the photovoltaic parameters are reported.

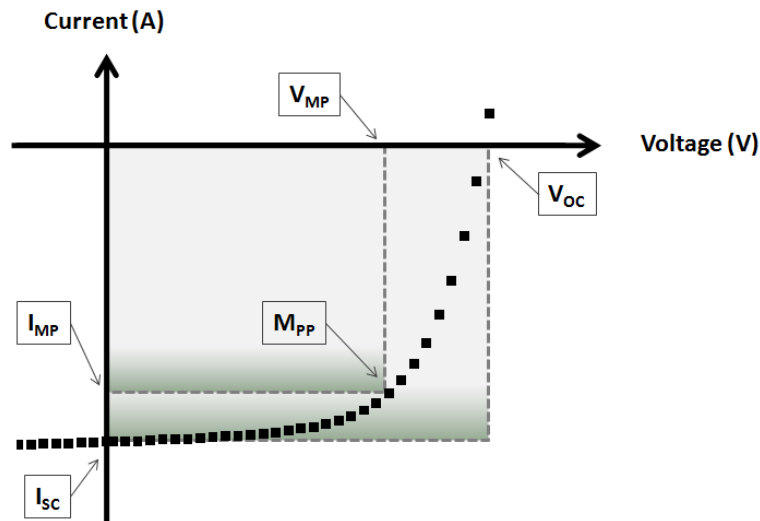


Figure 2.1 Typical I-V characteristic for a solar cell under illumination.

I_{sc} , the short-circuit current, is the electrical current that flows through the device under illumination when no external voltage is applied. V_{oc} , the open-circuit voltage, is the value of bias applied to the illuminated device at which no currents flows within it.

The operating regime of a solar cell is in the voltage range from 0 to V_{oc} , where it generates a power given by the equation:

$$P = I \times V \quad (2.1)$$

The maximum electric power (P_{MAX}) produced by the cell under illumination corresponds to the maximum power point (M_{PP}) shown in the characteristic curve.

At this point, the solar cell produces a current I_{MP} under an applied voltage of V_{MP} , therefore:

$$P_{MAX} = I_{MP} \times V_{MP} \quad (2.2)$$

The value of P_{MAX} corresponds to the area of the smaller rectangle indicated in figure 2.1, while the area of the bigger rectangle is the product $I_{sc} \times V_{oc}$, which is the theoretical maximum power (P_{TMAX}) that could be obtained from the cell.

The ratio between P_{MAX} and P_{TMAX} is called fill factor (FF):

$$FF = \frac{I_{MP} \times V_{MP}}{I_{SC} \times V_{OC}} \quad (2.3)$$

and it is a measure of the deviation of the behavior of a photovoltaic cell from that of an ideal diode. Graphically, the FF corresponds to the ratio between the area of the smaller rectangle and the area of the bigger one shown in the figure. It also represents the "squareness" of the I-V characteristics.

The power conversion efficiency (PCE or η) is the most commonly used parameter to compare the performances of solar cells. It is defined as the ratio between the maximum power (P_{MAX}) obtained from the solar cell and the power of the incident light (P_{IN}):

$$PCE = \frac{P_{MAX}}{P_{IN}} = \frac{I_{MP} \times V_{MP}}{P_{IN}} = \frac{FF \times I_{SC} \times V_{OC}}{P_{IN}} \quad (2.4)$$

The efficiency of a solar cell depends on the characteristic of the incident light; therefore, to compare the performance of different solar cells it is necessary to define the spectrum and intensity of the light. The graph of the spectral irradiance as a function of photon wavelength permits to characterize a light source^[10]. In figure 2.2 are reported the spectral irradiance spectra of the sunlight from 300 to 2600 nm in different conditions.

The spectral distribution of sunlight outside the Earth's atmosphere can be approximated to the emission of blackbody at 5800 K. In this condition the intensity of the light incident on a surface perpendicular to its direction is constant and correspondent to a value of 1353 W/m².

When sunlight pass through the atmosphere part of the radiation is scattered by aerosol and particulate matter present in it and absorbed by different atmospheric gases like oxygen, ozone, water and carbon dioxide, as evidenced in figure 2.2.

Therefore, the intensity and spectral distribution of sunlight depends strictly on the length of the atmosphere crossed and consequently also on the latitude and the month of the year. For these reasons, to uniquely identify the spectral distribution of the solar radiation considered, a parameter called Air Mass (AM) is used. It defines the optical path length of sunlight through the atmosphere to reach the Earth's surface.

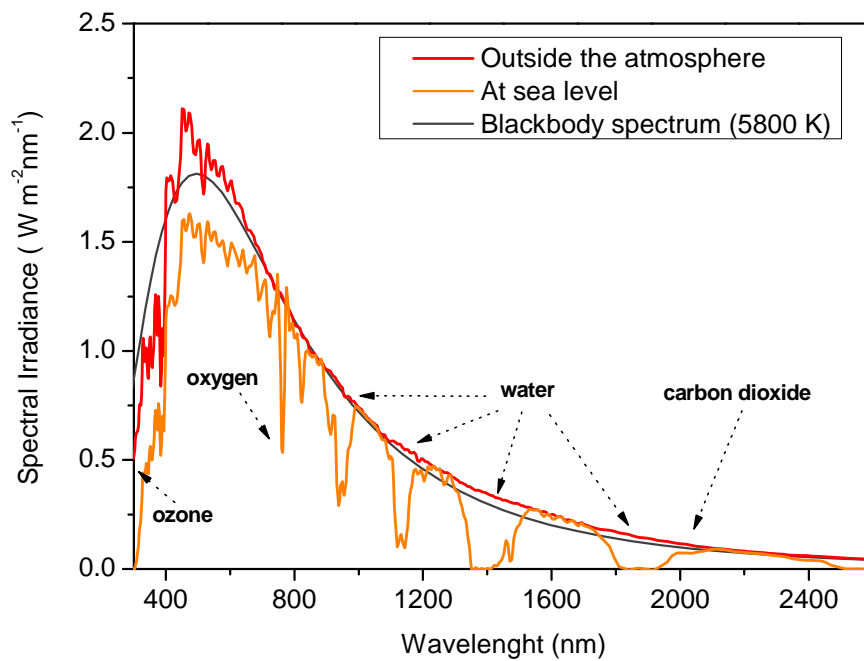


Figure 2.2 Solar irradiance spectra in different conditions. In the figure the impact of the atmospheric gases on the spectrum is highlighted.

The AM value is given by the equation 2.5:

$$AM = \frac{1}{\cos \theta} \quad (2.5)$$

where θ is the angle of between the incident sun's rays and a line normal to the earth horizon that goes straight up to the zenith.

AM0 indicates the spectral distribution of sunlight outside the Earth's atmosphere, while AM1 refers to the spectrum of sunlight at the sea level with the sun directly overhead (figure 2.3).

As a standard spectrum for solar cell characterization it was chosen AM 1.5 that corresponds to the sunlight incident on the earth surface at a solar zenith angle of 48.2° and with an irradiance of 1000 W/m^2 . Moreover, it can be distinguished between AM 1.5D and AM 1.5G, if the spectrum is relative only to the direct light from the sun or it includes also the light reflected and scattered by the Earth surface, respectively.

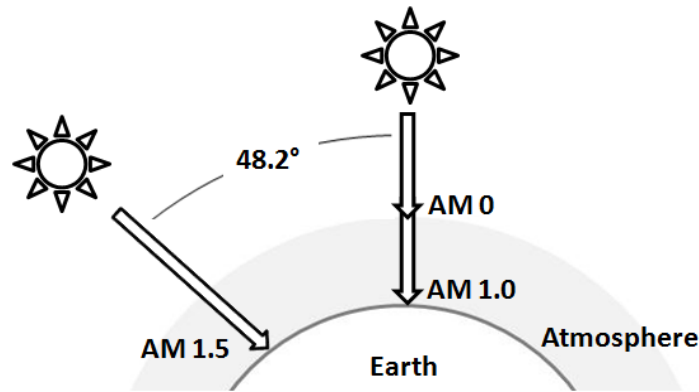


Figure 2.3 Illustration of the definitions of air mass indices.

2.2.2 Quantum efficiency

Another important photovoltaic parameter is the External Quantum Efficiency (EQE), also called Incident-Photon-to-Current Efficiency (IPCE). EQE is defined as the ratio between the number of photogenerated charges extracted out of the solar cell (N_e), under short-circuit condition, and the number of incident photons (N_{ph}) at a given wavelength. According to this definition, it can be calculated through the Equation 2.6:

$$EQE(\lambda) = IPCE = \frac{N_e}{N_{ph}} \quad (2.6)$$

EQE measurements permit to evaluate the optical and electrical losses that reduce the measured J_{SC} of a solar cell with respect to the maximum theoretical photocurrent^[11]. Optical losses are due parasitic absorption, reflection and transmission of photons that occurs at the interfaces or within the different layers of the cells, while electric losses come from recombination of charges in the device, thereby not all the photons absorbed by the active layer are converted into extracted charges^[12]. If the external quantum efficiency is integrated over the whole incident radiation spectrum, the total photocurrent of the cell (J_{SC}) can be obtained. Often, in addition to the EQE, another type of quantum efficiency is considered. This is the Internal Quantum Efficiency (IQE), which is the ratio of the number of charge carriers collected by the solar cell to the number of photons, of a given wavelength, absorbed by the active layer. Since IQE evaluates only the recombination losses, its value is always larger than the EQE.

2.2.3 Equivalent circuit of organic solar cells

An ideal solar cell can be modeled with an equivalent circuit composed of a current generator in parallel with a diode, as shown in Figure 2.4.

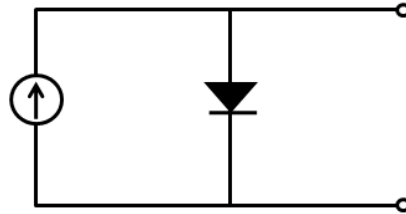


Figure 2.4 Representative equivalent circuit of an ideal solar cell.

In dark conditions the cell behaves like a diode as a consequence of the asymmetry introduced by the electrodes with different work functions. Under an applied voltage a current flows through the device (I_{dark}), that expressed in terms of current density (J_{dark}) is defined by the following equation^[13]:

$$J_{\text{dark}} = J_0 \left(e^{\frac{eV}{k_B T}} - 1 \right) \quad (2.7)$$

where J_0 is the reverse saturation current of a diode, e is the elementary charge, k_B is the Boltzmann constant, T is the temperature. The current density-voltage curve for a solar cell in the dark corresponds therefore to the exponential characteristic curve of a diode (figure 2.5).

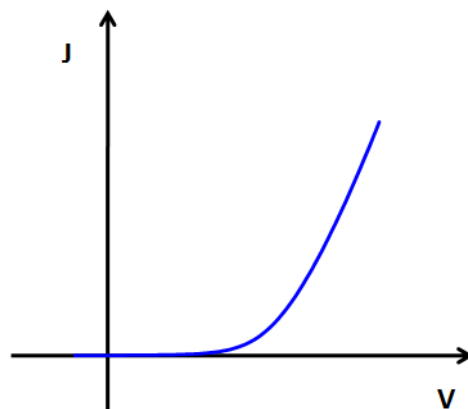


Figure 2.5 Dark current density-voltage curve for a solar cell.

Under illumination, a photocurrent (J_{ph}) proportional to the light intensity and with a direction opposite respect to that of the diode current is generated. By approximating the reverse current which flows in the illuminated cell with the current that flows in dark conditions, it is possible to determinate the overall current density $J(V)$ by the following equation:

$$J(V) = J_{ph} - J_{dark}(V) = J_{ph} - J_0 \left(e^{\frac{eV}{k_B T}} - 1 \right) \quad (2.8)$$

The approximation is known as superposition approximation and it is effective for many photovoltaic materials. As a result, under illumination the J-V curve is shifted in the fourth quadrant, as showed in figure 2.6 where power can be extracted from the cell.

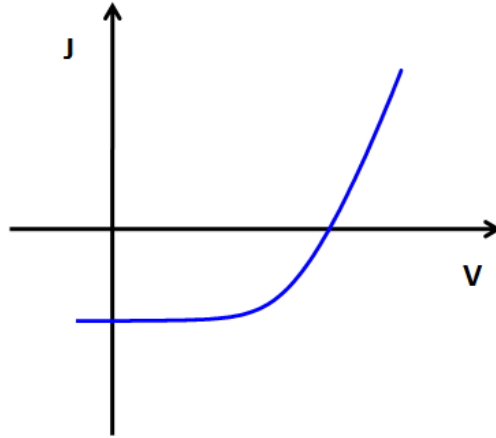


Figure 2.6 J-V curve for an illuminated solar cell.

To take into account these electrical losses, two terms are introduced in the equation, a series resistance (R_s) and a parallel (shunt) resistance (R_p). The equation became:

$$J(V) = J_{ph} - J_{dark}(V) = J_{ph} - J_0 \left(e^{\frac{e(V+JR_s)}{k_B T}} - 1 \right) - \frac{V + JR_s}{R_p} \quad (2.9)$$

In figure 2.7 is shown the correspondent equivalent circuit. The series resistance (R_s) derives from the intrinsic resistivity of the semiconducting materials and the contact resistances between the different materials in the multilayer structured solar cell. The value of R_s must be minimized as much as possible. The shunt resistance (R_p) is related to the loss of charge carriers through leakage paths due to structural defects like pinholes in the film or impurities

acting as charge recombination centers. The shunt resistance must be as high as possible in order to restrict the current leakage^[3].

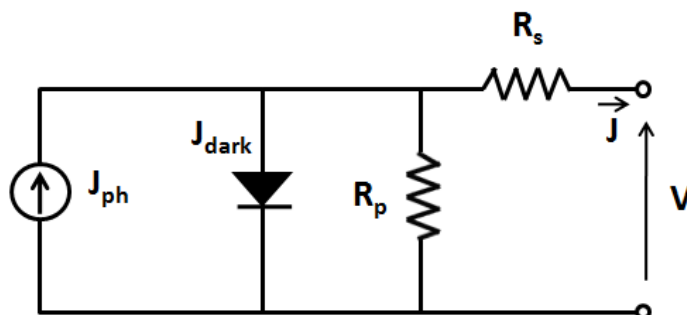


Figure 2.7 Equivalent circuit of a solar cell including series and shunt resistances.

The series resistance can be calculated from the inverse of the slope at the V_{OC} point in the J-V curve, while shunt resistance can be obtained from the inverse of the slope at the J_{SC} point in the characteristic curve^[14].

2.3 Inorganic and organic semiconductors

The chemical composition and the molecular order of the semiconductor used to prepare a photovoltaic cell govern the working mechanism of the cell since many different processes (i.e. charge conduction, charge generation, etc.) depend from these two properties. The different electronic structures between inorganic and organic materials, for example, drive to different operations and, consequently, to different performances.

To understand in detail this topic, it is advantageous to describe the distribution of electrons in terms of molecular orbitals. Considering a simple homonuclear diatomic molecule the constructive or destructive interaction between atomic orbitals results in bonding or antibonding molecular orbitals, respectively. In the first ones, the electronic density is located in the region between the nuclei and in this situation the system has a lower energy than non-interacting atoms, while in the latter the density is minimal between the nuclei resulting in an unstable state having higher energy. When a great number of atoms are close to each other in a way that their atomic orbitals can overlap, such in a crystalline lattice, an equal number of bonding and antibonding molecular orbitals is generated. As a consequence of the Pauli's principle, the bonding (or antibonding) orbitals have a slightly different energy from each other, so that they can be considered as a continuum of allowed states, an energy

band. The band originated from the bonding orbitals is called valence band, while the one relative to the antibonding is called conduction band. The energy gap between the two bands is the electronic band gap, E_g .

In organic semiconductors used for photovoltaics, the molecules are generally randomly oriented and interact between them by weak forces. Due the lack of a periodic structure the intermolecular orbital interaction is limited. As a consequence, the highest occupied molecular orbitals (HOMOs) and the lowest unoccupied molecular orbitals (LUMOs) can not form a continuum and they persist as discrete energetic levels without originate bands. The smallest difference in energy between discrete LUMO and HOMO molecular orbitals is defined optical band gap.

The difference in terms of electronic structure and dielectric constant between inorganic and organic semiconductor permit to understand their different charge transport properties. Inorganic semiconductors are characterized by charge mobility^[15] of $0.1-10^4 \text{ cm}^2 \text{ V}^{-1} \text{ s}^{-1}$. These high values are due to the easy charge transport through the material bulk. The charges are screened by the surrounding lattice thanks to the high dielectric constant of the material and are efficiently transported in its conduction band. In organic semiconductors the charges are more localized and are not enough screened by the surrounding molecules because of the low dielectric constant. Consequently, the charges induce a local polarization and a distortion of the lattice originating the polarons, which diffuse through a thermally activated hopping mechanism, less efficient with respect to the band transport. Indeed, the charge mobility^[16] of amorphous organic solids is generally of $10^{-5} -10^{-2} \text{ cm}^2 \text{ V}^{-1} \text{ s}^{-1}$.

In semiconductors, the absorption of a photon with energy equal or greater than the band gap leads to the formation of an exciton, which is a bound state of an electron and a hole. In organic semiconductors, as a consequence of the low polarizability reflected in a small dielectric constant ($\epsilon_r \approx 3-4$ for amorphous organic solids), the charges are not enough screened and therefore a strong bound electron-hole pair, named Frenkel exciton, is formed. In the case of inorganic semiconductors the electrostatic interaction between electron and hole is reduced due to the higher dielectric constant and polarizability of the materials (ϵ_r is generally greater than 10)^[17] resulting in a Wannier-Mott exciton. As an effect of the different intensity of electron-hole attraction, the Frenkel excitons have a smaller radius size and higher binding energy (E_B , i.e. the least amount of energy required to dissociate the

exciton in two free charges), compared to the Wannier-Mott excitons. In figure 2.8 the two types of excitons are schematized.

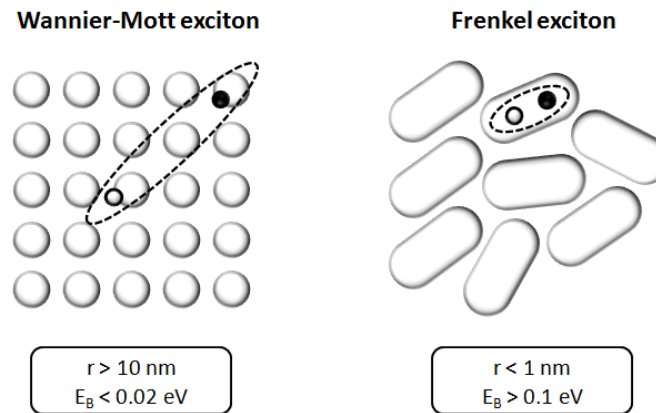


Figure 2.8 Schematic representation of Wannier-Mott and Frenkel excitons (hollow and filled circles represent holes and electrons, respectively).

At room temperature, the thermal energy is approximately 26 meV and this value is lower than the binding energy of a Frenkel exciton but greater than the one of a Wannier-Mott exciton. This means that at room temperature, photon absorption in inorganic semiconductors results in the formation of free charge carriers, while in organic semiconductors the generated Frenkel excitons remain bound and an additional energy is required for their dissociation.

2.4 Architectures of organic solar cells

2.4.1 Single Layer

The simplest organic solar cell architecture consists in an organic photoactive semiconductor comprised between two electrodes, one of which semitransparent, having different work functions^[18]. A schematic representation of a single layer OSC is shown in figure 2.9.

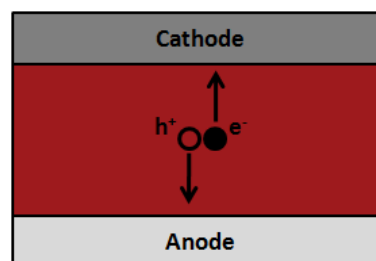


Figure 2.9 Schematic representation of a single layer OSC.

The organic material (p-type semiconductor) forms a Schottky junction with the metal having the lower work function (figure 2.10). Holes diffuse from the semiconductor to the metal and due to the smaller carrier density in semiconductor with respect to the metal a depletion region appears in the semiconductor^[19]. The generated electric field produces a HOMO and LUMO band-bending within the depletion region, supporting the dissociation of excitons photogenerated or diffused in it. Finally, the resulting electrons and holes are collected to the low and high work function electrodes, respectively.

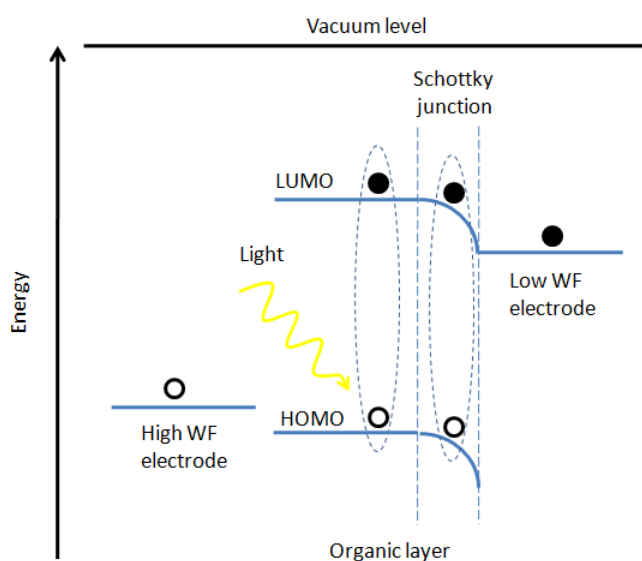


Figure 2.10 Energy diagram and operating principle of a single layer OSC (hollow and filled circles represent holes and electrons, respectively).

Since free charges move across the same material to reach the electrodes, their recombination losses are remarkable. Furthermore, due to the short exciton diffusion length, the excitons generated far away the depletion region recombine to the ground state without contribute to photocurrent production. As a consequence of both these detrimental processes and the low charge mobility of the organic materials, the efficiency of the single layer organic device is limited to 0.1%^[18].

2.4.2 Bilayer heterojunction

To overcome the limitations of the single layer organic solar cells, a planar bilayer heterojunction device structure was designed. A schematic representation of this type of cell structure is shown in figure 2.11.

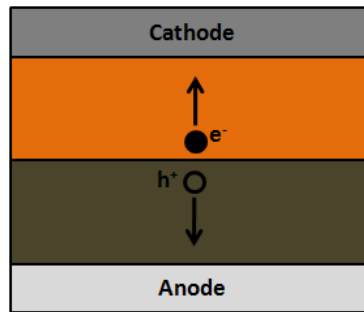


Figure 2.11 Schematic representation of a planar bilayer heterojunction OSC.

The photoactive bilayer consisting of p-type and n-type organic semiconductors, also defined as donor (D) and acceptor (A), is comprised between two electrodes whose work functions match respectively the donor HOMO and the acceptor LUMO energies, in order to efficiently extract the corresponding charge carriers (figure 2.12).

In the working condition, the photogenerated excitons (generally in donor) diffuse to the D/A interface, where their dissociation in free charges takes place thanks to their different chemical potentials.

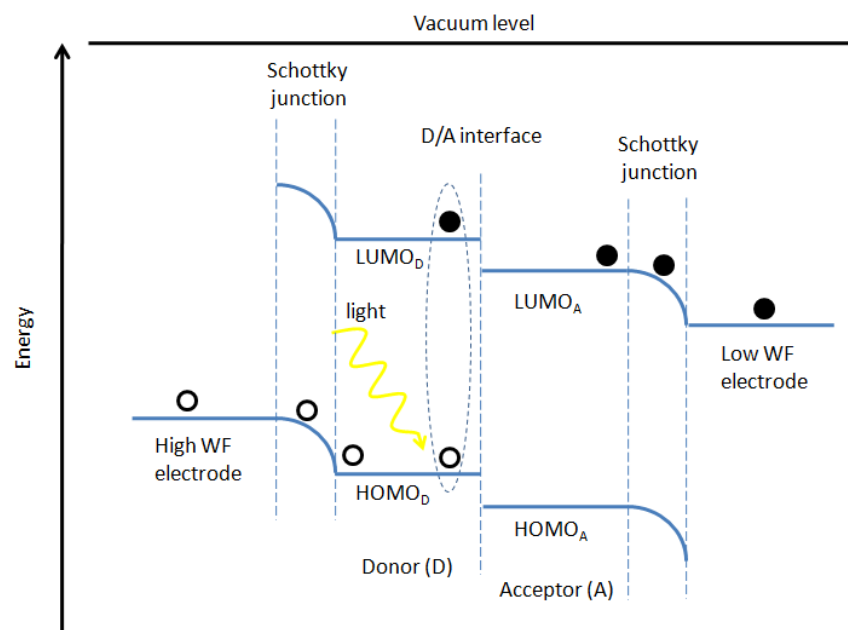


Figure 2.12 Energy diagram and operating principle of a planar bilayer heterojunction OSC (hollow and filled circles represent holes and electrons, respectively).

The electrons are transferred to the LUMO of the acceptor, while the holes remain in the HOMO of the donor. Successively, the free charges are driven to the respective electrode by the build-in electric field deriving from their difference in terms of work functions. The possibility for electron and holes to pass through different materials reduce the probability of charge recombination with respect to the single layer device. It is possible in this way obtain efficiency that are typically around 1%^[20,21,22,23].

The short diffusion length of the excitons and the reduced D/A interfacial area available for their dissociation into free charges are limiting factors for the efficiency of the bilayer heterojunction devices. Therefore, only the excitons generated at a distance from the D/A interface within about ten nanometers are separated. However, in order to efficiently harvest the sunlight, the active layer thickness should be of at least 100 nm, whereby the excitons generated at a distance greater than the diffusion length decay to the ground state and do not contribute to the charge generation.

2.4.3 Bulk heterojunction

The low efficiency of the bilayer heterojunction solar cells, substantially due to the high exciton losses, has stimulated the development of a new structure of the active layer known as bulk heterojunction (BHJ). The idea behind the BHJ is to simultaneously enhance the D/A interfacial area and reduce the diffusion pathway of the excitons to the interface in order to maximize their dissociation. The BHJ consists of bi-continuous interpenetrating networks of donor and acceptor materials obtained by exploiting the spontaneous phase separation of their mixture (figure 2.13).

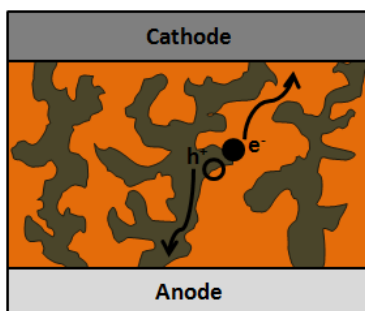


Figure 2.13 Schematic representation of a BHJ solar cell composed by two intermixed phases of a D (brown) and A (orange) material.

The phase separation must lead to domains, whose dimensions are comparable with the exciton diffusion length, fully percolated to form connected pathways in which the free

charges can easily travel to reach the electrodes. In this way, the efficiency of the solar device is greatly improved. Indeed, due to the reduced distance between the point in which the excitons are generated and the D/A interface, a great number of excitons is dissociated in free charges that can efficiently reach the electrodes through the continuous pathway of acceptor and donor. In addition, as nanodomains allow a wide contact area between the donor and acceptor, it is possible to increase the thickness of the photoactive layer with respect to single or planar bilayer devices. In this way, the light harvesting and the photocurrent generated are increased.

As explained above, the morphology of the BHJ is determinant both for the efficient exciton separation and for free charge collection at the electrodes. It is therefore necessary to optimize all parameters that influence the BHJ morphology. Obviously, the parameters change according to the technique used for the production of the film, which in turn depends on the type of material. In the case of molecular organic semiconductor, vacuum thermal evaporation is widely used, while for polymeric materials solution based processes, such as spin coating, are preferred. Molecular structure of the material, solvent, concentration of the solutions, donor/acceptor weight ratio are some key parameters for controlling the morphology of the BHJ deposited through solution-based processes.

Different methods such as thermal annealing, solvent vapor annealing and the use of a processing additive can also be used to optimize the morphology of the BHJ^[24]. Thermal annealing favors phase separation on nanometric scale and the crystalline reorganization of materials, leading to an increase of the interfacial area between the component of the active layer and to an enhancement of the charge-carrier mobility^[25,26]. Solvent-vapor annealing allows to weaken the intermolecular interactions and therefore to increase the polymer chains mobility that rearrange themselves in a more crystalline order^[27]. The enhancement of the crystallinity leads to an increase of the charge carriers mobility within the materials^[28] and to the broadening of their absorption spectra^[29], with evident ameliorating effects on solar cell efficiencies.

The addition of a small volume of co-solvent (processing additive) to the primary host solvent of the active layer blend solution permits to optimize the morphology of the active layer by controlling the phase separation between donor and acceptor^[24]. Two general criteria can be followed for the choice of the processing additive. In particular, it must have a

selective solubility for one of the components of the active layer (usually the acceptor) and must be less volatile than host solvent.

The structure of the BHJ could lead to the direct contact between a semiconductor (donor or acceptor) and the unsuitable electrode (cathode or anode, respectively) resulting in charge losses. To avoid this undesired process, charge transport layers are generally deposited between the active layer and the electrodes. The materials used with this aim must have several requirements^[30]:

- promote the formation of ohmic contacts between the electrodes and the active layer;
- have energy levels that improve charge selectivity at the corresponding electrodes;
- possess a large band gap in order to confine excitons in the active layer avoiding their quenching at the electrode/active layer interfaces;
- have a high conductivity to minimize the series resistive losses;
- have a low absorption in the spectral range of visible - near infrared to avoid optical losses;
- have chemical stability to avoid undesired reactions at the active layer/electrode interface.

2.5 Working mechanism of bulk heterojunction organic solar cells

The knowledge of the processes involved in the working of BHJ organic solar cells allows to identify the factors that limit their efficiency and to provide, therefore, the most appropriate solutions for the improvement of their performances. For this reason, in the following it will be discussed in detail the mechanisms that permit to convert the sunlight into electricity in such devices. The whole process can be divided in five steps, which are: (1) photons absorption with excitons generation; (2) excitons diffusion to the interface between donor (D) and acceptor (A) of electrons; (3) excitons dissociation into free charge carriers; (4) charge transport within the D or A toward the electrodes; (5) charge collection at the electrodes.

2.5.1 Photons absorption and excitons generation

When an organic solar cell is irradiated with sunlight, the photons travelling across the transparent electrode reach the active layer in which they are absorbed. Light absorption generates Frenkel excitons due to the transition of electrons from HOMO to LUMO orbitals in the donor material that generally is the main absorber.

The efficiency of the light absorption depends on the optical absorption coefficient of the materials, the spectral matching of the absorbers with the solar radiation and the optical thickness of the active layer. The absorption coefficient is related to the molecular electronic structure of the materials and to their packing and order in the photoactive film. Organic semiconductors have an absorption coefficient value at the maximum of the absorption spectra, generally located in the visible spectral range, of the order^[31] of 10^5 cm^{-1} . Therefore, films with a thickness of a few hundreds of nanometers, made with these materials, are able to absorb between 60% and 95% of the incident light^[32]. On the other hand, due to the short exciton diffusion length and low charge mobility of the organic materials, the optimal thickness of the active layer in solar devices is limited to 100 nm; thus it is not possible to achieve a complete light harvesting.

To have a high light absorption it is important to choose absorbers whose absorption spectra overlap with the solar radiation. Observing the solar irradiance spectrum, it can be noticed that a lot of energy is emitted in the infrared region. So a way to exploit this energy could be to use organic semiconductor that absorb in that range of spectral frequencies. With this aim, different semiconductors with a low band gap have been synthesized. However, by reducing the band gap the energy of the most energetic photons is lost as heat.

2.5.2 Exciton diffusion

The generated excitons have a lifetime before their decay through recombination mechanisms. Because the energy to overcome the binding interaction between electron and hole and to obtain free charges is provided by the energy difference in the electronic levels of the donor and acceptor materials, it is necessary that the exciton reaches the interface prior to decay. Exciton has no net charge and therefore it is not subject to the internal electric field due to the difference in the work function of the electrodes. Rather it diffuses from the point in which it is generated to the donor/acceptor interface and this process can be explained in terms of energy transfer from an excited donor molecule to an energy

acceptor molecule. Depending on the relative distance between the molecules involved in the process, it can be distinguished between Dexter (short-range) or Förster (long-range) energy transfer mechanisms.

The Förster energy transfer occurs via non-radiative dipole-dipole interaction between the donor and the acceptor. The efficiency of this process, that does not modify the spins of both molecules, is inversely proportional to the six power of the distance and therefore usually occurs within a distance of the order of 100 Å. The Dexter energy transfer mechanism requires an overlap between the frontier orbitals of the donor and acceptor and so it occurs only between adjacent molecules (distance in the order of 10 Å). It involves a direct “double electronic transfer” as can be observed in figure 2.14, resulting in the energy transfer between the molecules.

Exciton diffusion lengths in organic donor phases are usually in the range between 5 nm and 100 nm^[33,34].

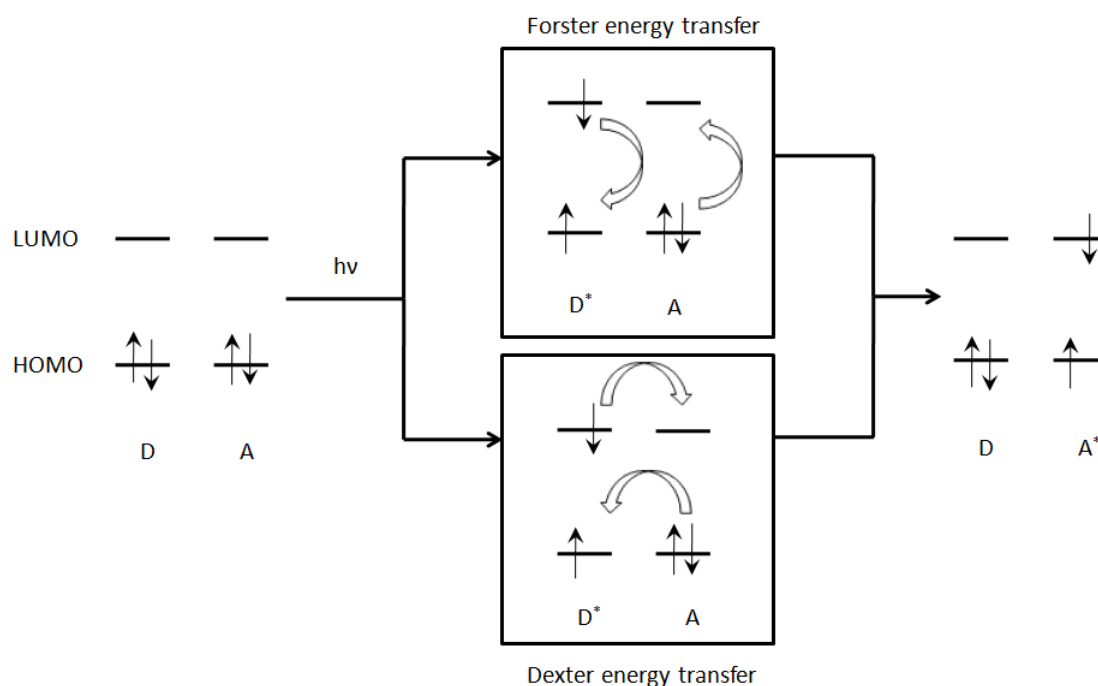


Figure 2.14 Schematic representation of Förster and Dexter energy transfer mechanisms.

2.5.3 Excitons dissociation at the D/A interface

Excitons that reach the D/A interface can dissociate into free charges. This process is energetically favored when the difference between the ionization potential of the donor and the electron affinity of the acceptor is greater than the exciton binding energy. Before dissociation into free charges, the exciton at the interface evolves into a charge transfer state (CT)^[35], in which the electron is located at the LUMO of the acceptor, while the hole is residing at the HOMO of the donor (figure 2.15).

Although spatially more separated with respect to the exciton state, the hole and electron are still bound together by the electrostatic attractive force. Therefore, to complete the separation process it is necessary an additional energy provided by the electric built-in field created using electrodes with different work functions at the two sides of the device. In presence of this field the charge separation occurs successfully, so electrons and holes are attracted towards their respective electrode where they are collect to generate photocurrent.

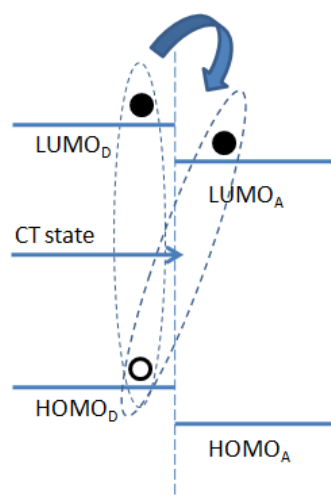


Figure 2.15 Schematic illustration of the formation of CT state at the D–A interface in an organic solar cell.

2.5.4 Charge transport to the electrodes

In organic amorphous semiconductors the free charges lead to the formation of polarons as a consequence of the localization of the charges on single molecules. Charge carrier transport takes place through a thermally activated hopping mechanism^[36]. The latter is less efficient with respect to the band transport that occurs in inorganic semiconductors. As a consequence, the charge mobility^[16] in amorphous organic semiconductors is in the range 10^{-5} - 10^{-2} $\text{cm}^2\text{V}^{-1}\text{s}^{-1}$, therefore a limited thickness of the active layer is required to have an

efficient charge transport towards the electrodes. In this way, the charge losses through bimolecular recombinations, which occur between free charge carriers of opposite sign coming from distinct photoexcitation events, are reduced. To limit the charge losses in organic solar cell, it is also important that the mobilities of hole and electron in the donor and in the acceptor are balanced. If this condition is not met, a space charge field is built-up^[37,38] due to a longer residence time of the slowest carriers and this leads to a reduction of the efficiency of the devices.

2.5.5 Charge collection at the electrodes

When the charge carriers reach the active layer/electrode interfaces, they are extracted by the respective electrodes. For this process to occur, the work function of the cathode should have a lower energy than the LUMO level of acceptor, while the work function of the anode should have a higher energy than the HOMO level of donor. To have a highly efficient process, the relative energy differences must lead to ohmic contacts. Theoretical calculations and experimental evidences have identified 0.3 eV as the optimal value for this energy difference^[39].

Aluminum (Al), calcium (Ca) and silver (Ag) are the most used material as electron extraction electrode because they have a low work function, while gold (Au), for its high work function, is used as hole extraction electrode. Generally, the transparent conductive electrode of the cell consists of Indium Tin Oxide (ITO) because of its high optical transmittance, electrical conductivity and wide band gap (>3.5 eV)^[40]; ITO, like gold, has a high work function.

Although the energetic alignment between organic semiconductors and electrodes is essential to have an efficient charge carrier extraction process, numerous defects at the organic layer/electrode interface, created during cell fabrication, can affect charge extraction. Interfacial charge-density redistribution, modification of surface roughness, chemical reactions and physical intermixing are some possible effects that may happen.

Another aspect to consider is the selectivity of the electrodes towards only one charge carrier in order to minimize the non-geminate charge recombination. Some strategies can be adopted to improve charge extraction; in particular, it is possible to pretreat the electrode on which the device is constructed (bottom electrode) before the deposition of the organic layer or to use interlayers (ILs) between the organic semiconductors and the electrode^[41,42].

Through the first method, the work function of the electrode is modified by chemical and/or physical processes^[43,44,45,46,47] performed on its surface, in order to improve the energetic matching with the charge transport levels of donor/acceptor materials.

The use of ILs lead to different advantages; depending on their main action mechanism, they can be classified as buffer or blocking layers: the first ones consist in organic or inorganic (oxides) materials that form a selective ohmic contact with the appropriate semiconductor of the active layer, while the latter selectively block the charge carrier transport. Both mechanisms lead to an improvement of charge extraction. Moreover, the insertion of the ILs can improve the stability of the cells, considering that the organic semiconductors are susceptible to chemical degradation in presence of oxygen, water and under ultraviolet illumination. The ILs can prevent these chemical reactions and at the same time avoid the diffusion of “hot” metal atoms into the active layer during the deposition of the top metallic contact, which can lead to shunting or electrical shorting of the organic devices and limit their lifetime^[48]. The ILs can also be used to control the polarity of the device^[41]. Two different geometries of organic solar cells can be fabricated, the normal and the inverted, depending on whether the electrode on which the cell is built (bottom electrode) is the anode (holes collector) or the cathode (electrons collector). The bottom electrode is generally constitutes by ITO. The possibility for ITO to act as anode or cathode is due to the use of appropriate interlayer materials. Poly(3,4-ethylenedioxythiophene)-poly(styrenesulfonate) (PEDOT:PSS) and zinc oxide (ZnO) are two examples of material that deposited on ITO allow to fabricate normal and inverted organic solar cell, respectively. In figure 2.16 the schematic representation of the two types of structure are reported, while in figure 2.17 are shown the corresponding energy level diagrams. P3HT:PCBM constitutes the active layer blend. P3HT, the donor, is poly(3-hexylthiophene-2,5-diyl) and PC₆₁BM, the acceptor, is [6,6]-phenyl C61 butyric acid methyl ester.

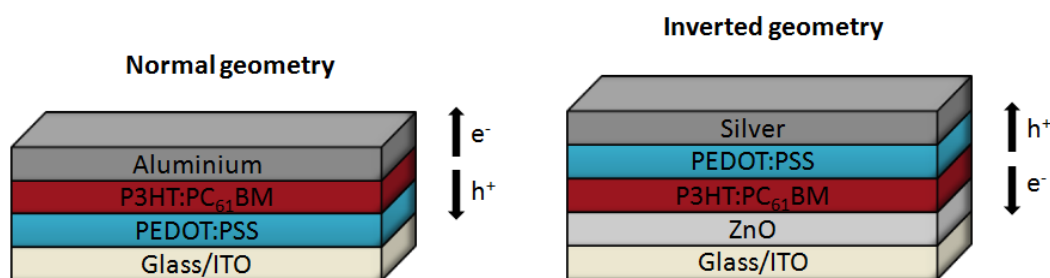
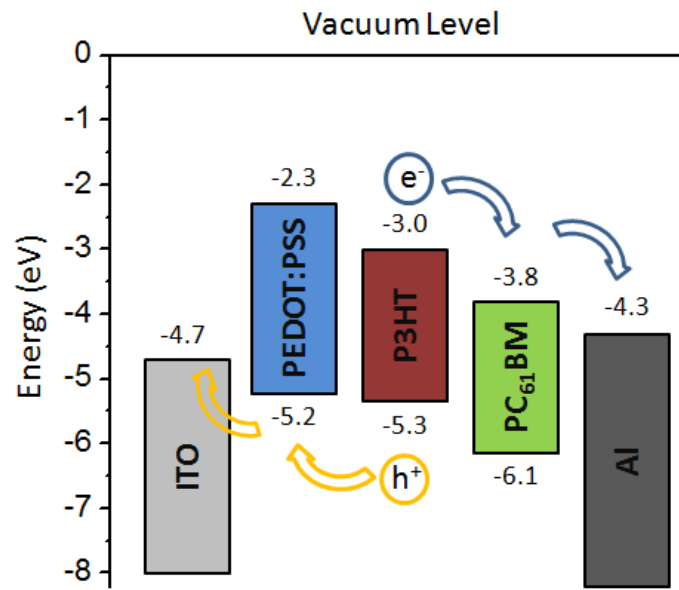


Figure 2.16 Schematic representations of normal and inverted organic solar cells.

(a)



(b)

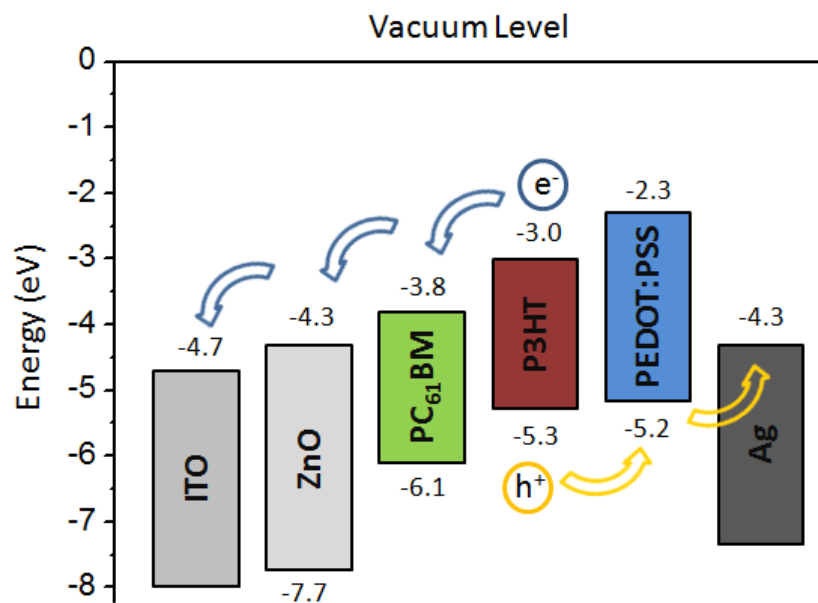


Figure 2.17 Energy level diagrams for regular (a) and inverted geometries (b).

2.6 Plasmonic enhanced organic solar cells

The poor charge transport properties of organic semiconductors together with the short exciton lifetime impose a limited thickness of the active layer of the organic solar cells. Consequently, a portion of incident light is not absorbed and the efficiency of the cell is reduced. Using light trapping strategies that allow to increase the light absorption without changing the thickness of the active layer is a promising approach. In particular, photonic

structures^[49,50,51,52], microlens arrays^[53], diffraction gratings^[54] and metallic nanostructures^[55,56,57] are effective means to improve the light harvesting. In this research work, the interest was focused on the integration of gold nanoparticles in solar cells in order to boost the performance of the devices by exploiting their plasmonic properties.

2.6.1 Plasmonic light trapping in organic solar cells

The improvement of light absorption in solar cells resulting from the incorporation of plasmonic nanoparticles can be obtained through three different approaches^[57].

In the first one plasmonic nanoparticles can be exploited as subwavelength scattering centers to trap and redistribute light into the active layer. An incident light beam perpendicular to the photoactive layer has a pathway inside the layer determined by its thickness. If subwavelength metallic nanostructures are appropriately incorporated into the cell, the light will be diffused angularly. As a result, the path of light in the active layer and therefore the probability of being absorbed will increase. Furthermore, the unabsorbed light that is reflected by the back electrode is partly blocked by the nanoparticles through multiple scattering and redistributed in the active layer before it can move away from the cell (figure 2.18).

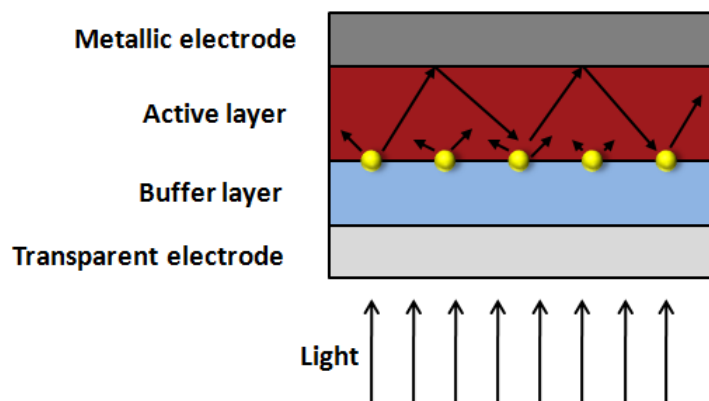


Figure 2.18 Light trapping by scattering from metal nanoparticles in a plasmonic solar cell.

To fully exploit the plasmonic scattering for improving the light absorption of the active layer, the location of the nanoparticles within the cell must be chosen appropriately. Indeed, if the nanoparticles are embedded in a homogeneous medium the light scattering is nearly symmetric in the forward and backward directions. Instead, if they are placed at an interface between two different layers, the light is preferentially scattered into the material with the higher dielectric constant.

The size and shape of the nanoparticles influence their scattering properties. In fact, if the dimensions of the metal nanostructures are too small compared to the wavelength of the incident light, a good part of it is absorbed by the particles and the dispersed fraction is limited. This will result in a decrease in the performance of solar cells. To exploit the light scattering properties of nanoparticles, size of at least 90 nm are generally required. Concerning the effect of the shape on the scattering properties of nanoparticles deposited at the interface between two materials, the fraction of light scattered in the material with higher dielectric constant increase when the shape of the nanostructures allow to maximize the contact area with this material^[58].

A second approach to improve light absorption in solar cells is to use plasmonic nanoparticles as subwavelength antennas. In conditions of LSPR, the nanoparticles store the incident energy in an electric field strongly confined near their surface (figure 2.19).

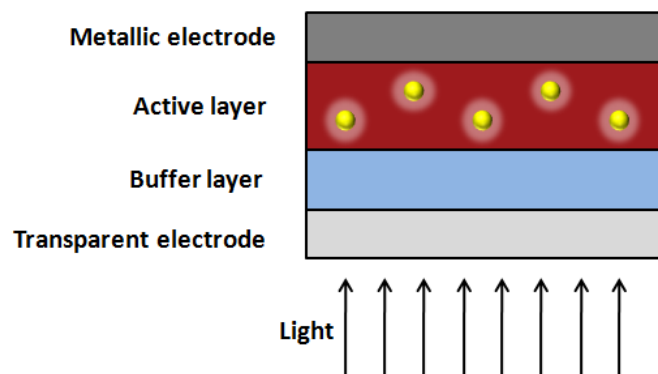


Figure 2.19 Light trapping by the excitation of localized surface plasmons in metal nanoparticles embedded in the solar cell.

This evanescent field produces an increase in the absorption cross-section of the materials that are affected by the field. Therefore, by positioning the nanoparticles near the active layer it is possible to enhance the amount of light absorbed by the cell. The effect of near-field enhancement is dominant for nanoparticle with size of 5-20 nm, whose plasmonic scattering effect is negligible. The intensity of the near-field also depends on the shape of the nanoparticles. Anisotropic nanoparticles such as nanorods, nanotriangles and nanostars have a higher polarizability than nanospheres. As a consequence their near-field is more intense and particularly concentrated at the edges and at the corners where the oscillating metal charges are highly confined^[59].

To fully exploit the near-field enhancement for increasing the light absorption of the active layer, the absorption rate of the semiconductors must be greater than the reciprocal of the plasmon decay time (lifetime $\sim 10\text{--}50$ fs)^[57]. If this condition is not satisfied, the energy absorbed by the metal is dissipated as ohmic damping. However, many organic and direct-bandgap inorganic semiconductors have high absorption rates.

The third plasmonic light-trapping mechanism involves the excitation of plasmons at a metal-dielectric interface that causes the formation of surface plasmon polaritons (SPPs), which are electromagnetic waves that propagate along the interface considered^[57]. The propagation length can be of hundreds μm , therefore the light absorption by the active layer can be remarkably enhanced. In the case of planar surface, the excitation of plasmons does not generate SPPs due to a momentum mismatch existing between the photons and the SPPs^[60]. This mismatch can be avoided by depositing a periodic array of nanoparticles at the metallic-dielectric interface (figure 2.20), because they can provide the additional in-plane momentum to the incoming light that permit to generate the SPPs^[61].

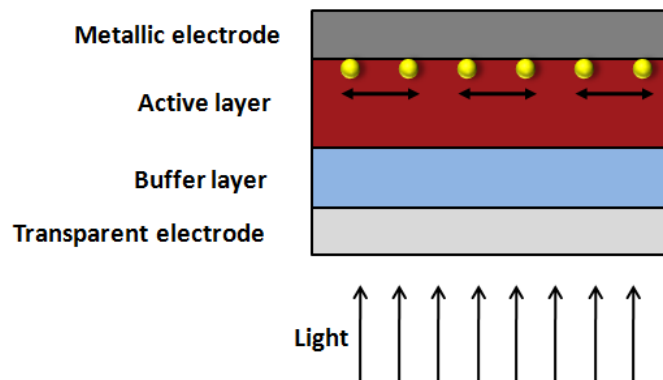


Figure 2.20 Light trapping by the excitation of surface plasmon polaritons.

By controlling the geometrical parameters of the nanoarray, including the period, the height and width of nanoparticles, it is possible to obtain the best condition for the SPPs excitation and in turn of absorption enhancement.

2.6.2 Beyond light harvesting effect induced by plasmonic nanoparticle in organic solar cells

The incorporation of plasmonic nanoparticles into solar cells can produce an improvement in their performance as a result not only of optical effects but also of electrical ones. In several works reported in literature, the presence of plasmonic nanoparticles in solar devices leads

to an increase in the exciton dissociation efficiency^[61,62,63,64]. Although the mechanism has not been fully understood, it has been reported that the coupling between excitons and plasmons leads to an increase in the amount of excitons in high-energy states that dissociate more efficiently than relaxed excitons^[63].

Other electrical effects related to the presence of metallic nanoparticles in organic solar cell are the reduction in the series resistance of the devices and the enhancement of charge carrier mobility of the semiconductors. The latter effect is explained considering that nanoparticles introduce energy levels within the band gap of the semiconductors that provide additional hopping sites for charges and thus improve charge mobility^[65].

Plasmonic nanoparticles can lead to an improvement of the device performances by promoting the increasing of the exciton/charge generation rate near the electrode where the charges with the lower mobility are collected. Generally, in organic device the holes have a lower mobility than electrons. Therefore, by locating the nanoparticles in the hole transport layer it is possible to improve the balancing of charge carrier transport obtaining an increase of the FF of the devices^[66]. The presence of nanoparticles in organic device can lead to an enhancement in the structural and morphological stability of the active layer blend, resulting in a slowed down degradation of the device under prolonged illumination^[67]. Plasmonic nanoparticles integrated in solar cells can produce multiple effects on their properties and performances; unfortunately, not all are beneficial effects. Indeed, numerous problems such as morphology change^[68], excitation quenching^[62,68,69] and increased charge recombination^[54] can occur. These loss mechanisms can be so important that the performance of the plasmonic device can be lower than that of the device without nanoparticles. Therefore, to obtain an enhancement in the performance of solar cells through plasmonic nanoparticles it is essential to consider all the possible mechanisms involved and adopt the most appropriate strategies to favor the improvement mechanisms and reduce the loss effects.

2.6.3 Plasmonic organic solar cells

Plasmonic nanoparticles can be integrated within organic solar cells in different positions^[70]: nanoparticles embedded in the photoactive layer, in the buffer layers and at the interfaces (figure 2.21).

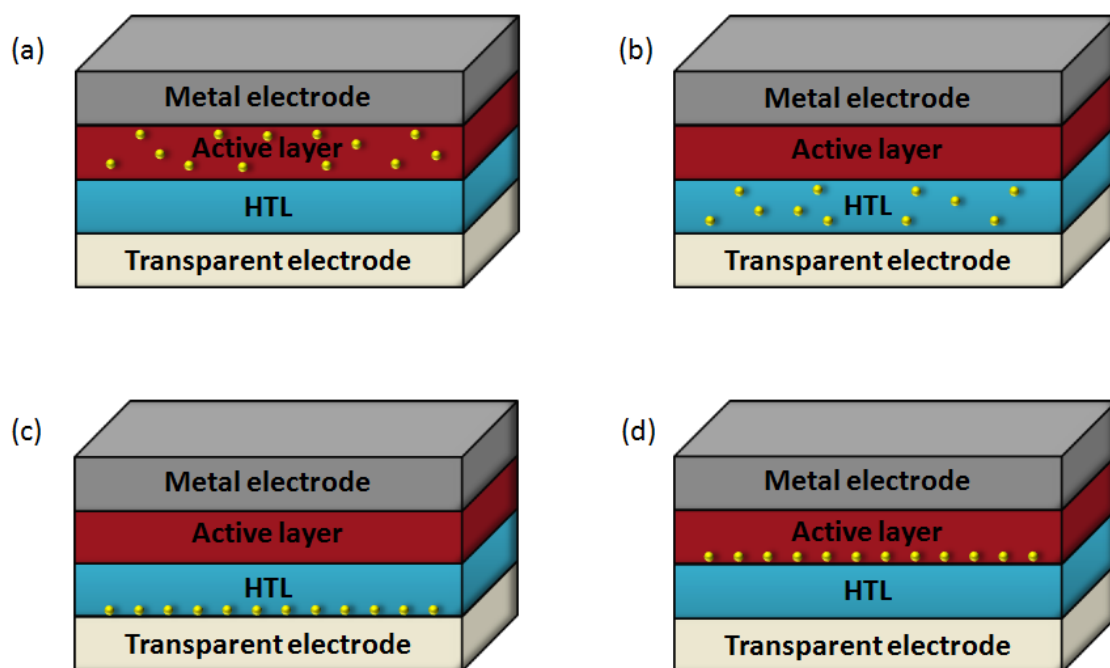


Figure 2.21 Schematic design of plasmonic organic solar cells in which the nanoparticles are integrated in different positions. Nanoparticles in photoactive layer (a), nanoparticles in Hole Transport Layer (HTL) (b), nanoparticles at transparent electrode /HTL interface (c) and at HTL/photoactive layer interface (d).

Nanoparticles in the photoactive layer

The incorporation of plasmonic nanoparticles in the active layer permits to exploit the effects of light scattering and near-field deriving from the LSPR to enhance the light absorption. The relative contribution of the two effects on the improvement of light harvesting will depend on the material and the geometrical properties of the nanoparticles used. The integration of plasmonic nanoparticles in the active layer could be the most promising strategy to increase the absorption of light in plasmonic solar cells. However, some works reported in literature show a decrease in cell efficiency following the integration of the nanoparticles in the active layer due to competitive effects. Topp et al.^[71] demonstrated that using dodecylamine-capped Au nanoparticles, the ligand coating leads to undesired exciton quenching, via nonradiative energy transfer between the nanoparticles and the active layer, which suppress the plasmonic improvement effects. In a further

work^[72] it was shown that the presence of the ligand (tetraoctyl ammonium bromide) on the surface of gold nanoparticles leads to the deterioration of the active layer morphology, whereby, although an increase of light absorption is observed, the performance of the devices result lower with respect to the reference without nanoparticles. Xue et al.^[68] reported that the addition of Ag nanoparticles in the active layer of organic solar cells produces an increase of both the light absorption and the charge carrier mobility. However, since the nanoparticles act as charge carrier recombination centers, no improvement in the efficiency of solar cells was observed. To prevent charge recombination when metallic nanoparticles are integrated in the active layer, a coating of an insulating material can be used^[73]. On the other hand, the presence of the insulating shell reduces the influence of plasmonic effects on the active layer because the near-field decays with the distance from the metallic core. The thickness of the shell, therefore, must be carefully optimized. A promising strategy to limit the adverse effect of exciton quenching is the use of metallic nanoparticles produced by laser ablation in liquids that are free of surfactants or passivating layers^[70]. It was demonstrated^[74] that the incorporation of surfactant-free Au nanoparticles within the active layer of organic solar cells leads to an enhancement of the device performance of 40% attributed to near-field and scattering effects.

Nanoparticles in the hole transport layer

The integration of plasmonic nanoparticles in the hole transport layer of organic solar cells is an effective strategy to improve the efficiency of the devices. It permits to avoid the problems of exciton quenching and disturbance of active layer morphology that can occur when nanoparticles are incorporated in the active layer. Chen et al.^[75] reported that by embedding Au nanoparticles in the HTL of organic solar cells, an improvement of 20% of their efficiency was observed. As a consequence of the local enhancement in the electromagnetic field due to the LSPR, the rate of exciton generation and the probability of exciton dissociation resulted improved, justifying the increase of J_{SC} and FF of the plasmonic devices. Fung et al.^[76] studied the optical and electrical effects produced by Au nanoparticle embedded in the HTL of organic solar cells. They demonstrated that the increase of device efficiency of 13% after the integration of the nanoparticles was not related to plasmonic effects. Indeed, the field enhancement near the metallic nanoparticles was mainly distributed along the HTL layer rather than vertically into the adjacent active layer, whereby no

increase of light absorption was observed. The improvement of the efficiency of the devices was related essentially to electrical effects produced by the nanoparticles which led to an enhancement of the HTL conductivity and the hole collection efficiency. The latter was a consequence of the larger contact area between the active layer and the HTL as an effect of the increased interfacial roughness due to the incorporation of the nanoparticles.

The effects of the integration of Au nanostructures with various sizes and shapes (nanospheres and nanorods) in the HTL of organic solar cells were investigated in a further work^[77]. The authors demonstrated that the improvement of the efficiency of the devices was essentially related to the near-field enhancement of the nanoparticles and that the possibility to exploit complementary plasmonic bands, covering a wide absorption region of the active layer, allowed to obtain an efficiency enhancement up to 24%. No significant variation in conductivity of the HTL after the addition of nanostructures was observed.

Kozanoglu et al.^[78] studied the effects of the integration of various morphologies of gold nanoparticles in the HTL of organic solar cells. They observed an increase of the efficiency of 29% with Au nanostars, 14% with Au nanorods and 11% with Au nanospheres compared to the device without nanoparticles. The efficiency enhancement was explained for all the nanoparticles as the sum of the contributions of light trapping improvement, due to plasmonic effects of near-field and scattering, and reduced series resistance deriving from the greater conductivity of nanoparticles with respect to the HTL. The best results obtained in the case of Au nanostars were related to their bigger size compared to the other nanoparticles, whereby they produced a greater light scattering, and to the presence of the tips near which local field is extremely high due to lightning rod effect.

Nanoparticles at the interfaces

Most of the works in literature concerning the integration of plasmonic nanoparticles between the different layers of the organic solar cells are aimed at the fabrication of devices in which the nanoparticles are deposited at the transparent electrode (TE)/ HTL interface or at the HTL/active layer interface.

Gao et al.^[79] reported the integration of Au nanospheres of different sizes at the TE/HTL interface of organic solar cells. The best efficiency improvement was of 16% and it was observed when nanoparticles with the biggest size were used. In that case the nanoparticles had a diameter bigger than the thickness of the HTL, therefore they protruded in the active

layer; consequently the laterally distributed near-field of the nanoparticles affected the light absorption of the active layer, leading to an increase of light absorption. The authors excluded the influence of electrical effects because of the slight reduction in device series resistance after the integration of the nanoparticles. Shahin et al. fabricated plasmonic organic devices in which Au nanoparticles were attached to a silanized TE through a self-assembly technique^[80]. By optimizing the surface coverage they demonstrated an enhancement of absorption and efficiency of 65% and 30%, respectively, due to the effects of plasmonic near-field on the active layer.

Yan et al.^[81] reported the incorporation of Ag nanoparticles at the HTL/active layer interface of organic solar cells. By optimizing the density of the nanoparticles on the HTL they demonstrated an efficiency enhancement of about 17%, resulting from the increase of the light absorption of the active layer and the exciton dissociation as effects of the near-field of the nanoparticles at LSPR.

The incorporation of plasmonic nanoparticles at the HTL/active layer interface permits to fully exploit the effects of light scattering and near-field in order to improve the light harvesting of the devices. However, competitive harmful effects such as exciton quenching may occur, limiting the efficiency improvement of the plasmonic devices.

Stratakis et al.^[82] accomplished the integration of surfactant-free Au nanoparticles at the HTL/active layer interface in organic solar devices. An efficiency improvement of 16% of the devices incorporating the nanoparticles with respect to the reference was attributed to the increase of the exciton generation and dissociation rate resulting from the plasmonic field of the nanoparticles.

2.7 Perovskite for photovoltaic applications

2.7.1 Structure and composition

The term perovskite was coined by Gustave Rose in 1840 to name the mineral form of calcium titanate (CaTiO_3) that he discovered in Ural Mountains^[83]; he assigned this name in honor of the Russian mineralogist Lev Perovski. Later the term was extended to all compounds with ABX_3 stoichiometry having the same crystalline structure of CaTiO_3 . In the cubic unit cell, the large cation A resides at the eight corners of the cube, while the small cation B is located at the body center that is surrounded by 6 anions X (located at the face centers) in an octahedral $[\text{BX}_6]^{4-}$ cluster^[84] (figure 2.22).

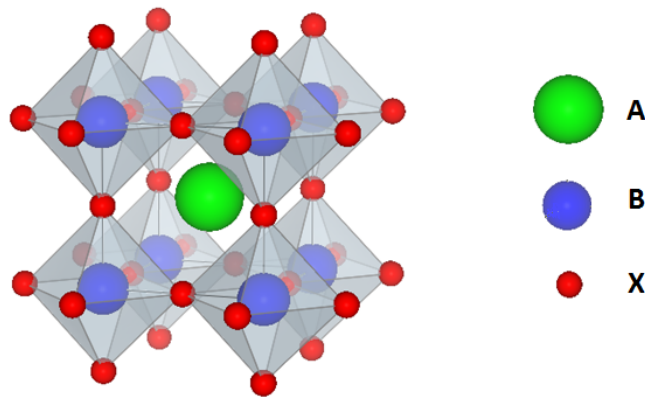


Figure 2.22 Structure of perovskite with general chemical formula ABX_3 ^[85].

The existence of numerous natural and synthetic perovskites is made possible by the adaptability of perovskite lattice towards A, B and X site substitutions. However, these substitutions are tied to geometrical restrictions. To predict the stability of a 3D perovskite structure, a semiempirical geometric parameter, the Goldschmidt tolerance factor (t), can be used:

$$t = \frac{r_A + r_X}{\sqrt{2}(r_B + r_X)} \quad (2.10)$$

where r_A , r_B , and r_X are the ionic radii of the A, B cations and X anion, respectively.

Materials with a tolerance factor of 0.9–1.0 have an ideal cubic structure, while if it is comprised in the range 0.71–0.9 a distorted perovskite structure with tilted octahedral is expected^[86]. For value of tolerance factor below 0.71 or above 1.0 the perovskite structure is

not formed. Although the Goldschmidt's rule was developed for oxide perovskite, its trend well adapted for hybrid inorganic–organic halide perovskite materials^[87,88]. In particular, the last ones tend to form an orthorhombic structure when $t < 0.8$, a cubic structure when $0.8 < t < 1$, and a hexagonal structure when $t > 1$.

Another important geometrical parameter that must be considered is the octahedral factor (μ), which describes the stability of the BX_6 octahedron.

$$\mu = \frac{r_B}{r_X} \quad (2.11)$$

If the octahedral factor is comprised in the range $0.442 \leq \mu \leq 0.895$ the formation of perovskite framework is expected^[89,90]. It was demonstrated, however, that both factors are necessary but not sufficient conditions because additional geometrical restrictions should be considered to predict more accurately the formation of the perovskite lattice.

The versatility of the perovskite structure towards A, B e X site substitutions has led to a plethora of synthetic materials having ferroelectric, magnetoelectric, antiferroelectric, ferromagnetic, semiconductive and superconductive properties^[91].

For their unique optoelectronic properties hybrid organic-inorganic perovskites are one of the most interesting materials for solar cell fabrication. In particular, the most performing class of compounds is that in which A cation is a monovalent organic cation (typically $CH_3NH_3^+$, $C_2H_5NH_3^+$, $HC(NH_2)_2^+$), the cation B is a group IVa divalent metal ion such as Pb^{2+} or Sn^{2+} , while the X anions are halide (Cl^- , Br^- , I^-)^[84]. Among these perovskite, $CH_3NH_3PbI_3$ is the most extensively studied hybrid perovskite for use in solar cells.

2.7.2 Optoelectronic properties

Organic-inorganic hybrid halide perovskites have several unique properties particularly interesting for photovoltaic applications. These materials have a large optical absorption coefficient and a wide and tunable absorption window. For instance, $CH_3NH_3PbI_3$ has an absorption coefficient greater than $3.0 \times 10^4 \text{ cm}^{-1}$ in the visible region^[92,93]. This value is comparable with that of organic semiconductors commonly used in highly efficient organic solar cell devices^[94,95,96].

High optical absorption in halide perovskites derives from the existence of a direct bandgap $p-p$ transition that is stronger than the $p-s$ transition present in other material used in thin-

film solar cells^[93]. The light harvesting properties of perovskites allows to reduce the active layer thickness in the range of 300-600 nm, which is three order of magnitude thinner respect to that of a silicon solar cell. This leads to both a significant reduction in the cost of material and an improvement of the charge carrier transport in the devices. Indeed, since the path of photogenerated carriers to reach the electrode is reduced, the probability of charge recombinations decreases.

Another very interesting peculiarity of perovskites is that by modifying their structure or composition it is possible to tune their band gap.

The substitution of the A-cation does not produce significant variations to the band structure of perovskite^[97] unless the incorporated cation produces distortions in the perovskite lattice as a consequence of its size. In this case the electronic properties of the perovskite and therefore the band gap will change^[98,99].

Organohalide lead perovskites are the most performing perovskites for photovoltaic application. Although it was proposed the Pb²⁺ substitution with a series of univalent, bivalent and trivalent ions^[100], only Sn²⁺ represent at the moment the most promising alternative^[101,102,103]. Lead-free MASnI_{3-x}Br_x has interesting optoelectronic properties, such as narrow bandgaps (1.2–1.4 eV)^[104] and high charge carrier mobilities in thin films^[105,106]. However, the stability of the perovskite is notable reduced^[107,108] due to the tendency of Sn²⁺ to oxidize into Sn⁴⁺.

X-site anion replacement produces the greatest effect on the optical properties of the organohalide lead perovskite. In particular, the bandgap monotonously decreases in the series of Cl⁻ > Br⁻ > I⁻ and this effect is due to the fact that the halide p orbitals have a large contribution to the valence band of perovskite. The replacement of iodine with bromine in CH₃NH₃PbI_{3-x}Br_x allows to modulate the band gap^[109] between 1.6 eV (x = 0) and 2.3 eV (x = 3). In the case of MAPbI_{3-x}Cl_x the miscibility of Cl⁻ with I⁻ is limited to about 5%^[110] because of the high ionic size mismatch between the two halide^[111].

In organohalide perovskites the light absorption leads to the generation of Wannier-Mott excitons^[112]. The exciton binding energy of CH₃NH₃PbI₃ was determined by spectroscopic measurement and its value is 16 meV at low temperatures, while it decreases to few meV at room temperature^[113]. This value is much lower than the thermal energy at room temperature (about 26 meV). Therefore, a spontaneous generation of free charges occurs

after light absorption and this explains the high performance of the perovskite-based devices.

A very interesting peculiarity of the perovskite materials for photovoltaic applications is that they have both high charge carrier mobility and ambipolar charge transport^[84,114]. Quenching experiments through femtosecond transient optical spectroscopy allowed to establish balanced and long-range electron-hole diffusion lengths of at least 100 nm for solution processed $\text{CH}_3\text{NH}_3\text{PbI}_3$ ^[115]. In further investigations on mixed halide $\text{CH}_3\text{NH}_3\text{PbI}_{3-x}\text{Cl}_x$, charge diffusion length of over 1 μm was measured^[116].

It was demonstrated that the long charge carrier diffusion length values are related to the kinetics of the recombination mechanisms^[117]. In particular, both monomolecular (deriving from geminate recombination of excitons and/or from trap- or impurity-assisted recombination) and bimolecular charge carrier recombination rates are extremely low in organohalide perovskite. Auger recombination, although characterized by high rate, is a relevant process only at high light intensity^[118].

Another important property of organohalide perovskites is their defect tolerance^[119]. While very low trap densities of the order of 10^{11} cm^{-3} have been reported for $\text{CH}_3\text{NH}_3\text{PbI}_3$ single crystals^[120,121], in the case of polycrystalline thin films used in efficient solar cells the value increase^[122,123] up to 10^{16} cm^{-3} . This high trap density value should result in a remarkable deterioration of the efficiency of the cells. However, the devices show unexpected high performances. Several first-principles investigations^[93,124,125,126,127] carried out on the nature of defects in $\text{CH}_3\text{NH}_3\text{PbI}_3$ have led to the conclusion that native defects introduce only shallow states in the perovskite band gap^[120], which explain the defect tolerance in perovskite.

2.8 Perovskite thin film deposition

The quality of the perovskite film has a crucial impact on the performance of photovoltaic devices. Indeed, the impressive improvements of efficiency of the perovskite based solar cells have been possible thanks to the development and the optimization of deposition methods that permit to prepare high-quality lead halide perovskite thin films. The deposition strategies can be divided in vapor deposition methods and solution deposition methods. In the following a description of the principal ones will be given.

2.8.1 Co-Evaporation method

Co-evaporation is a vapor method in which the perovskite precursors are thermally evaporated simultaneously from two separate sources and react on the substrate to produce the perovskite film. This method allows to obtain compact and uniform perovskite films regardless of the wetting properties of the layer on which it is deposited^[128]. Moreover, by co-evaporation it is possible to control precisely the thickness and morphology of the films with an excellent reproducibility. However, this method requires high vacuum condition and consequently high equipment costs. For these reasons solution methods are generally more adopted because of their low cost and versatility.

2.8.2 One-Step Solution methods

In one-step methods a solution of the perovskite precursors, consisting of a metal halide and an organohalide in appropriate solvent, is directly deposited on the substrate. During the deposition, generally carried out by means of spin-coating technique, the evaporation of solvent excess leads to a supersaturated solution and so to the crystallization of the solid perovskite film^[129,130].

Because both processes (solvent evaporation and crystallization) occur simultaneously, it is difficult to obtain uniform and high quality perovskite film due to its shrinkage. Often, the film appears opaque indicating a rough surface with the presence of undesired pinholes^[131]. This limitation can be overcome by controlling the velocity of the crystallization process. In particular, retarding the crystal growth a smooth precursor film is obtained, followed by its slow crystallization to form the perovskite. On the other hand, a high-quality perovskite film can also be produced by accelerating the crystallization of the perovskite before the complete evaporation of the solvent^[129].

The crystallization process can be effectively retarded by controlling the solvent or through the use of additives in precursor solution. The solvent usually employed are high boiling point polar aprotic solvents such as γ -butyrolactone (GBL), dimethylformamide (DMF) and dimethyl sulfoxide (DMSO). Compared to DMF and GBL, DMSO interact with PbI_2 forming a strong adduct DMSO-PbI_2 that retard the crystallization of the perovskite^[132,133].

The use of MACl or NH_4Cl as additives in the precursor solution leads to a significant improvement in the morphology and coverage of the perovskite film compared to the unmodified solution. Unexpectedly, there are no measurable amounts of chlorine in the final

perovskite film deposited from the precursor solution that incorporates these additives. Therefore, they interfere during the formation of the perovskite slowing its crystallization, but they are completely removed in the annealing step. This is possible because these additives have a low sublimation temperature^[129].

The strategy to enhance the perovskite crystallization rate is another interesting way to obtain high quality perovskite films through one-step solution methods. The fast crystal growth can be induced through the use of a solvent that is miscible with the solvent of the precursors of perovskite but that is a non-solvent (anti-solvent) for the precursors. Toluene, chlorobenzene, dichlorometane are the most used. The anti-solvent dripped during the spin coating of the perovskite precursor solution allows to obtain uniform supersaturation conditions that lead to the rapid formation of the perovskite film^[129]. To obtain high quality perovskite film all dripping conditions must be optimize. In particular, besides to the type and volume of anti-solvent used, the time at which it is added is a crucial factor that determinate the perovskite formation. Since the solvent evaporation during the spin coating of the precursor solution occurs within few seconds, it is necessary to establish with accuracy the instant in which carrying out the dripping. In the first seconds after the start of the spin coating process, the excess of solution is gradually removed by centrifugal force. In this conditions the perovskite solution is far away from supersaturation conditions, therefore the anti-solvent addition is inappropriate. In the subsequent seconds, after the solution excess removal, the residue solvent evaporates concentrating the perovskite solution and producing a dense a uniform film. To be effective the anti-solvent dripping must be achieved in this step, before the solvent evaporation is complete and the perovskite crystallization occurs spontaneously. The anti-solvent addition produces an instantaneous crystallization of the perovskite observable by the sudden darkening of the film. This is finally subject to thermal annealing in order to remove residues solvent traces. The process described can be applied with precursor solutions in DMF or DMSO. The difference between the two cases is that the in presence of DMSO the anti-solvent dripping leads to a smooth, pre-crystallized transparent film and not directly to the perovskite film because PbI_2 -DMSO adduct retard the crystallization that occurs in a subsequent thermal annealing treatment^[134].

2.8.3 Two-Step Solution methods

In two-step methods the perovskite is obtained through a heterogeneous phase reaction between solid metal halide precursor and organohalide solution. The method introduced by Gratzel et al. consists of PbI_2 deposition onto a mesoporous TiO_2 scaffold and subsequent immersion into a MAI solution, that penetrating through the channels of the scaffold reacts with PbI_2 and produces the perovskite^[135]. The complete conversion of PbI_2 in perovskite occurs in few seconds because the mesoporous structure promotes MAI diffusion into the PbI_2 lattice. Moreover, this structure provides enough space for volume expansion of PbI_2 precursor resulting from MAI intercalation. The method described is not directly applicable to prepare perovskite film for planar solar cells. Indeed, in such case the PbI_2 forms a compact film and when it is dipped in the MAI solution, only the PbI_2 on the surface come into contact and can react with MAI. As a consequence, a complete conversion can not be obtained unless the reaction time is extent to some hours^[136]. This time is required because the compact PbI_2 film limits the diffusion and intercalation of MAI. On the other hand, the volume expansion induced by the MAI intercalation further hinders the MAI diffusion in PbI_2 . Generally, the unreacted PbI_2 determines a lowering of solar cell performance due to the reduction of light absorption and charge transport properties^[137,138]. Moreover, the prolonged reaction time causes a degradation of the perovskite with significant effects in terms of efficiency and reproducibility of the devices.

An evolution of the described method allows to obtain high quality films of perovskite. Briefly, MAI solution is spin-coated on the top of a PbI_2 film to form stacked layer and by thermal annealing the diffusion and reaction of MAI in PbI_2 is promoted^[139]. In this way, by controlling accurately the thickness of the films a complete conversion can be obtained.

2.9 Perovskite solar cell architectures

Mesoscopic and planar are the two main architectures in which perovskite solar cells can be fabricated. In mesoscopic structure a compact thin layer of TiO_2 with the function of electron transport layer (ETL) is deposited on a transparent conductive oxide (TCO), generally constitutes of Fluorine doped Tin Oxide (FTO). Subsequently, a film of metal oxide nanoparticles is deposited and subject to high temperature in order to promote the sintering of the nanoparticles^[140]. In this way, a film with mesoscopic pores that result from the void spaces between the nanoparticles is obtained. Afterwards, the mesoporous film is infiltrated

with perovskite precursors solution and, after the crystallization of the active layer, a hole transport layer and the metallic electrode are deposited to complete the device. In figure 2.23 a schematic diagram of the mesoscopic architecture is reported.

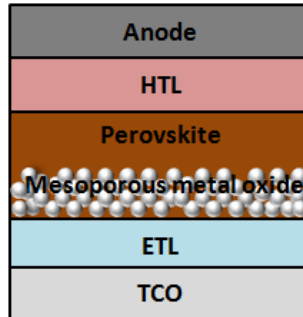


Figure 2.23 Schematic diagram of mesoscopic structure.

The thickness of the mesoporous layer is a key parameter to be optimized for obtaining high efficient devices. Indeed, a too thin layer limits the amount of deposited perovskite and therefore the absorption of light, while a thicker layer has the disadvantage of a possible incomplete filling of the pores. In this case, the use of appropriate deposition techniques permits to overcome this limit. The mesoporous architecture allows to obtain high performance devices with an efficiency of up to 20.1%^[141].

In the early perovskite devices, the mesoscopic layer was constituted by semiconducting TiO_2 that collected the electrons photogenerated in the perovskite and allowed their transport to the cathode. Later, it was demonstrated that by using an insulating scaffold of alumina (Al_2O_3) instead of the mesoporous TiO_2 electron-conducting network, cells with efficiency of 10.9% could be obtained. Since the alumina scaffold acts only as structural component in the cell, it was possible to conclude that perovskite itself is able to efficiently transport electrons^[142]. These results have led to the development of a planar architecture in which the mesoporous layer is absent. In this way, it was possible to avoid the high temperature processes required for the sintering of the mesoporous layer and to reduce the structural complexity of the device.

In planar structure the perovskite film is comprised between flat HTL and ETL. The challenge to obtain high efficient devices is to deposit a smooth layer of perovskite with a uniform surface coverage. This is necessary to avoid current leakage due to the direct contact between the HTL and ETL^[130].

Another important aspect to consider is that the size of the grains must be large enough to

reduce the charge recombination at grain boundaries.

Planar architecture can be distinct in regular (or n-i-p) and inverted (or p-i-n) configurations^[143] as reported in figure 2.24.

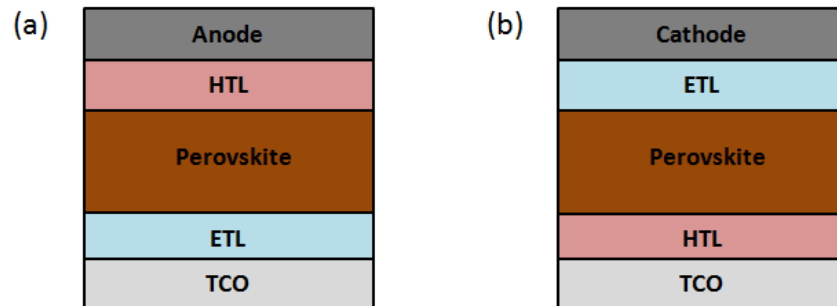


Figure 2.24 Schematic diagram of regular planar structure (a) and inverted planar structure (b).

The difference between the two configurations is due to the order in which the charge transport layers are located with respect to the semitransparent electrode^[143].

In regular planar structure the ETL (n-type), generally consisting of a compact TiO_2 , is deposited on the transparent electrode, while the HTL (p-type), usually constituted by 2,2',7,7'-Tetrakis-(N,N-di-4-methoxyphenylamino)-9,9'-spirobifluorene (spiro-MeOTAD), is deposited on the perovskite. In inverted configuration the layer at contact with the transparent conducting substrate is the HTL. PEDOT:PSS is one of the most used HTL while PC_{61}BM or PC_{71}BM are the conventional ETLs.

Among the different architectures, in this thesis work an inverted planar structure was adopted as reference structure to investigate the effects produced by the integration of anisotropic gold nanoparticles. In particular, perovskite solar cells with the following structures were chosen: glass/ITO/PEDOT:PSS/Perovskite/ PC_{61}BM /BCP/Al and glass/ITO/poly-TPD/Perovskite/ PC_{61}BM /BCP/Al (figure 2.25) where BCP is bathocuproine, used as hole blocking layer, while poly-TPD is Poly[N,N'-bis(4-butylphenyl)-N,N'-bisphenylbenzidine] that acts as HTL.

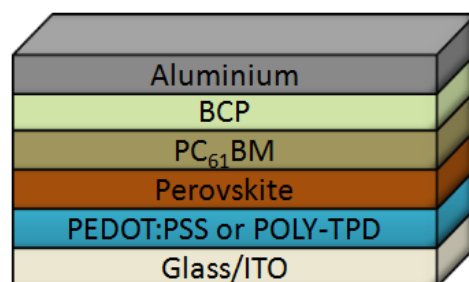


Figure 2.25 Schematic diagram of the inverted perovskite solar cells used as reference in this thesis work.

2.10 Hysteresis

Hysteresis is a phenomenon widely observed in perovskite solar devices. It consists in the variation of the J-V curves under different scan rate or scan direction and it is related to the material properties and physical processes that occur during the working of the device^[130]. In figure 2.26 is reported a typical hysteresis behavior observed in the characteristic curves of perovskite solar cells acquired under different scan direction.

Hysteresis makes it difficult to obtain reliable electrical solar cell characterization; moreover, it reduces the long-term device operational stability^[144], so it is opportune to identify its causes in order to limit this undesired effect.

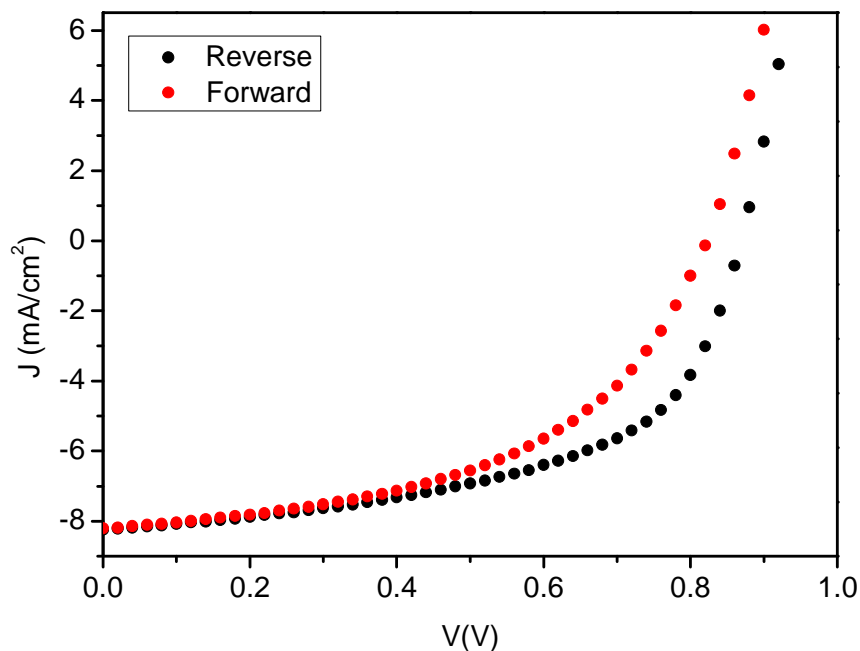


Figure 2.26 Current–voltage curves with forward and reverse scans for a planar solar cell showing hysteresis.

Ion migration in perovskite film is considered one of the main causes of hysteresis^[145,146]. When an electric field is applied to the device, ions in the perovskite drift and accumulate at the interfaces according to the intensity and direction of the field. Since this migration occurs with a proper kinetics, different scan rates lead to different charge distribution at interfaces. As an effect of this charge accumulation, an internal electric field is generated which can have the same or opposite direction of the external electric field applied. The effective electric field is the resulting of the two contributions and this explains the difference in the electrical response in terms of photocurrent or photovoltage^[130] observed.

Inefficient electron extraction may be another cause of the hysteresis. Indeed, charge accumulation at the interfaces induces capacitive effects in the device with the consequent hysteresis enhancement^[147,148].

Hysteresis is widely observed in regular planar perovskite device, while it is not an important phenomenon in inverted architecture. In particular, in this kind of devices the use of PC₆₁BM as electron transport layer is determinant in suppress the hysteresis^[149]. PC₆₁BM passivates the trap states and bind the mobile ions to form radicals, thus limiting their migration^[150]. Moreover, PC₆₁BM improves the electron extraction from the perovskite. When PC₆₁BM is deposited on perovskite, it diffuses into the defects and in the grain boundaries. In this way the interfacial area is considerably increased, as in the case of mesoporous architectures in which the hysteresis is limited. Consequently, the electron extraction is notable enhanced, charges accumulation is prevented and the hysteresis effect is suppressed.

2.11 Plasmonic light trapping enhancement in perovskite solar cells

Among the different solar cell technologies, perovskite solar modules have the shortest energy-payback time^[151]. The raw materials required for their production are all Earth-abundant. On the other hand, it was demonstrated that it is possible to fabricate perovskite solar cells using lead waste recycled from lead-acid batteries^[152].

Although the stability of these devices is still limited, the greater obstacle to their commercialization is related to the use of lead that is a toxic element. Lead produces serious damage to human body at the renal, reproductive and nervous systems also at low concentrations^[153].

Solar panels are normally located in open fields or on roofs of building. Despite being encapsulated, the possibility of being damaged must be considered. In this case the organohalide lead perovskite in contact with rain undergoes degradation. The PbI₂ produced is partially soluble in water so it can be leach by rain into the soil and from there into groundwater in significant quantities^[154].

It is clear, therefore, that the reduction or replacement of lead for the fabrication of high efficient perovskite devices is a key aspect for their marketing. Tin has been identified as a possible lead alternative for the fabrication of perovskite solar cells. Although tin halide perovskites have shown good semiconducting behavior, the Sn²⁺ required in perovskite structure rapidly oxidizes in ambient condition to the more stable Sn⁴⁺. This leads to the lack

of charge neutrality of the perovskite structure resulting in its breakdown^[107]. Moreover, the devices obtained using lead-free perovskite are less efficient than cells made with organohalide lead perovskite. In the context of lead reduction, the use of plasmonic nanoparticles can be an effective way to reduce the thickness of the perovskite film and therefore the lead content in the devices, while preserving their high performance^[155].

The improvement of the efficiency of organic solar cells through the integration of plasmonic nanoparticles has led to the extension of their use in perovskite solar cells obtaining successful results. Light scattering and near-field enhancement have been identified as the predominant effects that lead to an improvement of the efficiency in plasmonic perovskite solar cells. However, two other important mechanisms have been involved to justify the enhancement of efficiency in this kind of devices: hot electron transfer (HET) and plasmon resonant energy transfer (PRET)^[156]. While the effects of light scattering and near-field enhancement are originated from the radiative decay of the plasmon, HET and PRET result from the nonradiative plasmon dephasing.

In HET, electrons with energies higher than the Fermi level (“hot electrons”)^[157], originated from the Landau damping of the plasmons, are transferred to a semiconductor in direct contact with the metallic nanostructure. Landau damping is a quantum mechanical phenomenon which occurs on a timescale of 1–100 fs and leads to the formation of electron-hole pairs in the metals as a consequence of the energetic relaxation of the plasmon. An isolate system evolves through an electron–electron scattering process that leads from a non-Fermi to a Fermi electron distribution, followed by the cooling of hot electrons via electron–phonon scattering and heat dissipation from the nanostructure to the environment through phonon–phonon scattering^[158]. However, if a semiconductor with a high density of states in its conduction band (such as TiO₂) is in contact with the plasmon, hot electrons with enough energy to overcome the Schottky barrier can be injected into the conduction band of the semiconductor before dissipating their energy as heat. This leads to the generation of additional photocurrent in the device with a consequent increase of its efficiency.

HET allows to exploit also the light with energy lower than band gap of the semiconductors because the energy required to occur is lower. Therefore, no spectral overlap between the metal nanostructure and semiconductor is required. However, there are two necessary conditions for the HET to take place:

- metal and the semiconductor have to be very close at not more than 2 nm one from the other;
- the Fermi levels of metal and semiconductor have to be aligned.

Shape, size and composition of the metal nanostructures are essential parameters for controlling the efficiency of the HET process. Nanoparticles with size comprised between 5-20 nm present strong surface dispersion that promotes hot electron transfer from the metal to the semiconductors. The increase in size of nanoparticles leads to a reduction of the hot electron generation as a consequence of the radiative effects that become competitive. The composition of the nanoparticles is also important because metals with a strong intraband and interband transition have weak radiative properties and efficiently convert photons in hot carriers.

Besides HET, plasmon resonant energy transfer is another important non-radiative mechanism that leads to the enhancement of the performance of solar devices. PRET consists in the energy transfer from the plasmon to an adjacent semiconductor via dipole–dipole coupling with the generation of electron–hole pairs below and near the semiconductor band edge. PRET occurs only if the semiconductor is affected by the near-field of the nanoparticles and a spectral overlap exists between the plasmon resonance spectrum of the nanoparticles and the absorption band of the semiconductor. Since in these conditions the effect of radiative near-field enhancement that lead to an increase of the absorption cross-section of the materials can coexist, it is difficult to discriminate the two contributions in improving the performance of solar cells.

Unlike HET, PRET does not require direct contact or alignment of the bands between the metal and the semiconductor. PRET in plasmonic solar cells competes with the opposite process known as Forster Resonance Energy Transfer (FRET) through which the energy is transferred from the semiconductor to the plasmon. However, PRET is the predominant mechanism if the plasmon has a dephasing time slower than that of the semiconductor. Moreover, PRET is favored when the semiconductor is at the minimum distance from the plasmon but not in direct physical contact^[156].

2.11.1 Effects of plasmonic nanoparticles incorporation in perovskite solar cells

Although perovskite solar cells technology is one of the most promising in the field of photovoltaics, some limitations hinder the commercialization of these devices such as the

low stability at high levels of moisture and temperature, the presence of toxic lead in perovskite structure and the hysteresis effects. The integration of plasmonic nanostructures in perovskite solar cells could be an effective approach to limit or eliminate some of these disadvantages. The use of plasmonic nanoparticles could allow to reduce the thickness of the perovskite layer and in turns the amount of lead present in the device without lowering its efficiency. The plasmonic effects of light scattering and near-field enhancement can give a more appreciable contribute to the improvement of light absorption in the case of very thin perovskite films considering the high absorption coefficient of these materials. In addition to this optical contribution, the incorporation of metallic nanoparticles can improve the electrical properties of the cells, increasing the conductivity of the buffer layers and in turns the charge transport rate to the electrodes. The incorporation of nanoparticles can also lead to a reduction of the hysteresis effect by the hot electron transfer mechanism. It has been reported that gold nanoparticles embedding in TiO_x layer promote the filling of the trape states into TiO_x through the plasmon-induced electron injection. This leads to an increase of the charge carrier density in TiO_x resulting in an enhancement of charge mobility that dramatically reduces space limited charges and so the hysteresis^[159].

Numerous works^[160] in which a variety of nanoparticles of different materials, sizes and shapes have been incorporated in mesoscopic and planar perovskite solar cells are reported in literature. However, in the following the attention will be focused only on those related to the incorporation of plasmonic nanoparticles in inverted planar perovskite solar cells, since this architecture was adopted as reference in this thesis work.

Hsu et al.^[161] have proposed the integration of triangular Ag nanoplates in the HTL of planar inverted perovskite solar cells with the structure glass/ITO/PEDOT:PSS/ $\text{CH}_3\text{NH}_3\text{PbI}_{3-x}\text{Cl}_x$ /PC₆₁BM/Al. The nanoplates had an edge length in the range of 40-100 nm and a thickness of about 12 nm and when incorporated in the PEDOT:PSS did not produce morphology disturb because they tended to deposit flatly with respect to the layer. The devices with the Ag nanoplates showed an increase of efficiency of 9.5 % respect to the reference essentially due to a higher J_{SC} value. This enhancement was justified as an increase of light absorption by the active layer resulting from the plasmonic scattering effect of the nanoplates.

Kakavelakis et al.^[162] have studied the effects of the incorporation of Au, Ag and Al nanospheres, produced by laser ablation, in the HTL of inverted perovskite cells with the structure glass/ITO/PEDOT:PSS/ $\text{CH}_3\text{NH}_3\text{PbI}_{3-x}\text{Cl}_x$ /PCBM/PFN/Ag. The nanoparticles of Au, Ag

and Al had an average diameter of 10, 20 and 30 nm, respectively. The integration of Au and Ag nanoparticles has led to an enhancement of the J_{SC} , due to an improved hole extraction rate, and of the FF as effect of a lower device series resistance. In the case of Al nanospheres the J_{SC} enhancement effect was limited because an ultra-thin oxide layer on their surface was formed during their preparation. In the best case, using Ag nanospheres an efficiency enhancement of the about 13% was obtained respect to the reference device. It was observed that the Al nanospheres led to an increase of the device stability, since they lowered the degradation rate of perovskite in environmental conditions. This effect was related to the oxidation of Al nanoparticles that reduces the amount of water molecules deriving from the moisture on the air that reach the perovskite.

Liu et al.^[163] accomplished the simultaneous integration of Au and Ag nanospheres with a diameter of about 50 nm in the HTL of an of inverted perovskite cell with the structure ITO/PEDOT:PSS/ $CH_3NH_3PbI_3$ /PCBM/Al.

The use of Au and Ag nanoparticles was related to the possibility of exploiting both their relative LSPRs that occur in different visible spectral range. An efficiency enhancement of about 12% was observed in plasmonic devices due to optical and electrical effects induced by the presence of the nanoparticles. In particular, the effect of the near-field enhancement led to an increase of the amount of light absorbed by the perovskite and to the improvement of the charge transports properties of the HTL.

Wu et al.^[164] have fabricated inverted planar perovskite solar cells with the structure ITO/PEDOT:PSS/ $CH_3NH_3PbI_3$ /PCBM/Al integrating silica-coated gold (Au@SiO₂) nanorods at the interface between the PEDOT:PSS and the perovskite. Au@SiO₂ nanorods had an average diameter, length and thickness of SiO₂ of 16.8 nm, 34.7 nm and 9.5 nm, respectively. Nanorods were used to exploit their longitudinal and transversal plasmonic bands in order to increase the absorption of light as effect of the near field-enhancement on perovskite, while the insulating coating of silica was necessary to prevent exciton quenching and recombination losses that occur at the metal/perovskite interface. By optimizing the concentration of the nanorods the authors have demonstrated an efficiency enhancement of 40% respect to the reference device due to an increase of J_{SC} and FF, resulting from an improvement of light absorption and a reduction of device series resistance, respectively.

2.12 References

- [1] M. E. Becquerel, Mémoire sur les effets électriques produits sous l'influence des rayons solaires. *Comptes rendus hebdomadaires des séances de l'Académie des sciences*, **1839**, 9, 561-567.
- [2] D. M. Chapin et al., A new silicon p-n junction photocell for converting solar radiation into electrical power. *Journal of Applied Physics*, **1954**, 25, 676-677.
- [3] B. Kippelen et al., Organic photovoltaics. *Energy & Environmental Science*, **2009**, 2, 251–261
- [4] M. A. Green et al., Solar cell efficiency tables. *Progress in Photovoltaics: Research and Applications*, **2016**, 7, 905-913.
- [5] M. Boccard et al., Multiscale transparent electrode architecture for efficient light management and carrier collection in solar cells. *Nano Letters*, **2012**, 12, 1344-1348.
- [6] K. Yamamoto et al., A high efficiency thin film silicon solar cell and module. *Solar Energy*, **2004**, 77, 939-949.
- [7] D. L. Staebler et al., Reversible conductivity changes in discharge-produced amorphous Si. *Applied Physics Letters*, **1977**, 31, 292-294.
- [8] A. Mutalikdesai et al., Emerging solar technologies: Perovskite solar cell. *Resonance*, **2017**, 22, 1061-1083.
- [9] M. C. Scharber et al., Efficiency of bulk-heterojunction organic solar cells. *Progress in Polymer Science*, **2013**, 38, 1929-1940.
- [10] N. Sebastian, Limiting Approach to Generalized Gamma Bessel Model via Fractional Calculus and Its Applications in Various Disciplines. *Axioms*, **2015**, 4, 385-399.
- [11] S. S. Hegedus et al., Thin-film solar cells: device measurements and analysis. *Progress in Photovoltaics: Research and Applications*, **2004**, 12, 155-176.
- [12] A. Melianas, Non-Equilibrium Charge Motion in Organic Solar Cells. *Linköping University Electronic Press*, **2017**, Vol. 1836.
- [13] J. Nelson, Imperial College Press. *The Physics of Solar Cells*, **2003**.
- [14] Z. Lin et al., Low-cost nanomaterials: toward greener and more efficient energy applications. *Springer*, **2014**.
- [15] Z. Cui, Printed electronics: materials, technologies and applications. *John Wiley & Sons*, **2016**.
- [16] S. Forget et al., Organic solid-state lasers. Vol. 175. *New York: Springer*, **2013**.
- [17] D. Hertel et al., Photoconduction in amorphous organic solids. *ChemPhysChem*, **2008**, 9, 666-688.
- [18] G. A. Chamberlain, Organic solar cells: A review. *Solar cells*, **1983**, 8, 47-83.
- [19] J. C. Bernede, Organic photovoltaic cells: history, principle and techniques. *Journal of the Chilean Chemical Society*, **2008**, 53, 1549-1564.

- [20] C. W. Tang, Two-layer organic photovoltaic cell. *Applied Physics Letters*, **1986**, 48, 183-185.
- [21] N. S. Sariciftci et al., Semiconducting polymer-buckminsterfullerene heterojunctions: Diodes, photodiodes, and photovoltaic cells. *Applied Physics Letters*, **1993**, 62, 585-587.
- [22] J. J. Halls et al., The photovoltaic effect in a poly(p-phenylenevinylene)/perylene heterojunction. *Synthetic Metals*, **1997**, 85, 1307-1308.
- [23] J. J. Halls et al., Exciton diffusion and dissociation in a poly (p-phenylenevinylene)/C60 heterojunction photovoltaic cell. *Applied Physics Letters*, **1996**, 68, 3120-3122.
- [24] T. H. Lee et al., A universal processing additive for high-performance polymer solar cells. *RSC Advances*, **2017**, 7, 7476-7482.
- [25] T. Erb et al., Correlation between structural and optical properties of composite polymer/fullerene films for organic solar cells. *Advanced Functional Materials*, **2005**, 15, 1193-1196.
- [26] G. Li et al., Investigation of annealing effects and film thickness dependence of polymer solar cells based on poly (3-hexylthiophene). *Journal of Applied Physics*, **2005**, 98, 043704.
- [27] S. Hüttner et al., Controlled solvent vapour annealing for polymer electronics. *Soft Matter*, **2009**, 5, 4206-4211.
- [28] D. T. Scholes et al., The Effects of Crystallinity on Charge Transport and the Structure of Sequentially Processed F4TCNQ-Doped Conjugated Polymer Films. *Advanced Functional Materials*, **2017**, 27, 1702654.
- [29] G. Chidichimo et al., Organic solar cells: problems and perspectives. *International Journal of Photoenergy*, **2010**.
- [30] I. Litzov et al., Development of efficient and stable inverted bulk heterojunction (BHJ) solar cells using different metal oxide interfaces. *Materials*, **2013**, 6, 5796-5820.
- [31] W. Brütting, Physics of organic semiconductors. *John Wiley & Sons*, **2006**.
- [32] K. M. Coakley et al., Conjugated polymer photovoltaic cells. *Chemistry of Materials*, **2004**, 16, 4533-4542.
- [33] Y. Terao et al., Correlation of hole mobility, exciton diffusion length, and solar cell characteristics in phthalocyanine/fullerene organic solar cells. *Applied Physics Letters*, **2007**, 90, 103515.
- [34] H. Marciniak et al., One-dimensional exciton diffusion in perylene bisimide aggregates. *The Journal of Physical Chemistry A*, **2010**, 115, 648-654.
- [35] J. Singh, et al., Dissociation of charge transfer excitons at the donor-acceptor interface in bulk heterojunction organic solar cells. *Journal of Materials Science: Materials in Electronics*, **2017**, 28, 7095-7099.
- [36] I. Fishchuk et al., Unified description for hopping transport in organic semiconductors including both energetic disorder and polaronic contributions. *Physical Review B*, **2013**, 88, 125202.

- [37] L. J. A. Koster et al., Origin of the light intensity dependence of the short-circuit current of polymer/fullerene solar cells. *Applied Physics Letters*, **2005**, 87, 203502.
- [38] B. Ecker et al., Understanding S-shaped current–voltage characteristics in organic solar cells containing a TiO_x interlayer with impedance spectroscopy and equivalent circuit analysis. *The Journal of Physical Chemistry C*, **2012**, 116, 16333-16337.
- [39] A. Kokil et al., Techniques for characterization of charge carrier mobility in organic semiconductors. *Journal of Polymer Science Part B: Polymer Physics*, **2012**, 50, 1130-1144.
- [40] M. Thirumoorthi et al., Structure, optical and electrical properties of indium tin oxide ultra thin films prepared by jet nebulizer spray pyrolysis technique. *Journal of Asian Ceramic Societies*, **2016**, 4, 124-132.
- [41] R. Steim, et al., Interface materials for organic solar cells. *Journal of Materials Chemistry*, **2010**, 20, 2499-2512.
- [42] E. L. Ratcliff et al., Investigating the influence of interfacial contact properties on open circuit voltages in organic photovoltaic performance: work function versus selectivity. *Advanced Energy Materials*, **2013**, 3, 647-656.
- [43] K. Heet al., Work function changes of plasma treated indium tin oxide. *Organic Electronics*, **2014**, 15, 1731-1737.
- [44] F. Nüesch et al., Importance of indium tin oxide surface acido basicity for charge injection into organic materials based light emitting diodes. *Journal of Applied Physics*, **2000**, 87, 7973-7980.
- [45] F. Cheng et al., Enhancing the performance of P3HT: ICBA based polymer solar cells using LiF as electron collecting buffer layer and UV–ozone treated MoO₃ as hole collecting buffer layer. *Solar Energy Materials and Solar Cells*, **2013**, 110, 63-68.
- [46] S. Das et al., Self-assembled monolayer modified ITO in P3HT: PC61BM organic solar cells with improved efficiency. *Solar Energy Materials and Solar Cells*, **2014**, 124, 98-102.
- [47] B. Li et al., Interfacial engineering by using self-assembled monolayer in mesoporous perovskite solar cell. *RSC Advances*, **2015**, 5, 94290-94295.
- [48] G. Williams et al., The photo-stability of polymer solar cells: Contact photo-degradation and the benefits of interfacial layers. *Advanced Functional Materials*, **2013**, 23, 2239-2247.
- [49] J. R. Tumbleston et al., Electrophotonic enhancement of bulk heterojunction organic solar cells through photonic crystal photoactive layer. *Applied Physics Letters*, **2009**, 94, 25.
- [50] J. R. Tumbleston et al., Absorption and quasiguided mode analysis of organic solar cells with photonic crystal photoactive layers. *Optics express*, **2009**, 17, 7670-7681.
- [51] D. H. Ko et al., Photonic crystal geometry for organic solar cells. *Nano Letters*, **2009**, 9, 2742-2746.

- [52] L. Chen et al., Light harvesting improvement of organic solar cells with self-enhanced active layer designs. *Optics Express*, **2012**, 20, 8175-8185.
- [53] K. Tvingstedt et al., Trapping light with micro lenses in thin film organic photovoltaic cells. *Optics Express*, **2008**, 16, 21608-21615.
- [54] J. Gjessinget et al., 2D back-side diffraction grating for improved light trapping in thin silicon solar cells. *Optics express*, **2010**, 18, 5481-5495.
- [55] A. P. Kulkarni et al., Plasmon-enhanced charge carrier generation in organic photovoltaic films using silver nanoprisms. *Nano Letters*, **2010**, 10, 1501-1505.
- [56] I. Diukman et al., Controlling absorption enhancement in organic photovoltaic cells by patterning Au nano disks within the active layer. *Optics Express*, **2011**, 19, A64-A71.
- [57] H. A. Atwater et al., Plasmonics for improved photovoltaic devices. *Nature Materials*, **2010**, 9, 205.
- [58] K. R. Catchpole et al., Design principles for particle plasmon enhanced solar cells. *Applied Physics Letters*, **2008**, 93, 191113.
- [59] J. Reguera et al., Anisotropic metal nanoparticles for surface enhanced Raman scattering. *Chemical Society Reviews*, **2017**, 46, 3866-3885.
- [60] C.-H. Chou et al., Plasmonic nanostructures for light trapping in organic photovoltaic devices. *Nanoscale*, **2014**, 6, 8444-8458.
- [61] L. Lu et al., Cooperative plasmonic effect of Ag and Au nanoparticles on enhancing performance of polymer solar cells. *Nano Letters*, **2012**, 13, 59-64.
- [62] J.-L. Wu et al., Surface plasmonic effects of metallic nanoparticles on the performance of polymer bulk heterojunction solar cells. *ACS Nano*, **2011**, 5, 959-967.
- [63] J. H. Lee et al., High efficiency polymer solar cells with wet deposited plasmonic gold nanodots. *Organic Electronics*, **2009**, 10, 416-420.
- [64] A. Williamson et al., The design of efficient surface-plasmon-enhanced ultra-thin polymer-based solar cells. *Applied Physics Letters*, **2011**, 99, 186.
- [65] C. Wang et al., Optical and electrical effects of gold nanoparticles in the active layer of polymer solar cells. *Journal of Materials Chemistry*, **2012**, 22, 1206-1211.
- [66] R. S. Kim et al., E-beam deposited Ag-nanoparticles plasmonic organic solar cell and its absorption enhancement analysis using FDTD-based cylindrical nano-particle optical model. *Optics Express*, **2012**, 20, 12649-12657.
- [67] B. Paciet al., Enhanced structural stability and performance durability of bulk heterojunction photovoltaic devices incorporating metallic nanoparticles. *Advanced Functional Materials*, **2011**, 21, 3573-3582.
- [68] M. Xue et al., Charge-carrier dynamics in hybrid plasmonic organic solar cells with Ag nanoparticles. *Applied Physics Letters*, **2011**, 98, 119.
- [69] T. Z. Oo et al., Ultrafine gold nanowire networks as plasmonic antennae in organic photovoltaics. *The Journal of Physical Chemistry C*, **2012**, 116, 6453-6458.

- [70] E. Stratakis et al., Nanoparticle-based plasmonic organic photovoltaic devices. *Materials Today*, **2013**, 16, 133-146.
- [71] K. Topp et al., Impact of the incorporation of Au nanoparticles into polymer/fullerene solar cells. *The Journal of Physical Chemistry A*, **2009**, 114, 3981-3989.
- [72] E. Kymakis et al., Plasmonic bulk heterojunction solar cells: the role of nanoparticle ligand coating. *ACS Photonics*, **2015**, 2, 714-723.
- [73] M. D. Brown et al., Plasmonic dye-sensitized solar cells using core-shell metal-insulator nanoparticles. *Nano Letters*, **2010**, 11, 438-445.
- [74] G. D. Spyropoulos et al., Organic bulk heterojunction photovoltaic devices with surfactant-free Au nanoparticles embedded in the active layer. *Applied Physics Letters*, **2012**, 100, 213904.
- [75] F. C. Chen et al., Plasmonic-enhanced polymer photovoltaic devices incorporating solution-processable metal nanoparticles. *Applied Physics Letters*, **2009**, 95, 182.
- [76] D. DS Fung et al., Optical and electrical properties of efficiency enhanced polymer solar cells with Au nanoparticles in a PEDOT-PSS layer. *Journal of Materials Chemistry*, **2011**, 21, 16349-16356.
- [77] Y.-S. Hsiao et al., Improving the light trapping efficiency of plasmonic polymer solar cells through photon management. *The Journal of Physical Chemistry C*, **2012**, 116, 20731-20737.
- [78] D. Kozanoglu et al., Power conversion efficiency enhancement of organic solar cells by addition of gold nanostars, nanorods, and nanospheres. *Organic Electronics*, **2013**, 14, 1720-1727.
- [79] H. L. Gao et al., Plasmon enhanced polymer solar cells by spin-coating Au nanoparticles on indium-tin-oxide substrate. *Applied Physics Letters*, **2012**, 101, 133903.
- [80] S. Shahin et al., Ultrathin organic bulk heterojunction solar cells: Plasmon enhanced performance using Au nanoparticles. *Applied Physics Letters*, **2012**, 101, 053109.
- [81] Q.-Q. Yan et al., Plasmon-enhanced polymer bulk heterojunction solar cells with solution-processable Ag nanoparticles. *Optoelectronics Letters*, **2011**, 7, 410-414.
- [82] E. Stratakis et al., Plasmonic organic photovoltaic devices with graphene based buffer layers for stability and efficiency enhancement. *Nanoscale*, **2013**, 5, 4144-4150.
- [83] W. Li et al., Chemically diverse and multifunctional hybrid organic-inorganic perovskites. *Nature Reviews Materials*, **2017**, 2, 16099.
- [84] T. C. Sum et al., Advancements in perovskite solar cells: photophysics behind the photovoltaics. *Energy & Environmental Science*, **2014**, 7, 2518-2534.
- [85] K. Momma and F. Izumi, VESTA 3 for three-dimensional visualization of crystal, volumetric and morphology data. *Journal of Applied Crystallography*, **2011**, 44, 1272-1276.

- [86] Z. Li et al., Stabilizing perovskite structures by tuning tolerance factor: formation of formamidinium and cesium lead iodide solid-state alloys. *Chemistry of Materials*, **2015**, 28, 284-292.
- [87] G. Kieslich et al., Solid-state principles applied to organic–inorganic perovskites: new tricks for an old dog. *Chemical Science*, **2014**, 5, 4712-4715.
- [88] C. C. Stoumpos et al., The renaissance of halide perovskites and their evolution as emerging semiconductors. *Accounts of chemical research*, **2015**, 48, 2791-2802.
- [89] L. Liang et al., On the criteria of formation and lattice distortion of perovskite-type complex halides. *Journal of Physics and Chemistry of Solids*, **2004**, 65, 855-860.
- [90] C. Li et al., Formability of ABX_3 (X= F, Cl, Br, I) Halide Perovskites. *Acta Crystallographica Section B: Structural Science*, **2008**, 64, 702-707.
- [91] M. Habibi et al., Progress in emerging solution-processed thin film solar cells – Part II: Perovskite solar cells. *Renewable and Sustainable Energy Reviews*, **2016**, 62, 1012-1031.
- [92] J. Huang et al., Understanding the physical properties of hybrid perovskites for photovoltaic applications. *Nature Reviews Materials*, **2017**, 2, 17042.
- [93] W.-J. Yin et al., Unique properties of halide perovskites as possible origins of the superior solar cell performance. *Advanced Materials*, **2014**, 26, 4653-4658.
- [94] B. Walker et al., Small molecule solution-processed bulk heterojunction solar cells. *Chemistry of Materials*, **2010**, 23, 470-482.
- [95] S. H. Park et al., Bulk heterojunction solar cells with internal quantum efficiency approaching 100%. *Nature Photonics*, **2009**, 3, 297.
- [96] Y. Kim et al., A strong regioregularity effect in self-organizing conjugated polymer films and high-efficiency polythiophene: fullerene solar cells. *Materials for Sustainable Energy: A Collection of Peer-Reviewed Research and Review Articles from Nature Publishing Group*, **2011**, 63-69.
- [97] T. J. Jacobsson et al., Exploration of the compositional space for mixed lead halogen perovskites for high efficiency solar cells. *Energy & Environmental Science*, **2016**, 9, 1706-1724.
- [98] S. Sarkar et al., Role of the A-site cation in determining the properties of the hybrid perovskite $CH_3NH_3PbBr_3$. *Physical Review B*, **2017**, 95, 214118.
- [99] G. Giorgi et al., Cation role in structural and electronic properties of 3D organic–inorganic halide perovskites: a DFT analysis. *The Journal of Physical Chemistry C*, **2014**, 118, 12176-12183.
- [100] L. A. Frolova et al., Exploring the Effects of the Pb^{2+} Substitution in $MAPbI_3$ on the Photovoltaic Performance of the Hybrid Perovskite Solar Cells. *The Journal of Physical Chemistry Letters*, **2016**, 7, 4353–4357.
- [101] I. Chung et al., $CsSnI_3$: semiconductor or metal? High electrical conductivity and strong near-infrared photoluminescence from a single material. High hole mobility

- and phase-transitions. *Journal of the American Chemical Society*, **2012**, 134, 8579-8587.
- [102] B. Lee et al., All-solid-state dye-sensitized solar cells with high efficiency. *Nature*, **2012**, 485, 486.
- [103] F. Hao et al., Anomalous band gap behavior in mixed Sn and Pb perovskites enables broadening of absorption spectrum in solar cells. *Journal of the American Chemical Society*, **2014**, 136, 8094-8099.
- [104] C. C. Stoumpos et al., Semiconducting tin and lead iodide perovskites with organic cations: phase transitions, high mobilities, and near-infrared photoluminescent properties. *Inorganic chemistry*, **2013**, 52, 9019-9038.
- [105] Y. Ogomi et al., $\text{CH}_3\text{NH}_3\text{Sn}_x\text{Pb}_{(1-x)}\text{I}_3$ Perovskite solar cells covering up to 1060 nm. *The Journal of Physical Chemistry Letters*, **2014**, 5, 1004-1011.
- [106] E. Mosconi et al., Electronic and optical properties of mixed Sn–Pb Organohalide perovskites: a first principles investigation. *Journal of Materials Chemistry A*, **2015**, 3, 9208-9215.
- [107] N. K. Noel et al., Lead-free organic–inorganic tin halide perovskites for photovoltaic applications. *Energy & Environmental Science*, **2014**, 7, 3061-3068.
- [108] F. Hao et al., Lead-free solid-state organic–inorganic halide perovskite solar cells. *Nature Photonics*, **2014**, 8, 489-494.
- [109] C. M. Sutter-Fella et al., High photoluminescence quantum yield in band gap tunable bromide containing mixed halide perovskites. *Nano Letters*, **2015**, 16, 800-806.
- [110] D. P. Nenon et al., Structural and chemical evolution of methylammonium lead halide perovskites during thermal processing from solution. *Energy & Environmental Science*, **2016**, 9, 2072-2082.
- [111] D. Banerjee et al., Hybrid Inorganic Organic Perovskites: A Low-Cost-Efficient Optoelectronic Material. In *Perovskite Photovoltaics*, **2018**, 123-162.
- [112] J. M. Frost et al., Atomistic origins of high-performance in hybrid halide perovskite solar cells. *Nano Letters*, **2014**, 14, 2584-2590.
- [113] A. Miyata et al., Direct measurement of the exciton binding energy and effective masses for charge carriers in organic-inorganic tri-halide perovskites. *Nature Physics*, **2015**, 11, 582-587.
- [114] J. S. Manser et al., Intriguing optoelectronic properties of metal halide perovskites. *Chemical Reviews*, **2016**, 116, 12956-13008.
- [115] G. Xing et al., Long-range balanced electron-and hole-transport lengths in organic-inorganic $\text{CH}_3\text{NH}_3\text{PbI}_3$. *Science*, **2013**, 342, 344-347.
- [116] S. D. Stranks et al., Electron-hole diffusion lengths exceeding 1 micrometer in an organometal trihalide perovskite absorber. *Science*, **2013**, 342, 341-344.
- [117] C. Wehrenfennig et al., High charge carrier mobilities and lifetimes in organolead trihalide perovskites. *Advanced Materials*, **2014**, 26, 1584-1589.

- [118] J. Chen et al., Enhanced Size Selection in Two-Photon Excitation for CsPbBr₃ Perovskite Nanocrystals. *The Journal of Physical Chemistry Letters*, **2017**, 8, 5119-5124.
- [119] D. Meggiolaro et al., Iodine chemistry determines the defect tolerance of lead-halide perovskites. *Energy & Environmental Science*, **2018**, 11, 702-713.
- [120] V. Adinolfi et al., The In-Gap Electronic State Spectrum of Methylammonium Lead Iodide Single-Crystal Perovskites. *Advanced Materials*, **2016**, 28, 3406-3410.
- [121] Y. Chen et al., Extended carrier lifetimes and diffusion in hybrid perovskites revealed by Hall effect and photoconductivity measurements. *Nature Communication*, **2016**, 7, 12253.
- [122] T. Leijtens et al., Carrier trapping and recombination: the role of defect physics in enhancing the open circuit voltage of metal halide perovskite solar cells. *Energy & Environmental Science*, **2016**, 9, 3472-3481.
- [123] D. W. de Quilettes et al., Impact of microstructure on local carrier lifetime in perovskite solar cells. *Science*, **2015**, 348, 683-686.
- [124] W.-J. Yi et al., Unusual defect physics in CH₃NH₃PbI₃ perovskite solar cell absorber. *Applied Physics Letters*, **2014**, 104, 063903.
- [125] A. Buin et al., Halide-dependent electronic structure of organolead perovskite materials. *Chemistry of Materials*, **2015**, 27, 4405-4412.
- [126] M. L. Agiorgousis et al., Strong covalency-induced recombination centers in perovskite solar cell material CH₃NH₃PbI₃. *Journal of the American Chemical Society*, **2014**, 136, 14570-14575.
- [127] A. Walsh et al., Self-Regulation Mechanism for Charged Point Defects in Hybrid Halide Perovskites. *Angewandte Chemie International Edition*, **2015**, 54, 1791-1794.
- [128] O. Malinkiewicz et al., Perovskite solar cells employing organic charge-transport layers. *Nature Photonics*, **2014**, 8, 128.
- [129] Y. Zhao et al., Organic-inorganic hybrid lead halide perovskites for optoelectronic and electronic applications." *Chemical Society Reviews*, **2016**, 45, 655-689.
- [130] T. Liu et al., Inverted perovskite solar cells: progresses and perspectives. *Advanced Energy Materials*, **2016**, 6, 1600457.
- [131] M. Xiao et al., A fast deposition-crystallization procedure for highly efficient lead iodide perovskite thin-film solar cells. *Angewandte Chemie International Edition*, **2014**, 53, 9898-9903.
- [132] Y. Wu et al., Retarding the crystallization of PbI₂ for highly reproducible planar-structured perovskite solar cells via sequential deposition. *Energy & Environmental Science*, **2014**, 7, 2934-2938.
- [133] J. W. Seo et al., Benefits of very thin PCBM and LiF layers for solution-processed p-i-n perovskite solar cells. *Energy & Environmental Science*, **2014**, 7, 2642-2646.

- [134] M. Konstantakou et al., Anti-solvent crystallization strategies for highly efficient perovskite solar cells. *Crystals*, **2017**, 7, 291.
- [135] J. Burschka et al., Sequential deposition as a route to high-performance perovskite-sensitized solar cells. *Nature*, **2013**, 499, 316.
- [136] K. Liang et al., Synthesis and characterization of organic–inorganic perovskite thin films prepared using a versatile two-step dipping technique. *Chemistry of materials*, **1998**, 10, 403-411.
- [137] Q. Chen et al., Controllable self-induced passivation of hybrid lead iodide perovskites toward high performance solar cells. *Nano Letters*, **2014**, 14, 4158-4163.
- [138] T. Liu et al., Mesoporous PbI_2 scaffold for high-performance planar heterojunction perovskite solar cells. *Advanced Energy Materials*, **2016**, 6, 1501890.
- [139] Z. Xiao et al., Efficient, high yield perovskite photovoltaic devices grown by interdiffusion of solution-processed precursor stacking layers. *Energy & Environmental Science*, **2014**, 7, 2619-2623.
- [140] T. Ibn-Mohammed et al., Perovskite solar cells: An integrated hybrid lifecycle assessment and review in comparison with other photovoltaic technologies. *Renewable and Sustainable Energy Reviews*, **2017**, 80, 1321-1344.
- [141] W. S. Yang et al., High-performance photovoltaic perovskite layers fabricated through intramolecular exchange. *Science*, **2015**, 348, 1234-1237.
- [142] M. M. Lee et al., Efficient hybrid solar cells based on meso-superstructured organometal halide perovskites. *Science*, **2012**, 1228604.
- [143] C. Zuo et al., Advances in perovskite solar cells. *Advanced Science*, **2016**, 3, 1500324.
- [144] N. Elumalai et al., Perovskite solar cells: progress and advancements. *Energies*, **2016**, 9, 861.
- [145] Z. Xiao et al., Giant switchable photovoltaic effect in organometal trihalide perovskite devices. *Nature Materials*, **2015**, 14, 193.
- [146] H. Zhang et al., Dynamic interface charge governing the current–voltage hysteresis in perovskite solar cells. *Physical Chemistry Chemical Physics*, **2015**, 17, 9613-9618.
- [147] J. H. Heo et al., Hysteresis-less inverted $\text{CH}_3\text{NH}_3\text{PbI}_3$ planar perovskite hybrid solar cells with 18.1% power conversion efficiency. *Energy & Environmental Science*, **2015**, 8, 1602-1608.
- [148] L. Meng et al., Recent advances in the inverted planar structure of perovskite solar cells. *Accounts of chemical research*, **2015**, 49, 155-165.
- [149] Y. Shao et al., Origin and elimination of photocurrent hysteresis by fullerene passivation in $\text{CH}_3\text{NH}_3\text{PbI}_3$ planar heterojunction solar cells. *Nature Communications*, **2014**, 5, 5784.
- [150] J. Xun et al., Perovskite–fullerene hybrid materials suppress hysteresis in planar diodes. *Nature Communications*, **2015**, 6, 7081.

- [151] J. Gong et al., Perovskite photovoltaics: life-cycle assessment of energy and environmental impacts. *Energy & Environmental Science*, **2015**, 8, 1953-1968.
- [152] P.-Y. Chen et al., Environmentally responsible fabrication of efficient perovskite solar cells from recycled car batteries. *Energy & Environmental Science*, **2014**, 7, 3659-3665.
- [153] A. L. Wani et al., Lead toxicity: a review. *Interdisciplinary Toxicology*, **2015**, 8, 55-64.
- [154] B. Hailegnaw et al., Rain on methylammonium lead iodide based perovskites: possible environmental effects of perovskite solar cells. *The Journal of Physical Chemistry Letters*, **2015**, 6, 1543-1547.
- [155] S. Carretero-Palacios et al., Plasmonic Nanoparticles as Light-Harvesting Enhancers in Perovskite Solar Cells: A User's Guide, *ACS Energy Letters*, **2016**, 1, 323-331.
- [156] W. R. Erwin et al., Light trapping in mesoporous solar cells with plasmonic nanostructures. *Energy & Environmental Science*, **2016**, 9, 1577-1601
- [157] M. Valenti et al., Plasmonic nanoparticle-semiconductor composites for efficient solar water splitting. *Journal of Materials Chemistry A*, **2016**, 4, 17891-17912.
- [158] A. Furube et al., Insight into plasmonic hot-electron transfer and plasmon molecular drive: new dimensions in energy conversion and nanofabrication. *NPG Asia Materials*, **2017**, 9, e454.
- [159] Z. Yuan et al., Hot-Electron Injection in a Sandwiched TiO_x-Au-TiO_x Structure for High-Performance Planar Perovskite Solar Cells. *Advanced Energy Materials*, **2015**, 5, 1500038.
- [160] G. Kakavelakis et al., Recent advances in plasmonic metal and rare-earth-element upconversion nanoparticle doped perovskite solar cells. *Journal of Materials Chemistry A*, **2017**, 5, 21604-21624.
- [161] H.L. Hsu et al., Enhanced efficiency of organic and perovskite photovoltaics from shape-dependent broadband plasmonic effects of silver nanoplates. *Solar Energy Materials and Solar Cells*, **2015**, 140, 224-231.
- [162] G. Kakavelakis et al., Efficiency and stability enhancement of inverted perovskite solar cells via the addition of metal nanoparticles in the hole transport layer. *RSC Advances*, **2017**, 7, 12998-13002.
- [163] P. Liu et al., Improving power conversion efficiency of perovskite solar cells by cooperative LSPR of gold-silver dual nanoparticles. *Chinese Physics B*, **2017**, 26, 058401.
- [164] R. Wu et al., Prominent efficiency enhancement in perovskite solar cells employing silica-coated gold nanorods. *The Journal of Physical Chemistry C*, **2016**, 120, 6996-7004.

Chapter 3

Plasmonic anisotropic gold nanoparticles: synthesis and characterization

3.1 Introduction

In this chapter the experimental protocols for the synthesis and purification of plasmonic gold nanoparticles are reported. In particular, anisotropic Au@PVP nanoparticles are synthesized by adapting a method reported in literature^[1]. In addition a procedure for coating them with an insulating silica shell was optimized. The optical and morphological characterizations of the nanoparticles involving UV-Vis-NIR spectroscopy and transmission electron microscopy (TEM) are presented. Because of the polydispersity of the nanoparticles a rigorous determination of their concentration in solution was hard, however it was possible to estimate it.

3.2 Anisotropic Au@PVP nanoparticles

3.2.1 Synthetic procedure

The synthetic protocol has been adapted from a method reported in literature^[1].

The glassware used for the synthesis was carefully cleaned to remove traces of contaminants that can significantly interfere with the formation of nanoparticles. Therefore, the glassware was washed with detergent, distilled water, then soaked in aqua regia to remove metal ions and other residues contaminants and finally rinsed with ultrapure water (resistivity of 18.2 M Ω ·cm).

1 mL of 10 mM hydrogen tetrachloroaurate (III) hydrate (HAuCl₄·3H₂O, purity \geq 99.9% trace metals basis, Sigma Aldrich) aqueous solution and 0.2 mL of 10 mM trisodium citrate (Na₃C₆H₅O₇·2H₂O, purity > 99 %, Sigma Aldrich) aqueous solution were added to 18.5 mL of ultra-pure water. Under vigorous stirring (800 rpm), 0.5 mL of 0.1 M sodium borohydride (NaBH₄, purity >98%, Acros Organics) aqueous solution was added and an immediate chromatic variation of the solution from light yellow to red was observed, due to the seeds formation. After 5 minutes, the stirring was stopped and the solution was left undisturbed

for 3h, to complete the seeds formation before their subsequent use in the growth step. After this time, 200 μL of the seed solution was injected under stirring in a mixture prepared by adding 1 mL of 10 mM HAuCl_4 and 2 mL of 2 mM polyvinylpyrrolidone (PVP, average MW 10,000 g/mol, purity $\geq 99\%$, Sigma Aldrich) aqueous solution to 19 mL of ultrapure water. Finally 90 μL of 30% hydrogen peroxide solution (H_2O_2 , Sigma Aldrich) were added to accomplish the seed growth of Au nanoplates and the reaction was left to proceed for 3h at room temperature.

3.2.2 Purification procedure

In order to remove excess PVP at the end of the reaction, the dispersion was subjected to a centrifugation process. It was transferred into a centrifugal concentrator (Vivaspin Sartorius) which consists of a tube of polycarbonate with a polyethersulphone membrane (porosity of 100 KDa) in the middle that separates the tube in two regions. An Hermlez Z300 centrifuge was used and a speed 1250 rpm was set. Due to the centrifugal force, the liquid with all dissolved PVP and other reaction residuals passes through the membrane, while the nanoparticles concentrate on it in the upper region of the tube.

By avoiding that nanoparticles were completely dry when the liquid was removed, a fresh solvent was added in the upper region of the tube and the process is repeated twice more. Finally, the nanoparticles were dispersed in 10 mL of ultrapure water. In this way a quantitative recovery of the purified nanoparticles was possible.

3.2.3 Nanoparticles characterizations

The absorption spectra of the seeds and anisotropic gold nanoparticles were acquired and they are showed in figure 3.1. The seeds spectrum presents only a band centered at 505 nm typical of spherical Au nanoparticles, while the spectrum of the grown nanoparticles have two bands centered at 532 nm and at 669 nm, respectively. The first band is due to the contribution of spherical nanoparticles with bigger size than the seeds and to the quadrupolar resonance mode of gold nanotriangles. The second band at longer wavelength, that clearly indicates the development of anisotropic shapes during the growth phase, is due to the dipolar resonance mode of the gold nanotriangles. The presence of a shoulder close to band at 669 nm derives from the polydispersity of the nanoparticles.

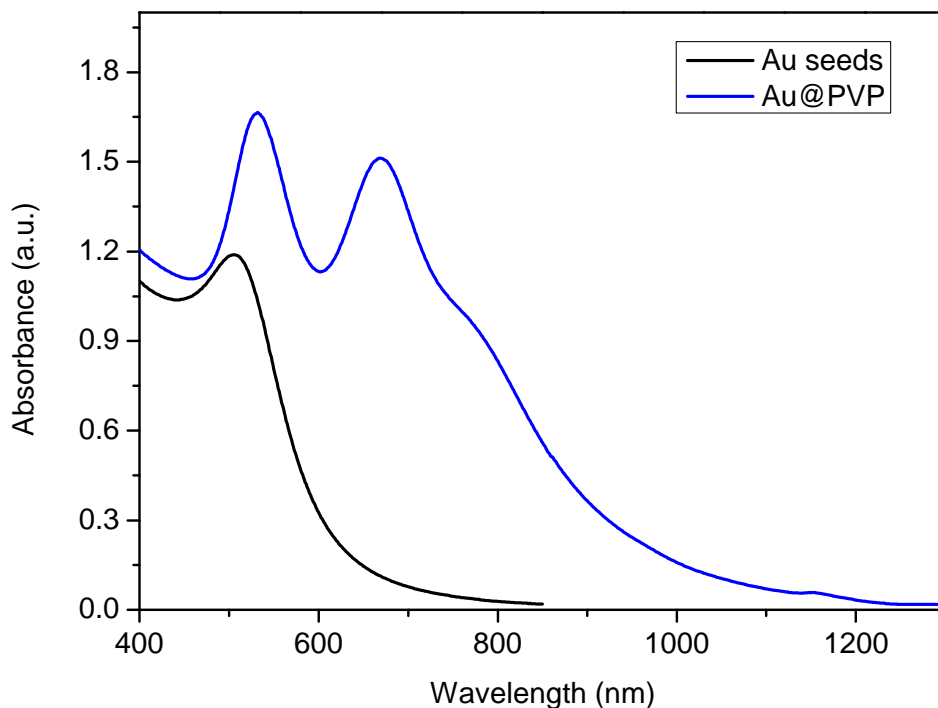


Figure 3.1 Absorption spectra of the Au seeds and Au@PVP nanoparticles dispersions obtained adding 90 μL of H_2O_2 .

To investigate the morphology of the nanoparticles TEM images were acquired. As can be observed in Figure 3.2 the seeds are spherical and monodisperse, while the grown nanoparticles are characterized by wide size and shape distributions. Nanoparticles with triangular, hexagonal and spherical shapes can be observed in the micrograph. In figure 3.3 the thin layer of PVP around the nanoparticle can be observed.

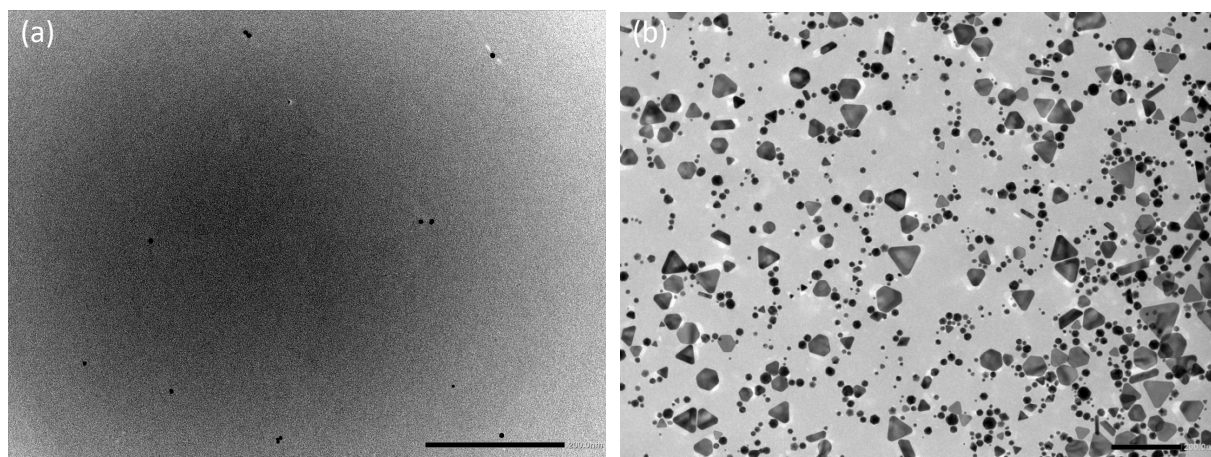


Figure 3.2 TEM micrographs of the Au seeds (a) and of the Au@PVP nanoplates obtained using 90 μL of H_2O_2 (b)(scale bar, in both images, correspond to 200 nm).

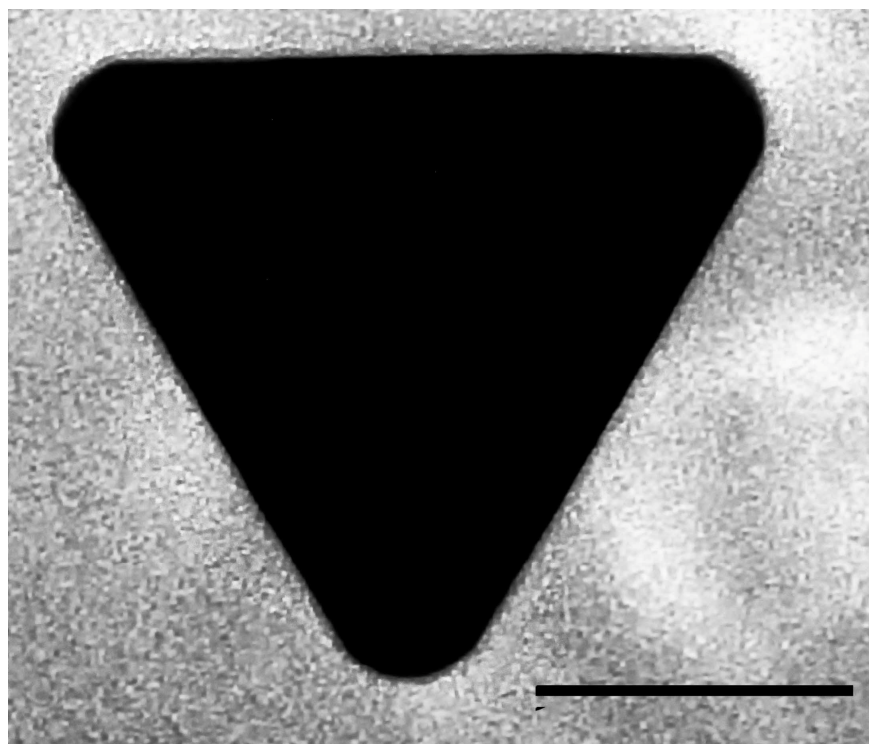


Figure 3.3 TEM micrograph of a gold nanotriangle in which can be observed the thin PVP layer (scale bar correspond to 50 nm).

The concentration of the nanoparticles in colloidal solution can be calculated using the Lambert-Beer law:

$$A = \epsilon bc \quad (3.1)$$

where A is the absorbance of the solution, ϵ ($\text{M}^{-1}\text{cm}^{-1}$) is the molar absorptivity, b (cm) is the path length and c (M) is the concentration of the nanoparticles. The values of ϵ for citrate-stabilized gold nanospheres versus average size are reported in literature^[2]. Therefore, measuring the absorbance of the seed solution, it is possible to calculate their concentration.

In the case of anisotropic nanoparticles, due to their polydispersity and to the lack of tabulated molar absorptivity values, the determination of the concentration through the Lambert-Beer law is not possible. However, assuming that each nanoparticles was grown from a seed^[1] it is possible to estimate their number referring to the seeds spectra.

3.3.4 Tuning the size of Au@PVP nanoparticles

The volume of H_2O_2 added to the seeds dispersion during the growth phase is decisive for controlling the aspect ratio of the anisotropic nanoparticles. As can be seen in figure 3.4, by

decreasing the volume of H_2O_2 from 90 μL to 2 μL the in-plane dipolar resonance band of Au nanoparticle red-shifted, indicating the increase of the aspect ratio and at the same time an increase of the full width half maximum of the band is observed corresponding to a greater size distribution.

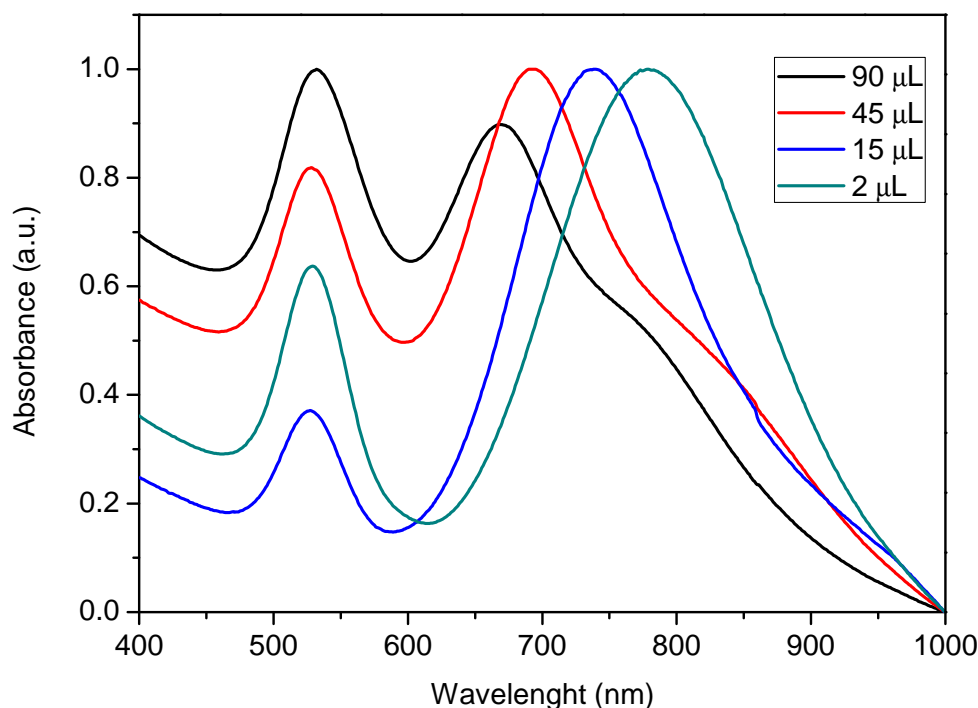


Figure 3.4 Normalized absorption spectra of nanoparticle dispersions obtained employing different volumes of H_2O_2 .

3.3 Synthesis of Au@SiO_2 nanoparticles from Au@PVP nanoparticles

Metallic nanoparticles integrated in solar cells, if not electrically insulated, could act as charge recombination center or exciton quenchers when in contact with the active layer. In order to obtain gold nanoparticles coated with a shell of insulating material, suitable for incorporation at the interface between the HTL and the active layer of a solar cell, a modified method developed by Graf was adopted^[3]. This method is based on the coating of a generic nanoparticle with a silica shell exploiting the presence on the surface of the nanoparticle of a primer such as PVP.

It simultaneously allows to have stable nanoparticles in ethanolic/ammonia solution required by Stöber's synthesis and to anchor on their surface the hydrolyzed form of the silica precursor used, tetraethoxysilane, that undergoes auto-condensation forming the shell.

It is important to underline that the protocol reported in literature is relative to the growth of silica shell starting from monodisperse metallic nanoparticles while our system is more complex due to the size and shape distribution of the nanoparticles. An additional difficulty to obtain a uniform covering of the metallic core as well as high stable nanoparticle dispersions is represented by the thickness of the silica layer because a thin shell is needed (not more than about 5 nm) to induce effect in the photovoltaic cells. For these reasons, the protocol optimization has required a huge investigation effort for both the synthetic and the subsequent purification steps. Below, the main adaptations of the initial protocol according to the progressive results obtained are described in detail.

3.3.1 Synthesis, purification and characterization of Au@SiO₂: initial protocol

Au@PVP nanoparticles were synthesized using the protocol described in the paragraph 3.2.1 and purified in ethanol. 1.5 mL of this dispersion were added to 1.5 mL of absolute ethanol. Subsequently, 50 μ L of hydroxyl ammonium solution (NH₄OH, 28 % NH₃ in H₂O, Sigma Aldrich) were added under gentling stirring, followed by 5 μ L of tetraethyl orthosilicate (TEOS, purity \geq 99%, Sigma Aldrich). The reaction was allowed to proceed for 2h at room temperature. Afterwards, the dispersion was centrifuged at 4000 rpm for 40 min. The supernatant, that showed a slight red coloration, was separated and the nanoparticles were dispersed in 3 mL of absolute ethanol. The centrifugation step was repeated again.

The absorption spectra of the dispersions before and after the silica coating were acquired and shown in figure 3.5. Considering the band at longer wavelength relative to the Au@SiO₂ nanoparticles, a red-shift with respect to the band of the Au@PVP nanoparticles indicates that the coating process has taken place (silica has a greater refractive index than water). However, the bandwidth widening means that aggregation occurred.

The band centered at 520 nm relative to the Au@SiO₂ nanoparticles is considerably less intense than the corresponding band of the Au@PVP nanoparticles. This is due to an incomplete recovery of the nanoparticles under the centrifugal conditions adopted. On the other hand, the slight color of the supernatant supports this conclusion. The possibility to improve nanoparticle recovery by increasing the centrifugation speed has been ruled out, since it determinates a greater impact force between the nanoparticles and therefore a more intense aggregation process.

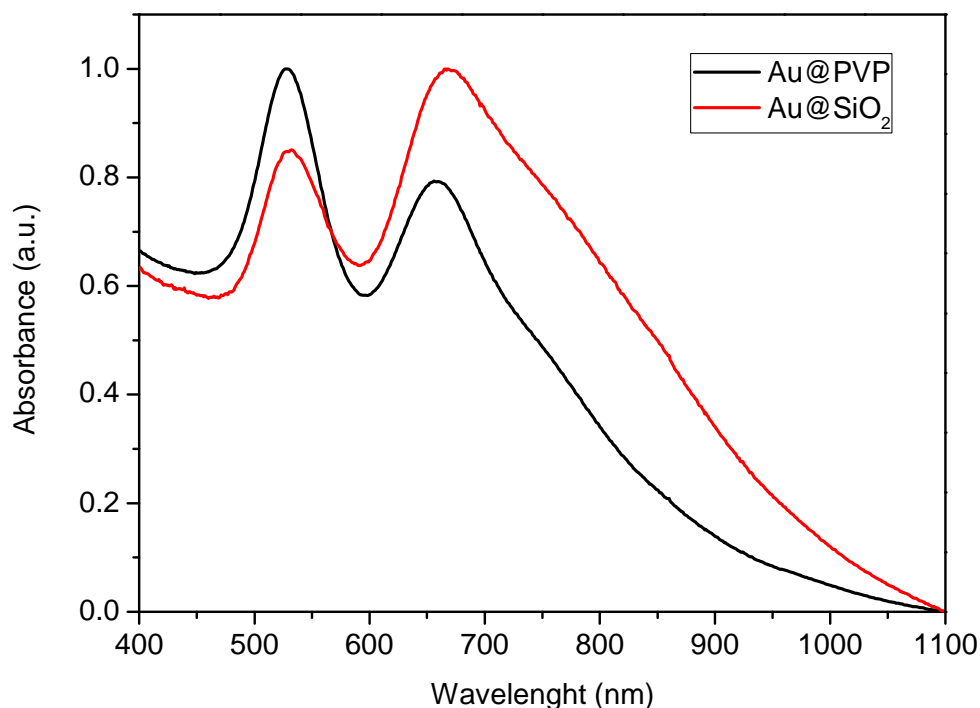


Figure 3.5 Normalized absorption spectra of Au@PVP and Au@SiO₂ nanoparticles obtained adopting the initial synthetic protocol.

To confirm these results, TEM analysis of both the supernatant and the Au@SiO₂ nanoparticles was performed; the acquired images are reported in figure 3.6.

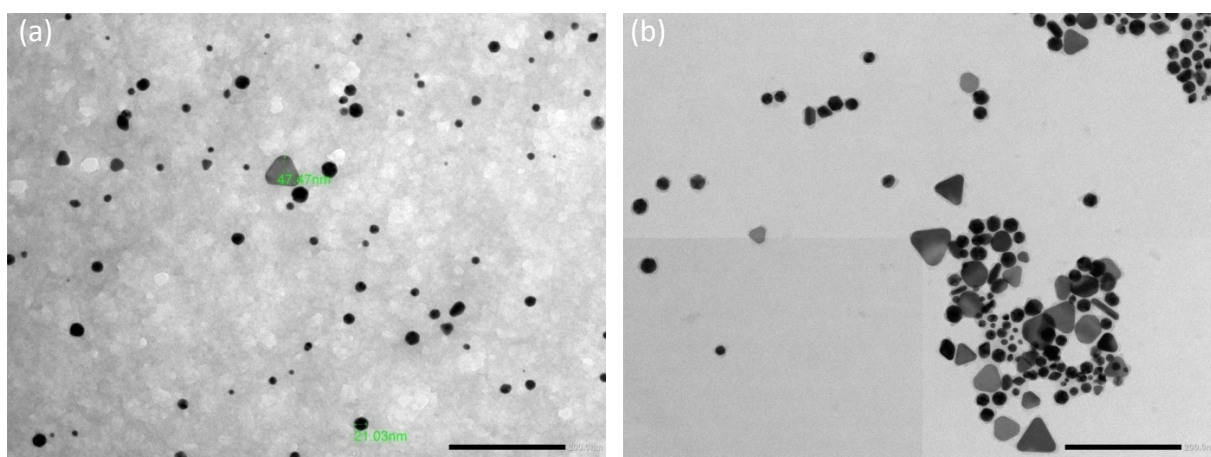


Figure 3.6 TEM micrographs of supernatant (a) and Au@SiO₂ nanoparticles obtained adopting the initial synthetic protocol (b) (scale bar correspond to 200 nm).

As can be seen in figure 3.6(a), the supernatant contains a significant number of nanoparticles for the most part spherical, while observing figure 3.6(b) a coating around the nanoparticles is evident, although unwanted aggregates structures are also present. The last are formed by condensation between the silanol groups on the surface of the nanoparticles

that can occur during the synthesis or the purification process. To establish when aggregations between nanoparticles take place, a TEM analysis was performed on non-purified Au@SiO₂ nanoparticles.

As shown in figure 3.7 there are no aggregates, therefore it can be concluded that aggregation occurs during the purification step.

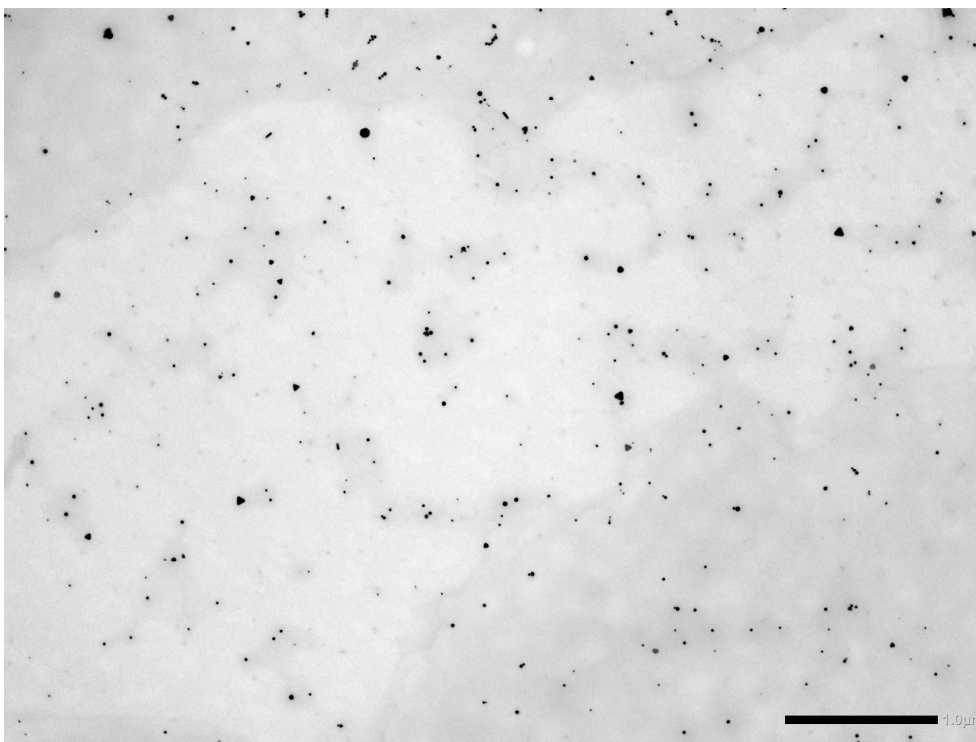


Figure 3.7 TEM image of non-purified Au@SiO₂ nanoparticles (scale bar correspond to 1 μm).

By focusing the interest on the silica shell, from figure 3.6(b) it can be observed that the obtained thickness is smaller than the optimal value (5 nm). For this reason a new synthesis was achieved following the protocol described above and increasing only the volume of TEOS added from 5 to 10 μL; the purification step was not changed. As can be seen by the TEM image in figure 3.8(a) the thickness of the shell obtained increasing the amount of TEOS is optimal. However, as shown by figure 3.8(b) the aggregation of the Au@SiO₂ nanoparticles persists.

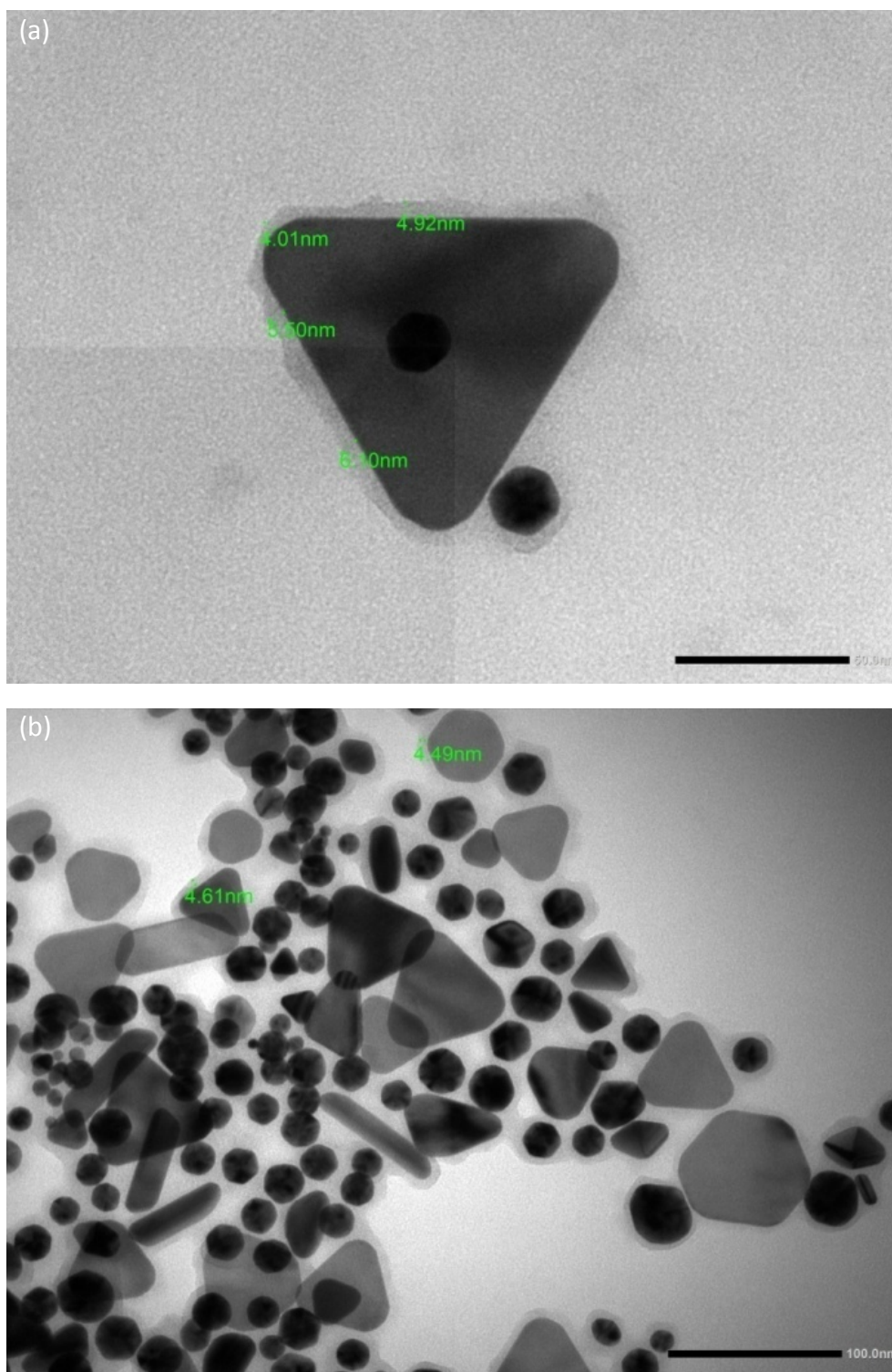


Figure 3.8 TEM images of the purified nanoparticles obtained using 10 μl of TEOS. Single Au@SiO₂ nanotriangles (a) and aggregate of Au@SiO₂ nanoparticles (b) (scale bar correspond to 50 nm in (a) and 100 nm in (b)).

A further limit of the purification process is the incomplete removal of the reaction residues, as can be observed in figure 3.9 that shows a large area of the membrane of TEM grid on which purified Au@SiO₂ nanoparticles were deposited: the nanoparticles (black objects) are

surrounded by an accumulation of reaction residues (dark grey areas around the nanoparticles).

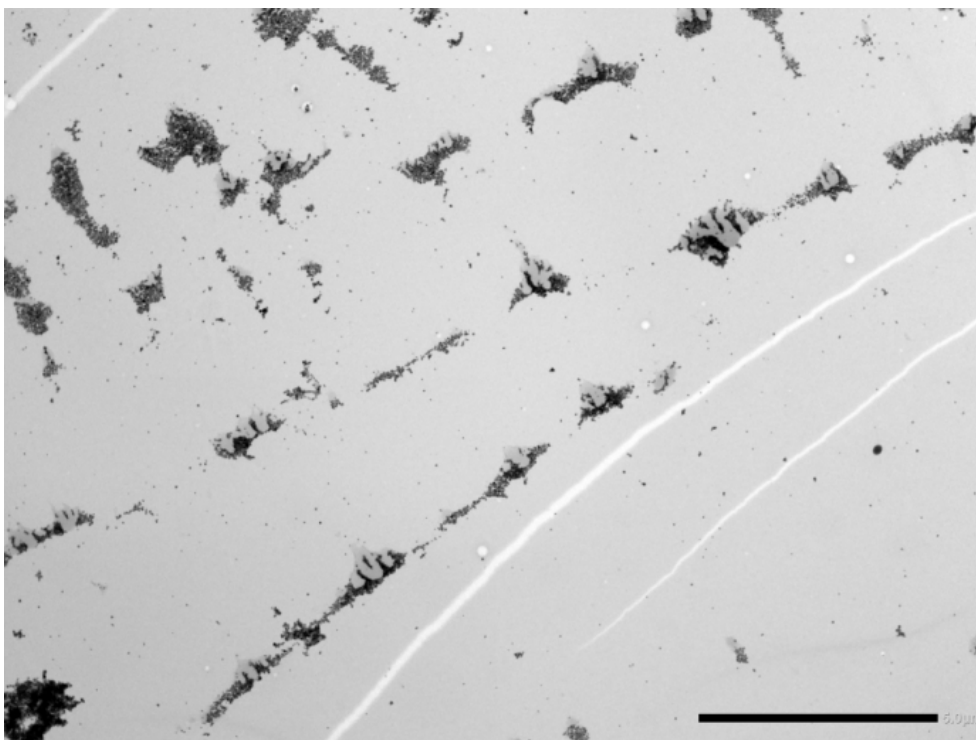


Figure 3.9 TEM image showing the incomplete purification of the Au@SiO₂ nanoparticles. Dark grey areas correspond to reaction residues (scale bar correspond to 5μm).

The removal of reaction residues by further centrifugation cycles was not possible without causing irreversible aggregations of the nanoparticles, which could not be dispersed even under sonication.

Considering the problems described, a different purification method involving the use of centrifugal concentrators was taken into account. Centrifugal concentrators permit to separate the reaction residues from the nanoparticles at low centrifugal speed. In this way, the nanoparticles are subject to lower energy impact and therefore the probability of aggregation decrease. Moreover, by using the centrifugal concentrators it is also possible the quantitatively recovery of the nanoparticles. On the basis of these considerations, the purification of the Au@SiO₂ nanoparticles was accomplished by centrifugal concentrator at 1250 rpm. Several cycles were performed, but the nanoparticles aggregate before they were completely purified.

3.3.2 Synthesis, purification and characterization of Au@SiO₂: a modified protocol

The developed synthetic procedure permits to cover the nanoparticles with a uniform and complete silica shell. However, it requires a large amount of TEOS that can not be completely removed in the purification steps without causing the aggregation of the nanoparticles and, for this reason, it was necessary to modify the synthetic protocol. It was chosen to reduce the initial concentration of the nanoparticles, because in this way the relative distance and consequently the interaction between them decrease. In addition, the amount of TEOS added was reduced in order to limit the unreacted silica precursors to be removed during the purification step. As a consequence of the decreased concentration of TEOS, the reaction kinetics is slower compared to the previous protocol, so the reaction time has been increased. Since the volume of pure TEOS to be used in the modified procedure is very low, a 2% v/v TEOS solution in ethanol was prepared.

In table 3.1 are reported the modified parameters with respect to the procedure described in the paragraph 3.3.

Table 3.1 Reaction conditions of initial and modified protocol for the covering of Au@PVP nanoparticles with a silica shell.

Parameter	Initial protocol	Modified protocol
Au@PVP nanoparticle volume (mL)	1.5	0.5
Ethanol volume (mL)	1.5	2
TEOS (μ L)	10 (pure)	50 (2% v/v in ethanol)
Reaction time (h)	2	16

To remove the residuals and purify the product, it was decided to use the centrifugal concentrators and to perform three cycles of centrifugation at 1250 rpm; after each cycle, 10 mL of pure ethanol were added to the dispersion with nanoparticles. At the end of the last cycle, the nanoparticles were dispersed in 1 mL of pure ethanol.

TEM measurements have shown a complete coating of the nanoparticles with an average thickness of the silica shell of about 3 nm, as shown in figure 3.10. Moreover, no reaction residuals were observed on the membrane of TEM grid.

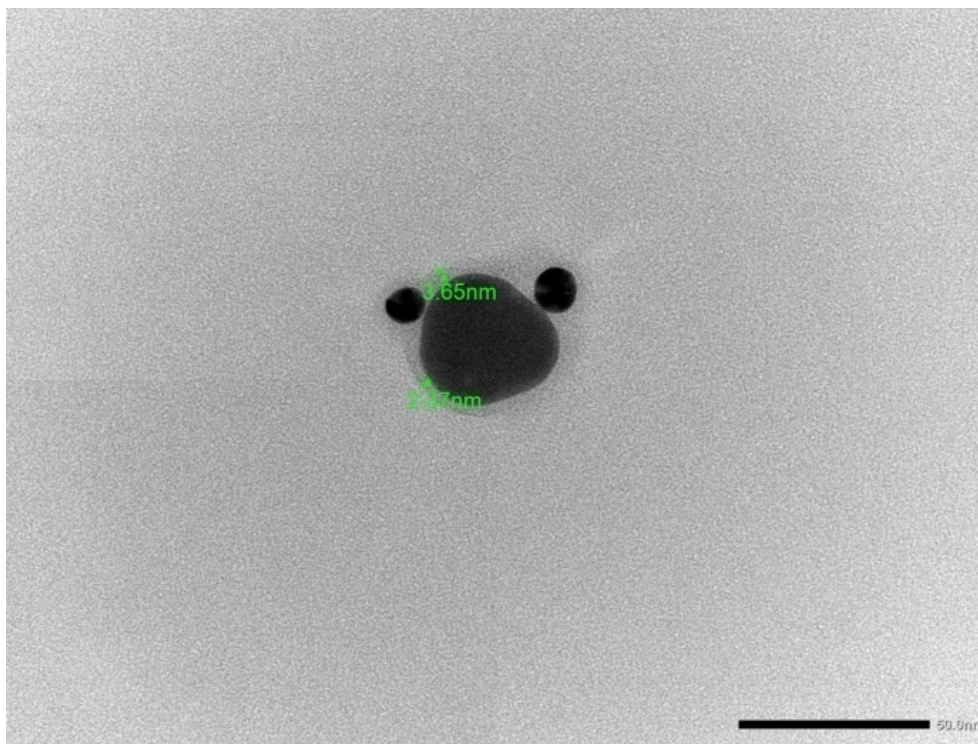


Figure 3.10 Au@SiO₂ nanoparticles obtained with the modified protocol (scale bar correspond to 50 nm).

Although the shell could be too thin to completely insulate the metallic core, it was chosen to fabricate some plasmonic organic solar cells by depositing these nanoparticles at the interface between the hole transport layer (HTL) and the active layer, as described in detail in Chapter 4. It was observed that the integration of the nanoparticles at the interface produced a reduction of the performance of the devices with respect to those of the reference devices without nanoparticles. Furthermore, the detrimental effect tended to decrease by increasing the dilution of the ethanolic nanoparticle dispersion deposited above the HTL.

The lower cell performances could be related to the nanoparticles, which were not completely isolated due to the reduced thickness of the silica shell, or to unwanted products/substances in dispersion that, deposited at the interface, hindered the charge transport. The presence of reaction residuals in dispersion was excluded by TEM observations, but to determinate if the centrifugal concentrator, used for nanoparticle purification, could release undesirable substances not observable to TEM, further investigation were accomplished. In particular, some devices were produced by depositing ethanol, which was previously poured in a centrifugal concentrator and subject to the same centrifugation process used for nanoparticles purification, on the HTL. As reference, samples with pure ethanol were fabricated.

It was found that the solar cells produced with pretreated ethanol did not show the electrical problems of the plasmonic devices, however their performances were notably reduced with respect to the reference devices. It was so possible to conclude that even though the electrical problems were due to the insufficient electrical insulation of the nanoparticles, the centrifugal tube made of polycarbonate could release bisphenol^[4] that deposited at the interface produced the worsening of the cell performances.

Considering the experimental evidences described, the optimization of the synthetic procedure to obtain a thicker silica shell was necessary. Moreover, since centrifugal concentrators in polycarbonate can not be used for the purification of the nanoparticles, a different procedure involving vials of polypropylene, fully compatible with the ethanol, was planned.

To efficiently separate the nanoparticles using vials without porous membrane, high centrifugation speeds are necessary. However, as previously described, nanoparticles aggregation can occur due to the highly energetic impact between them. To overcome this obstacle, it was thought to add at the end of the reaction for the synthesis of Au@SiO₂ nanoparticles, prior of the centrifugation, an excess of water to the dispersion of nanoparticles. In this way they are less concentrated, so the probability of aggregation during centrifugation is reduced. At the same time the unreacted TEOS, less dense and immiscible with water, can be removed with the supernatant.

Experiments aimed to optimize this new purification procedure are ongoing. The next step will be the refining of the reaction conditions reported in table 3.1 in order to obtain Au@SiO₂ nanoparticle with an optimal silica shell.

It is important to underline an aspect observed during the experimental work. In particular, it is essential to accomplish silica shell growth within few days after the synthesis of the Au@PVP nanoparticles. Indeed, if this time is longer than a week, the silica coating around the metallic core could be incomplete, as can be seen in figure 3.11.

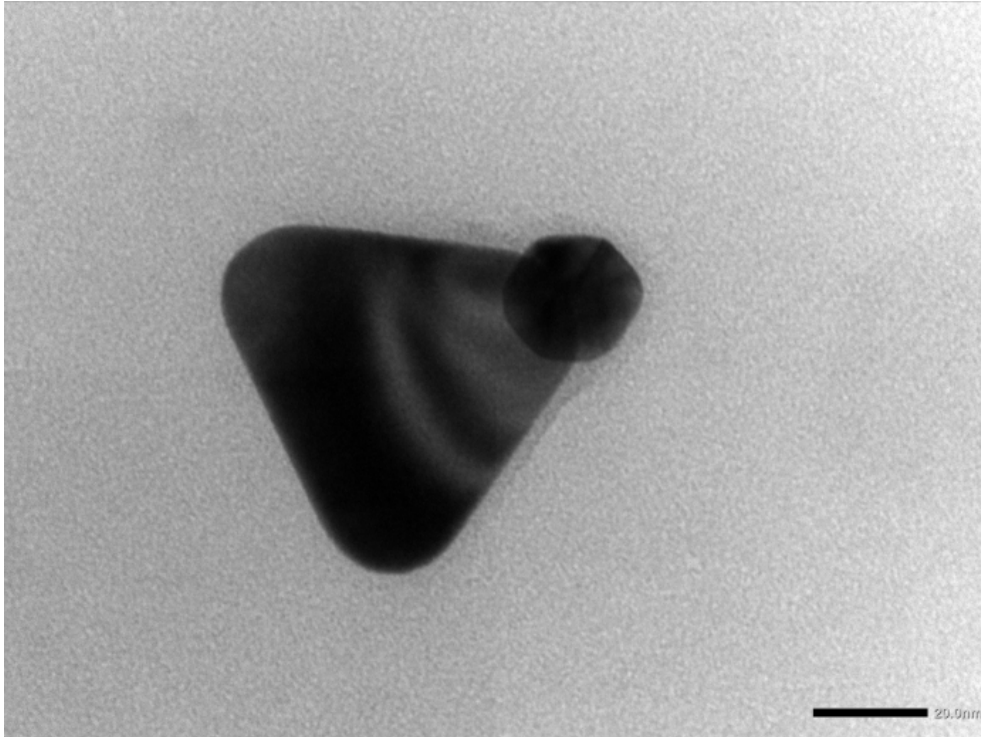


Figure 3.11 TEM image showing the incomplete silica shell on a Au@PVP nanoparticle synthesized 7 days before (scale bar correspond to 20 nm).

This could be due to the PVP desorption from the surface of the nanoparticle during storage, with the consequence that its function as a primer for the growth of silica shell is lost.

3. 4 References

- [1] G. Wang et al., High-yield halide-free synthesis of biocompatible Au nanoplates. *Chemical Communications*, **2016**, 52, 398-401.
- [2] X. Liu et al., Extinction coefficient of gold nanoparticles with different sizes and different capping ligands. *Colloids and Surfaces B: Biointerfaces*, **2017**, 58, 3-7.
- [3] C. Graf et al., A general method to coat colloidal particles with silica. *Langmuir*, **2003**, 19, 6693-6700.
- [4] E. J. Hoekstra et al., Release of bisphenol A from polycarbonate: a review. *Critical Reviews in Food Science and Nutrition*, **2013**, 53, 386-402.

Chapter 4

Plasmonic organic solar cells

4.1 Introduction

In this chapter the experimental work relative to the integration and the study of the effects of anisotropic Au@PVP nanoparticles into organic solar cells is described in detail.

As a reference cell it was chosen the well studied structure glass/ITO/PEDOT:PSS/P3HT:PC₆₁BM/Al. A protocol previously optimized by the research group of our laboratory was initially used for the fabrication of the organic devices. However, due to reproducibility problems of the devices, it was necessary to modify the protocol.

Au@PVP nanoparticles were introduced into the hole transport layer of the cells. After a preliminary optimization of the incorporation procedure, a study of the effects of the nanoparticles on the cells was accomplished through electrical, optical and morphological characterizations. Further experiments, in which the Au@PVP nanoparticles were introduced at the interface between the hole transport layer and the active layer, were conducted with the aim to reduce the distance between the nanoparticles and the active layer, in order to maximize the influence of plasmonic field on the active layer of the devices. However, because the PVP coating was not sufficient to electrically insulate the metallic core, the introduction of the Au@PVP nanoparticles has led to the deterioration of the device performances. It was necessary therefore to develop a synthetic protocol to insulate the nanoparticle with a silica shell as reported in Chapter 3. The difficulties encountered in the optimization of the synthesis and purification of Au@SiO₂ with appropriate shell thickness have limited the full achievement of the study of the effects produced by the nanoparticles at the PEDOT:PSS/P3HT:PC₆₁BM interface.

4.2 Optimization of the protocol for the fabrication of the reference cells

The first reference devices were fabricated according to the following procedure. Patterned ITO-coated glass substrates (ITO thickness 115-120 nm, sheet resistivity 12 Ω/sq, UNAXIS) were sequentially cleaned by ultrasonication in deionized water with detergent, deionized water, acetone and 2-propanol for 15 minutes. Substrates were treated with air plasma

(Diener Electronics, Model Femto) at 100% power for 5 minutes in order to remove residual organic contaminants and to activate the surface for the subsequent film deposition. PEDOT:PSS dispersion (1:6 weight ratio, suspension in water, solid content 1.3 – 1.7 % w/V, Heraeus Clevis PVP Al 4083, H.C. Starck), previously filtered by using a 0.45 μm PVDF syringe filter, was deposited by spin coating at 3000 rpm for 60 s and then the substrates were annealed at 140 °C for 15 minutes. A 17 mg/mL P3HT:PC₆₁BM (1:0.7 w/w) (P3HT, Regioregularity: 91-94%, 4002-EE, Rieke Metals Inc.; PC₆₁BM, Nano-C) blend in chlorobenzene (CB, anhydrous, 99.8%, Sigma-Aldrich) was spin coated at 700 rpm for 60 s; the samples were annealed at 75 °C for 10 minutes and then introduced inside a thermal evaporator for the deposition of the back electrode. 200 nm of aluminum were thermally evaporated at a pressure of 5×10^{-6} mbar and successively the samples were subject to an annealing treatment at 150 °C for 30 minutes. Devices manufactured following the previous protocol were electrically characterized under an irradiance of 1000 W/m² at air mass (AM) 1.5G. Irradiation of the samples was achieved by a solar simulator (Sciencetech, Model SS150) with an adequate set of filters to achieve a solar spectrum with AM 1.5G. The solar simulator light intensity was tuned by using a calibrated Silicon (Si) photodiode (Hamamatsu S2386-44K). It was observed that the characteristic curves of some samples showed an anomalous shape compared to the typical diode curve, resulting in a low fill factor and consequently in a low efficiency of the devices. This typology of curves, characterized by the presence of an inflection point, is known in the literature as S-shaped curve and figure 4.1 reports an example. The anomaly is due to an accumulation of charge inside the cells that can not be extracted by the electrode^[1]. The identification of the cause of the S-shaped anomaly was difficult because the problem occurred randomly also within a group of samples prepared at the same time under identical conditions. Numerous experiments were made by changing one parameter at a time during the cells fabrication; although the conditions of deposition and treatment of the various layers have been modified, the problem persisted. Through an extensive research on the topic, a paper was found in literature in which the authors demonstrate to improve the reproducibility of devices, with a structure similar to that adopted in this research work, introducing an additional layer of PC₆₁BM between the active layer and the aluminum electrode^[2].

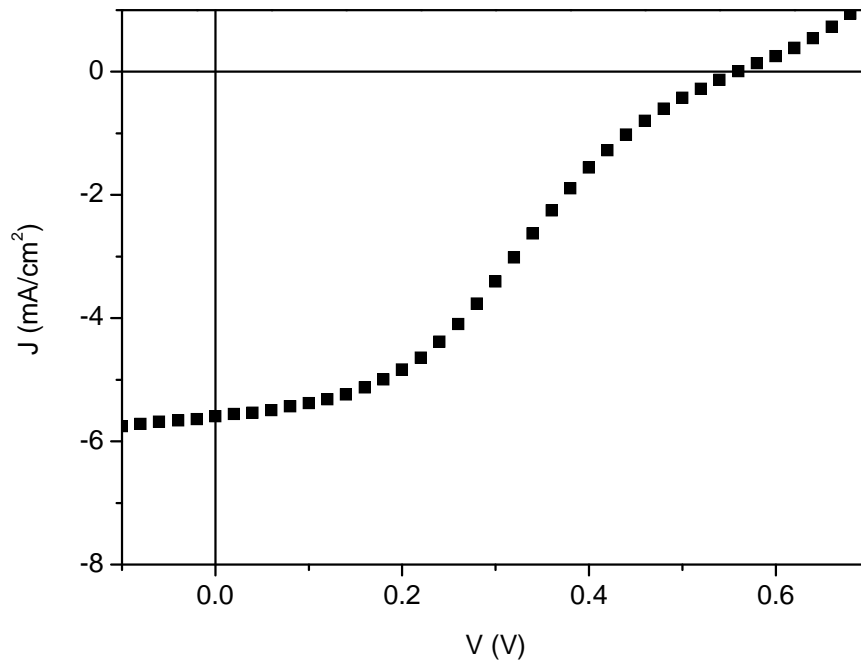


Figure 4.1 Typical S-shaped characteristic curve.

Due to excessive vertical phase separation in the P3HT:PC₆₁BM blend, the PC₆₁BM accumulated on the bottom of the film causing a poor contact with the cathode and consequently a reduced electron extraction. Therefore, by depositing the additional PC₆₁BM layer, they obtained a good electrical contact between the active layer and the cathode and consequently a high reproducibility of the samples.

With the aim of identifying the origin of the reproducibility problem in our work, the same strategy was applied. All the devices made with an additional layer of PC₆₁BM did not show S-shaped characteristic curves; therefore, the focus was on the active layer/electrode interface. Micrometric aggregates on the surface of the active layer of samples with low FF were observed through an optical microscope (figure 4.2).

Considering the results obtained with the additional layer of PC₆₁BM and the morphology of the microstructures, similar to that defined in literature as needle and chromosome like shape^[3], it was concluded that the aggregates came from an excessive segregation of PC₆₁BM^[4]. In our case, however, the phenomenon involved is an excessive horizontal phase separation rather than a vertical one. To optimize the phase separation between the two components of the active layer during the film formation, a processing additive technique^[5] was used. It consists in the addition of a small volume of a solvent with particular requirements to the active layer blend solution.

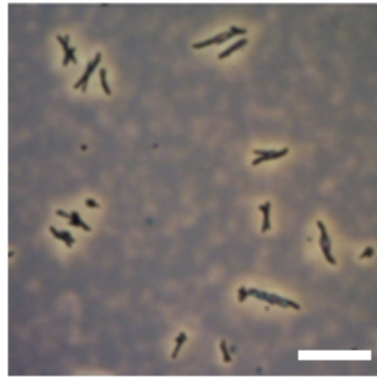


Figure 4.2 Optical microscope image of the P3HT:PC₆₁BM active layer (scale bar correspond to 50 μm).

In particular, the processing additive must be a selective solvent for a component of the blend and have a higher boiling point than the host solvent^[6]. 1,8-diiodooctane was chosen as processing additive to improve the cell reproducibility. Since it is a selective solvent for the PC₆₁BM and has a higher boiling point than the CB host solvent, the PC₆₁BM remains in solution during the film drying for a longer time than P3HT. In this way P3HT tends to self-stack producing orderly domains, while excessive PC₆₁BM aggregation is hindered.

In order to establish the optimal amount of processing additive to obtain performing and reproducible solar cells, solutions 17 mg/mL of P3HT:PC₆₁BM (1:0.7 w/w) in CB respectively with 1% (v/v), 2% (v/v) and 5% (v/v) of 1,8-diiodooctane were prepared and used to manufacture solar cells following the protocol previously described.

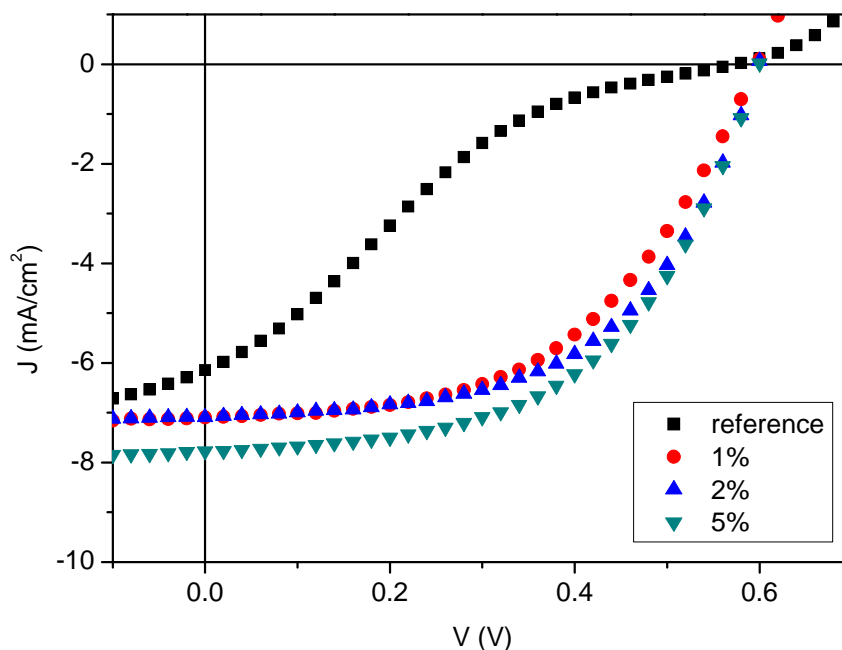


Figure 4.3 Representative J-V curves of the devices at different concentrations of 1,8-diiodooctane.

Figure 4.3 shows some representative characteristic curves of the samples at different concentrations of 1,8-diiodooctane, while in table 4.1 are summarized the principal figures of merit.

Table 4.1 Summary of the average photovoltaic parameters of the devices with different concentrations of 1,8-diiodooctane. Each value represents the average of 12 replicates.

Device	Description	FF	V_{oc} (V)	$-J_{sc}$ (mA/cm ²)	PCE (%)
A_{REF}	Reference	0.17 ± 0.01	0.52 ± 0.04	5.74 ± 0.21	0.51 ± 0.07
A1	1,8-diiodooctane (1% v/v)	0.51 ± 0.03	0.59 ± 0.01	7.40 ± 0.18	2.25 ± 0.14
A2	1,8-diiodooctane (2% v/v)	0.53 ± 0.04	0.60 ± 0.01	7.64 ± 0.20	2.43 ± 0.16
A3	1,8-diiodooctane (5% v/v)	0.54 ± 0.02	0.60 ± 0.01	7.68 ± 0.16	2.48 ± 0.14

With the addition of the 1,8-diiodooctane in the blend solutions, none of the samples produced showed S-shaped characteristic curve. However, since the addition of 5% (v/v) allows to obtain the most performing devices, it was decided to adopt this value for the manufacture of the reference cell. To confirm the effect of the processing additive on the PC₆₁BM aggregation an active layer film obtained from a blend solution with 5% (v/v) of 1,8-diiodooctane was observed with optical microscope. As can be seen in figure 4.4 the size of the aggregates is considerably reduced respect to the sample without 1,8-diiodooctane.

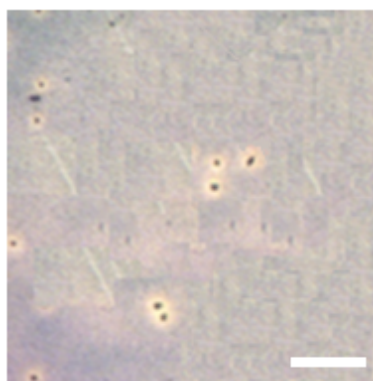


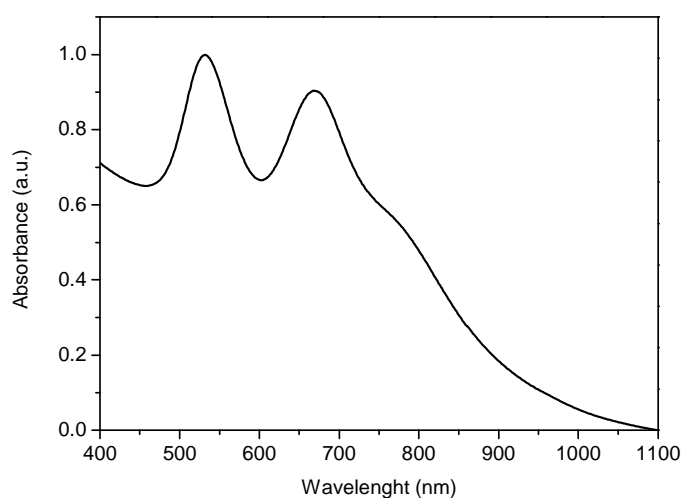
Figure 4.4 Optical microscope image of the P3HT:PC₆₁BM active layer obtained adding 5% (v/v) of 1,8-diiodooctane in the blend solution (scale bar correspond to 50 μm).

4.3 Optimization of the Au@PVP nanoparticles incorporation in PEDOT:PSS thin film

To integrate Au@PVP nanoparticles into the PEDOT:PSS, 100 μL of the Au@PVP aqueous dispersion, synthesized following the protocol reported in paragraph 3.2 using 90 μL of H_2O_2 , was added to 1 mL of PEDOT:PSS dispersion.

Figure 4.5 reports the normalized UV-Visible spectra of the Au@PVP aqueous dispersion and the corresponding TEM micrograph. The estimated nanoparticles concentration was 5.87×10^{11} particles/mL.

(a)



(b)

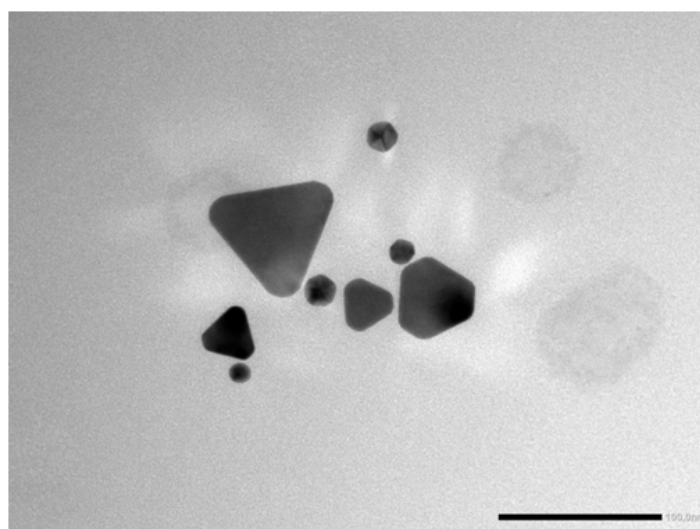


Figure 4.5 Normalized UV-Visible spectrum of the aqueous dispersion of the Au@PVP nanoparticles (a) and TEM micrograph of the nanoparticles (b) (scale bar 100 nm).

The final mixtures were agitated on a vortex mixer for 1 minute to ensure a good dispersion of the nanoparticles, then the organic cells were made by applying the protocol described above including the use of the 1,8-diiodooctane. For comparison, some devices were manufactured using pristine PEDOT:PSS and a dispersion obtained adding 100 μL of ultrapure water to 1 mL of the PEDOT:PSS.

The results summarized in table 4.2 show that the samples made with modified PEDOT:PSS have lower performances than those with pristine PEDOT:PSS, however, the presence of nanoparticles leads to devices with better performances than those with ultrapure water only.

Table 4.2 Summary of the average photovoltaic parameters of the devices. Each value represents the average of 12 replicates.

Device	Description	FF	V_{oc} (V)	$-J_{sc}$ (mA/cm^2)	PCE (%)
B_{REF}	PEDOT:PSS	0.55 ± 0.01	0.59 ± 0.01	7.71 ± 0.21	2.51 ± 0.09
B1	1mL PEDOT:PSS + 100 μL H ₂ O	0.46 ± 0.02	0.59 ± 0.01	7.39 ± 0.33	2.00 ± 0.14
B2	1mL PEDOT:PSS + 100 μL Au@PVP	0.54 ± 0.04	0.59 ± 0.01	6.81 ± 0.24	2.18 ± 0.32

Water addition to PEDOT:PSS dispersion changes its rheological properties and therefore heavily influences the film formation. Obviously, the dilute PEDOT:PSS leads to the formation of a thinner film respect to the pristine PEDOT:PSS. Furthermore, the dilution could causes a variation of the PEDOT:PSS energy levels^[7]. Both these effects can explain the worsening of performances in devices fabricated with PEDOT:PSS in which water was added. To limit these unwanted effects, the dispersion of Au@PVP nanoparticles was concentrated before its addition to the PEDOT:PSS, in order to reduce its water content. 100 μL of the Au@PVP dispersion were centrifuged at 14000 rpm for 15 minutes, the supernatant was removed and replaced with 1 mL of PEDOT:PSS. To avoid the aggregation of the nanoparticles a minimal volume of supernatant, 15 μL , were left in contact with them before the addition of the PEDOT:PSS. Solar devices were fabricated following the procedure previously described and in table 4.3 are reported the results of the electrical characterizations.

Table 4.3 Summary of the average photovoltaic parameters of the devices. Each value represents the average of 12 replicates.

Device	Description	FF	V_{oc} (V)	$-J_{sc}$ (mA/cm ²)	PCE (%)
K_{REF}	PEDOT:PSS	0.58 ± 0.01	0.59 ± 0.01	7.48 ± 0.24	2.56 ± 0.10
K2	1mL PEDOT:PSS + 15 μ L H ₂ O	0.55 ± 0.02	0.59 ± 0.01	7.39 ± 0.22	2.40 ± 0.12
K3	1mL PEDOT:PSS + Au@PVP concentrated	0.59 ± 0.01	0.59 ± 0.01	7.52 ± 0.25	2.62 ± 0.09

The results confirm that the water added to the PEDOT:PSS has a significant effect on the performance of the solar cells. In particular, with respect to the previous set of devices, it can be observed that by reducing the amount of water added to the PEDOT:PSS the worsening of the efficiency of the solar cells is lower. In addition, in the case of the plasmonic devices a slightly improvement of the performances is observed with respect to the reference.

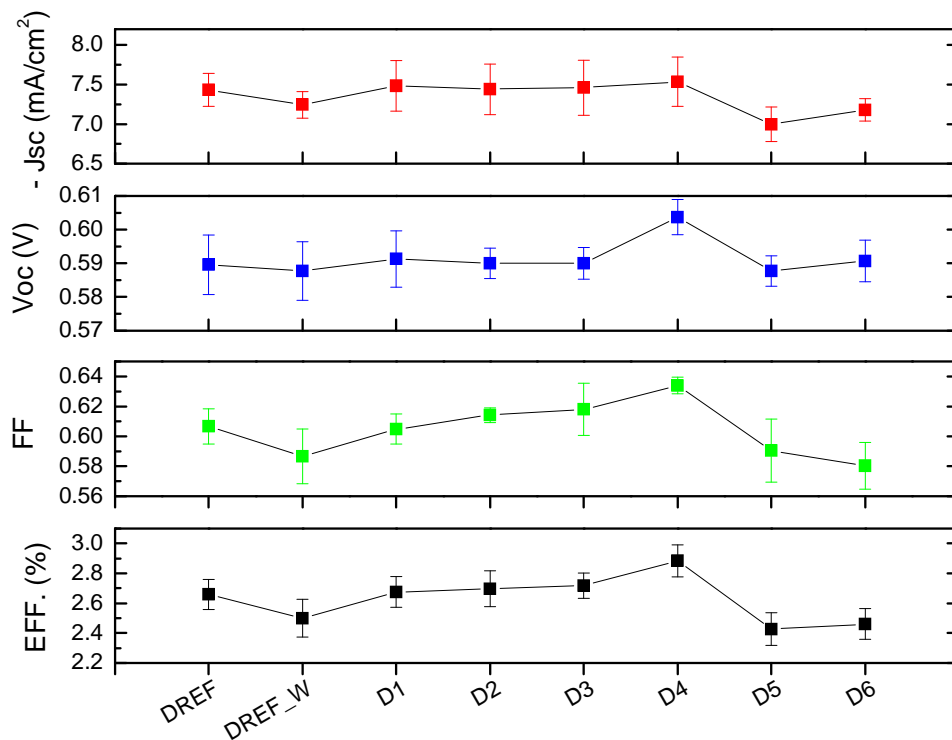
4.4 Effect of Au@PVP nanoparticles concentration in PEDOT:PSS on the performance of the devices

To investigate the effects that nanoparticles incorporated in PEDOT:PSS produce in the solar cells and how they depend on the nanoparticle concentration, a series of solar cells was made by varying the amount of nanoparticles added to PEDOT:PSS. In particular, Au@PVP dispersions in PEDOT:PSS were prepared using the procedure described above with the following concentrations: $C_1 = 5.78 \times 10^9$ particles/mL; $C_2 = 2.89 \times 10^{10}$ particles/mL; $C_3 = 1.45 \times 10^{11}$ particles/mL; $C_4 = 5.78 \times 10^{11}$ particles/mL; $C_5 = 1.16 \times 10^{12}$ particles/mL; $C_6 = 2.31 \times 10^{12}$ particles/mL. As a reference, samples using pristine PEDOT:PSS and PEDOT:PSS with water (15 μ L of H₂O added to 1 mL of PEDOT:PSS) were prepared. Table 4.4 and figure 4.6 summarize the results of the electrical characterization of the fabricated devices.

It can be observed that with the increase of the concentration of the Au@PVP nanoparticles in PEDOT:PSS, the efficiency of the devices growth up to a maximum average value of 2.88 % (in the case of D4 devices).

Table 4.4 Summary of the average photovoltaic parameters of the devices. Each value represents the average of 8 replicates.

Device	Description	FF	V _{oc} (V)	-J _{sc} (mA/cm ²)	PCE (%)
D _{REF}	PEDOT:PSS (ref)	0.61 ± 0.01	0.59 ± 0.01	7.43 ± 0.21	2.66 ± 0.10
D _{REF_W}	PEDOT:PSS + H ₂ O (ref_w)	0.59 ± 0.02	0.59 ± 0.01	7.24 ± 0.17	2.50 ± 0.13
D1	PEDOT:PSS + Au@PVP (C ₁)	0.60 ± 0.01	0.59 ± 0.01	7.48 ± 0.32	2.68 ± 0.10
D2	PEDOT:PSS + Au@PVP (C ₂)	0.61 ± 0.01	0.59 ± 0.01	7.44 ± 0.32	2.70 ± 0.12
D3	PEDOT:PSS + Au@PVP (C ₃)	0.62 ± 0.02	0.59 ± 0.01	7.46 ± 0.35	2.72 ± 0.08
D4	PEDOT:PSS + Au@PVP (C ₄)	0.63 ± 0.02	0.60 ± 0.01	7.54 ± 0.31	2.88 ± 0.11
D5	PEDOT:PSS + Au@PVP (C ₅)	0.59 ± 0.02	0.59 ± 0.01	7.00 ± 0.22	2.43 ± 0.11
D6	PEDOT:PSS + Au@PVP (C ₆)	0.58 ± 0.02	0.59 ± 0.01	7.18 ± 0.14	2.46 ± 0.10

**Figure 4.6** Summary of the average photovoltaic parameters of the devices. The error bars represent the standard deviation on 8 replicates.

However, at higher concentrations the performances of the solar cells are significantly lower than the references. J_{SC} and FF are the two parameters mainly affected by the presence of nanoparticles, while V_{OC} is almost unchanged for all the different concentration with the exception of the C_4 value, in which case is slightly higher.

The light trapping enhancement resulting from the incorporation of plasmonic nanoparticles in the PEDOT:PSS can involve effects of light scattering or near-field enhancement. The first lead to an increase of the light path inside the active layer and so the probability of absorption is enhanced, while the latter produces an increase of the absorption as a consequence of the larger cross section of the region of active layer affected by the local field^[8]. To determinate experimentally these contributes, UV-Visible spectroscopy measurements were achieved on samples with the structure glass/ITO/PEDOT:PSS with Au@PVP nanoparticles at different concentrations. Two other samples, as references, were prepared using pristine PEDOT:PSS and PEDOT:PSS with 15 μ L of ultrapure water. All samples, to be representative of the corresponding devices, were prepared in the same time and conditions of the solar cells.

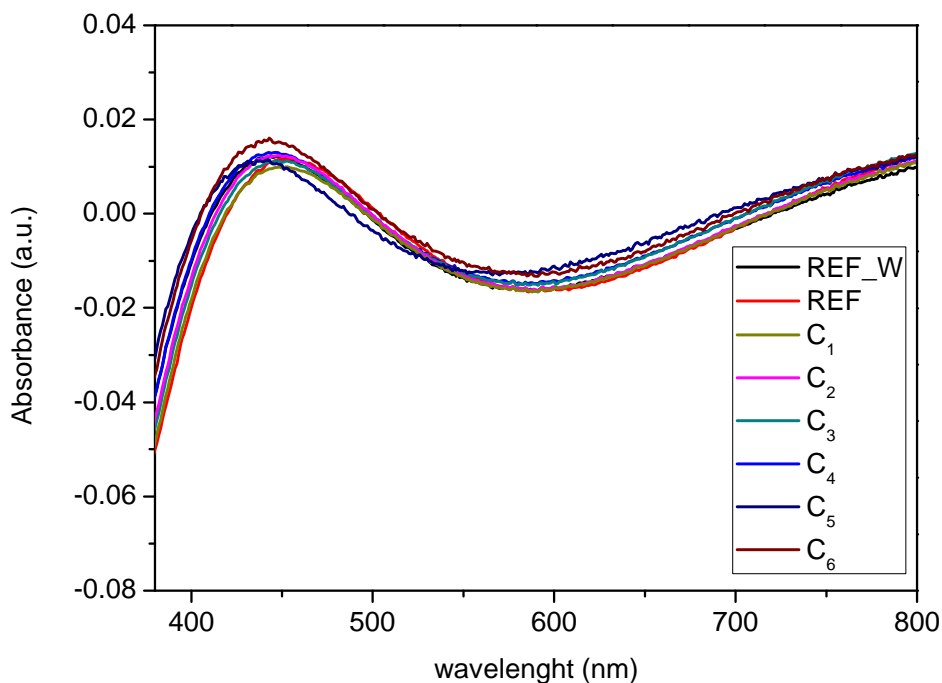


Figure 4.7 Absorption spectra of the sample glass/ITO/PEDOT:PSS with or without Au@PVP nanoparticles at different concentration as reported in table 4.4 (baseline: glass/ITO).

From figure 4.7 it can be deduced that there are no significant differences in the intensity of the spectra at the various concentrations of nanoparticles, therefore a contribution of forward light scattering or intrinsic nanoparticle absorption is low. The same characterizations were performed after the deposition of the active layer on the samples and the results are showed in figure 4.8. An absorption enhancement with the concentration of the nanoparticles in the PEDOT:PSS as effect of the near-field enhancement is clearly observable.

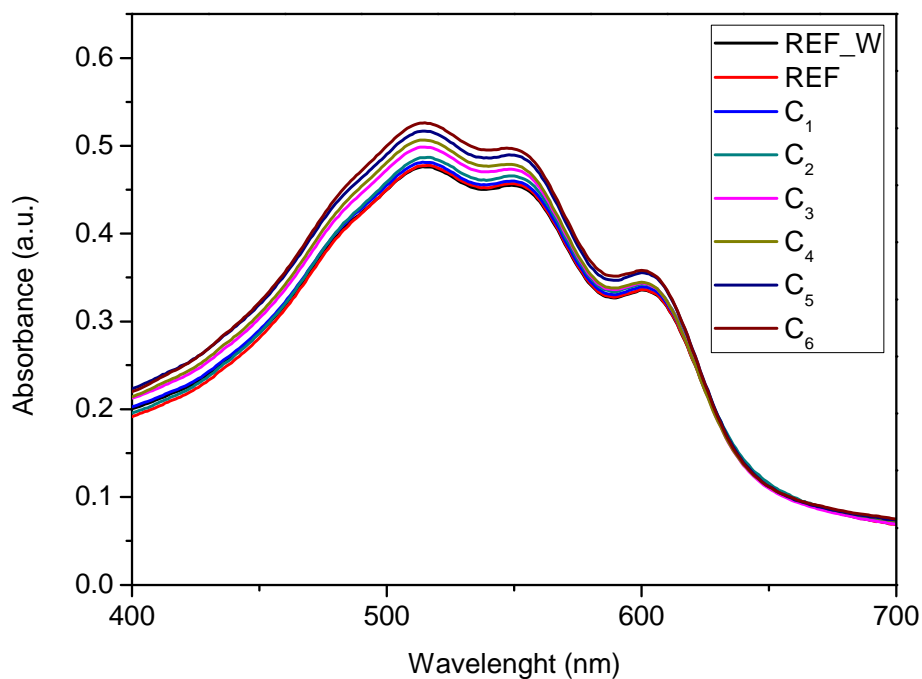
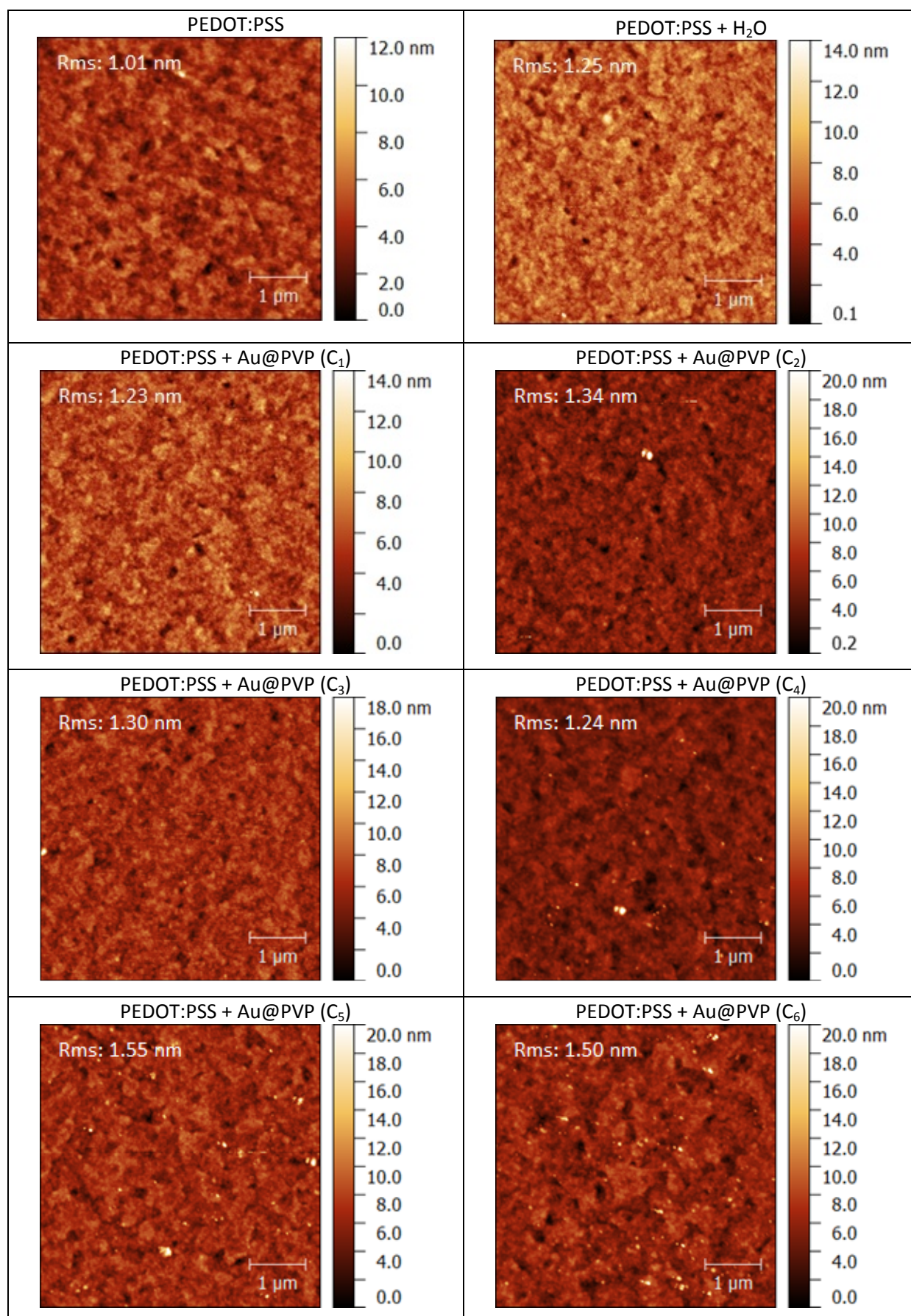


Figure 4.8 Absorption spectra of the samples glass/ITO/PEDOT:PSS with or without Au@PVP nanoparticles/P3HT:PC₆₁BM (baseline: glass/ITO).

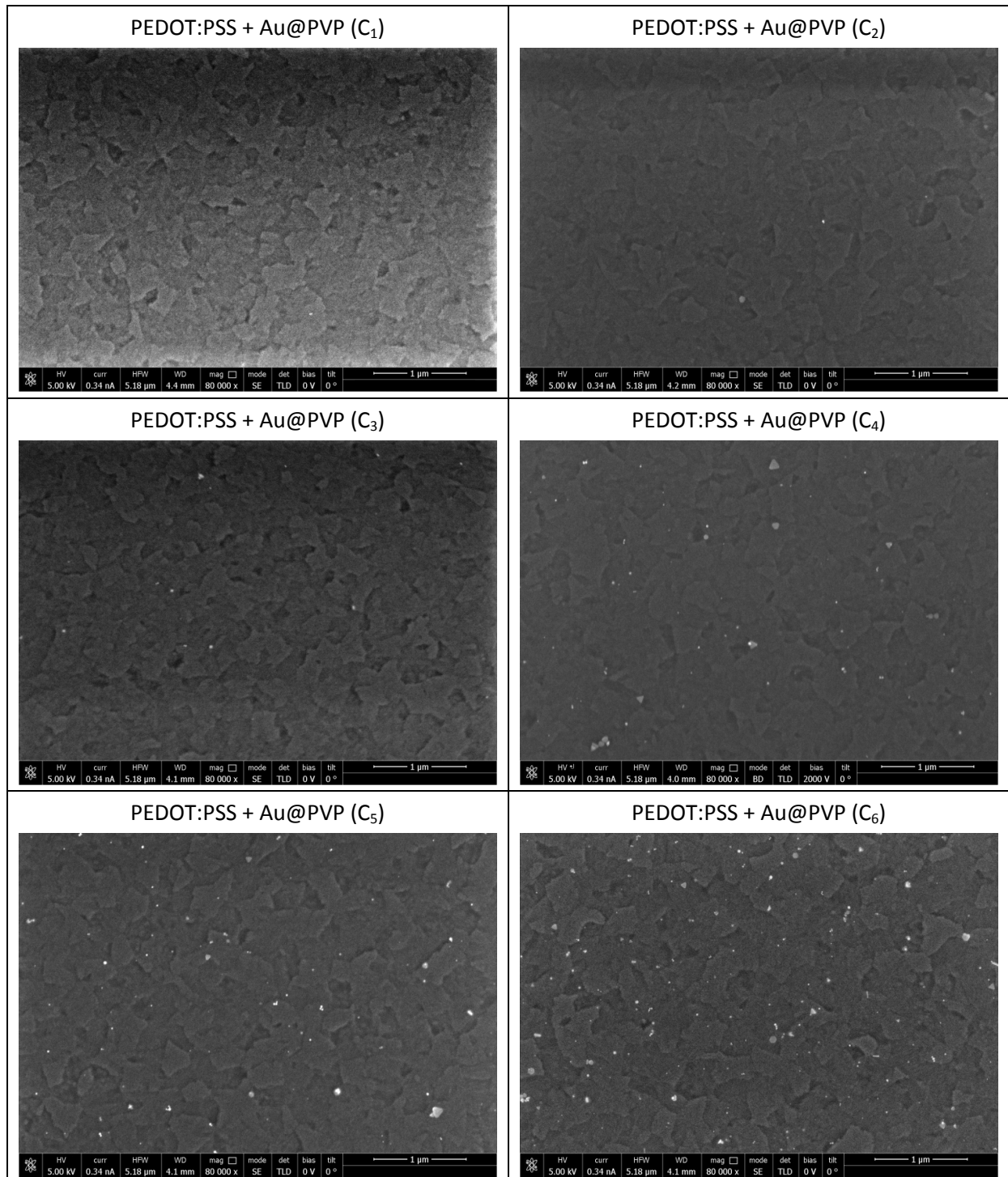
The surface morphology of the PEDOT:PSS thin films doped with various concentrations of Au@PVP nanoparticles was investigated by AFM and the topographic images acquired are reported in table 4.5. Root Mean Square roughness (RMS) values, obtained directly from the images using the AFM software Gwyddion, are also shown in the same table. Generally, the presence of the nanoparticles in PEDOT:PSS produces an enhancement in the surface roughness of the film. This leads to the increase of the contact area between PEDOT:PSS and the active layer, whereby the hole collection efficiency and consequently the J_{SC} of the devices improve^[9,10].

Table 4.5 AFM topographic images (5 μm \times 5 μm) of PEDOT:PSS thin films, with different concentration of Au@PVP nanoparticles, spin-coated on glass/ITO substrates.

Moreover, as a consequence of the reduced mean distance between the generated holes and the PEDOT:PSS interface, the dependence of the collection of the holes from the external electric field decrease, resulting in a FF enhancement^[10]. However, when the concentration of the nanoparticles is higher than the optimal value, they could protrude into the active layer film modifying its nanoscale morphology and reducing the P3HT/PC₆₁BM interfacial area. Therefore, the exciton dissociation is disadvantaged and the J_{SC} of the devices decreases.

To investigate the distribution of the nanoparticles in the PEDOT:PSS film, samples with the structure glass/ITO/PEDOT:PSS with Au@PVP nanoparticles at different concentration were analyzed by scanning electron microscopy (SEM) and the micrographs are showed in table 4.6. It can be observed that the nanoparticles are well dispersed in the PEDOT:PSS and there are no evident aggregates also at the higher concentration thanks to the efficient PVP stabilization.

Table 4.6 SEM images of PEDOT:PSS thin films, with different concentration of Au@PVP nanoparticles, spin-coated on glass/ITO substrates.



4.5 Incorporation of Au@PVP and Au@SiO₂ nanoparticles at PEDOT:PSS/P3HT:PC₆₁BM interface

The strategy of nanoparticles integration at the interface between the PEDOT:PSS and the active layer is to fully exploit the near-field of the nanoparticles considering that it decays near-exponentially with the distance from the metallic surface. In order to optimize the deposition of Au@PVP nanoparticles on the hole transport layer, a preliminary assessment of the effects of solvent treatment of PEDOT:PSS on the solar cell performances was necessary. In particular, solar cells based on water-treated PEDOT:PSS and ethanol-treated PEDOT:PSS were fabricated and tested. The procedure followed was the one reported above with the further step of the PEDOT:PSS film treatment. Practically, before active layer deposition, 80 μ L of solvent was spin coated on the PEDOT:PSS film at 1200 rpm for 1 minute and then the film was annealed in air for 15 minutes at 140 °C. To rule out the possibility that the additional annealing could affect the PEDOT:PSS, reference samples were prepared with PEDOT:PSS film subjected to the same thermal treatment. Table 4.7 summarizes the results of the electrical characterization of the samples.

Table 4.7 Summary of the average photovoltaic parameters of the devices. Each value represents the average of 12 replicates.

Device	Description	FF	V _{oc} (V)	-J _{sc} (mA/cm ²)	PCE (%)
E1	Pristine PEDOT:PSS	0.58 ± 0.01	0.59 ± 0.01	7.40 ± 0.33	2.53 ± 0.09
E2	Ethanol-treated PEDOT:PSS	0.57 ± 0.01	0.59 ± 0.01	7.46 ± 0.33	2.51 ± 0.08
E3	Water-treated PEDOT:PSS	0.51 ± 0.01	0.58 ± 0.01	7.57 ± 0.32	2.24 ± 0.10

As can be seen, ethanol treatment of the PEDOT:PSS produce no effect on the solar cell performances, while water has a negative impact on the FF. An in-deep investigation into the effects of water and ethanol spin coating on PEDOT:PSS films has been reported in literature^[11]. The authors demonstrated by UV-Visible spectroscopy, X-Ray photoelectron spectroscopy and contact angle measurements that the solvent treatment removes the surface layers of PSS and that water has a more pronounced effect than ethanol. In addition, they determined an enhancement of the film conductivity after the treatment (as a

consequence of the removal of the insulating PSS) and an increase of the surface roughness by AFM measurements.

The solvent treatment conditions used by the authors in their work are different from those used in this work. In particular, they spin coated the solvents on PEDOT:PSS film at 3000 rpm for 1 minute. Under those conditions, a greater amount of solvent is removed from the surface in the first seconds after the start of the spin coating and at the same time the evaporation is faster with respect to the process accomplished in the present work (spin coating of the solvent at 1200 rpm for 1 minute). As a consequence, the interaction time between the solvent and the film in this work is greater and it is possible that the solvent, in particular water, could lead to PEDOT:PSS film degeneration or affect the adhesion to the substrate, resulting in a worsening of the solar cells performance.

Considering the results of the preliminary study of the effect of the solvents on the PEDOT:PSS, a dispersion of Au@PVP nanoparticles in ethanol (obtained using 90 μL of H_2O_2 during the growth step) for their deposition on PEDOT: PSS was chosen. A set of solar devices was prepared following the protocol described above with the further step of the nanoparticles deposition before the spin coating of the active layer. For the deposition of the nanoparticles, 80 μL of their dispersion were spin coated on the PEDOT:PSS film at 1200 rpm for 1 minute and then the film was annealed in air for 15 minutes at 140 $^\circ\text{C}$. Samples were prepared using three different concentrations of Au@PVP nanoparticles in ethanol, $C_1=2.35 \times 10^{11}$ particles/mL; $C_2= 7.8 \times 10^{11}$ particles/mL; $C_3=5.88 \times 10^{11}$ particles/mL and, as a reference, samples with ethanol-treated PEDOT:PSS were fabricated and tested.

Table 4.8 Summary of the average photovoltaic parameters of the devices. Each value represents the average of 12 replicates.

Device	Description	FF	V_{oc} (V)	$-J_{sc}$ (mA/cm^2)	PCE (%)
F_{REF}	PEDOT:PSS + Ethanol	0.58 ± 0.01	0.59 ± 0.01	7.51 ± 0.23	2.57 ± 0.11
F1	PEDOT:PSS + Au@PVP (C_1)	0.29 ± 0.02	0.36 ± 0.02	4.81 ± 0.60	0.51 ± 0.08
F2	PEDOT:PSS + Au@PVP (C_2)	0.30 ± 0.01	0.43 ± 0.03	4.61 ± 0.44	0.59 ± 0.10
F3	PEDOT:PSS + Au@PVP (C_3)	0.27 ± 0.03	0.38 ± 0.07	4.44 ± 0.42	0.45 ± 0.08

Table 4.8 reports the principal photovoltaic parameters for the samples prepared. In figure 4.9 some representative characteristic curves of the samples are showed.

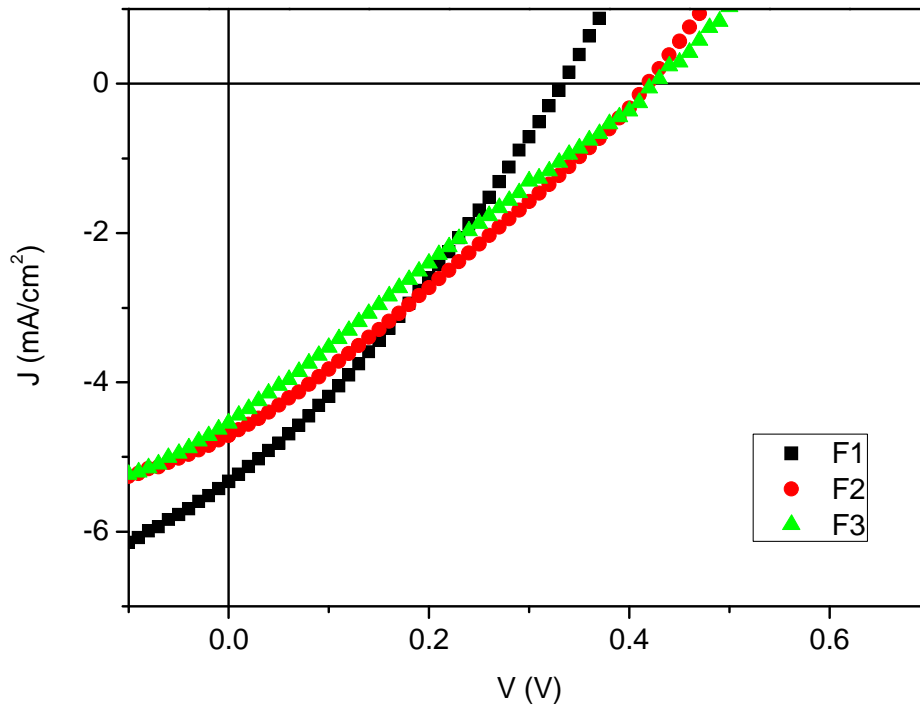


Figure 4.9 Representative J-V curves of the devices F1, F2 and F3.

The integration of the Au@PVP nanoparticles at the PEDOT:PSS/P3HT:PC₆₁BM interface causes a significant deterioration of the cell performances. This could be due to the fact that PVP around the metallic surface is not thick enough to electrically insulate the nanoparticles, whereby charge recombination and exciton quenching can occur due to dipole-dipole and charge-trapping coupling^[12]. It was therefore necessary to develop a protocol to cover the Au@PVP with an insulating silica shell, as detailed described in Chapter 3. The silica shell must be thick enough to insulate the metallic core but at the same time as thin as possible because the near-field is lost in it. On the basis of this consideration, it was decided to manufacture solar cells with nanoparticles incorporated at the HTL/active layer interface as soon as a complete coating of the nanoparticles with an average thickness of the silica shell of about 3 nm was obtained (refer to paragraph 3.3.2). Samples were prepared using three different concentrated Au@SiO₂ dispersions in ethanol, C₁=2.35 x 10¹¹ particles/mL; C₂= 7.8 x 10¹¹ particles/mL; C₃=5.88 x 10¹¹ particles/mL. The devices were electrically characterized

and the results are showed in table 4.9. In figure 4.10 some representative characteristic curves of the samples are showed.

Table 4.9 Summary of the average photovoltaic parameters of the devices. Each value represents the average of 12 replicates.

Device	Description	FF	V_{oc} (V)	$-J_{sc}$ (mA/cm ²)	PCE (%)
G_{REF}	PEDOT:PSS + Ethanol	0.57 ± 0.01	0.59 ± 0.01	7.46 ± 0.33	2.51 ± 0.08
G1	PEDOT:PSS + Au@SiO ₂ (C ₁)	0.22 ± 0.02	0.51 ± 0.04	4.85 ± 0.37	0.56 ± 0.08
G2	PEDOT:PSS + Au@SiO ₂ (C ₂)	0.30 ± 0.03	0.55 ± 0.04	5.48 ± 0.11	0.91 ± 0.14
G3	PEDOT:PSS + Au@SiO ₂ (C ₃)	0.37 ± 0.06	0.52 ± 0.10	5.7 ± 0.11	1.07 ± 0.11

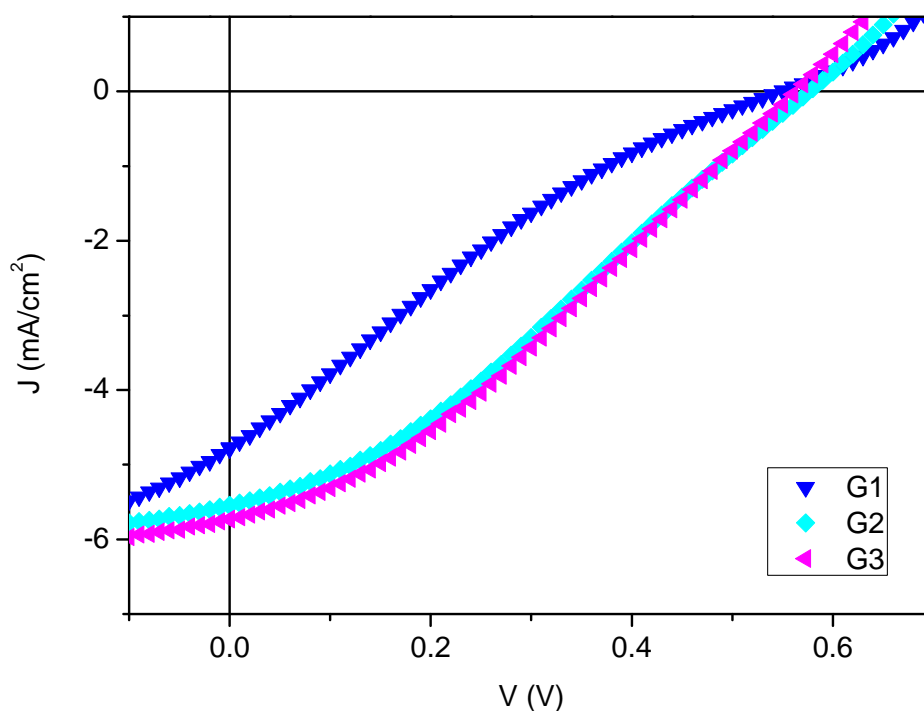


Figure 4.10 Representative J-V curves of the devices G1, G2 and G3.

As can be seen, the integration of the nanoparticles at the interface results in devices whose characteristic curves exhibit the S-shaped anomaly. However, the magnitude of the phenomenon decrease by increasing the dilution of the ethanolic nanoparticle dispersion

deposited above the HTL. The problem could be related to the nanoparticles, which were not completely isolated due to the reduced thickness of the silica shell, but also to the medium in which they were dispersed. TEM observations permitted to exclude the presence of reaction residuals in the Au@SiO₂ nanoparticles dispersions, confirming the efficacy of the purification procedure used. However it was thought to investigate if the centrifugal concentrator used for nanoparticle purification could release undesired substances not observable to TEM. Therefore, some devices were produced by depositing ethanol, which was previously poured in a centrifugal concentrator and subject to the same centrifugation process used for nanoparticles purification, on PEDOT:PSS. As reference, samples with pure ethanol were fabricated. In figure 4.11 are reported some representative characteristic curves of the sample with ethanol and pretreated ethanol.

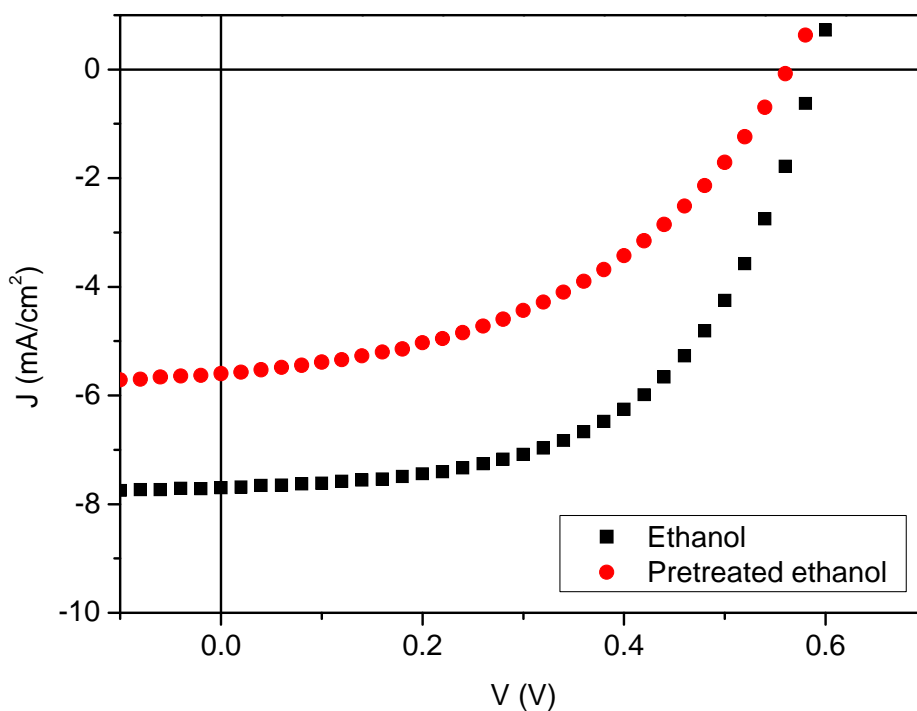


Figure 4.11 Representative J-V curves of the devices with ethanol and pretreated ethanol spin coated on PEDOT:PSS.

Although the devices fabricated using pretreated ethanol did not show the problem of the S-shaped in the characteristic curves, they had notably lower performances respect to the references. It could be deduced, therefore, that the S-shaped problem was ascribed to the insufficient electrical insulation of the nanoparticles. On the other hand, the worsening of the performance of the devices fabricated with pretreated ethanol, could be related to use

of the centrifugal tube made of polycarbonate. This material in contact with ethanol could release bisphenol^[13] that deposited at the interface produces the deterioration of the cell performances. Considering these experimental evidences, it was necessary to interrupt the study of the incorporation of the nanoparticle in the solar cells. The experimental work was therefore finalized to obtain Au@SiO₂ nanoparticles with the appropriate silica shell thickness through synthetic and purification procedures fully compatible with the use ethanol, as described in detail in Chapter 3.

4.6 References

- [1] Y. H. Huh et al., Investigating the origin of S-shaped photocurrent-voltage characteristics of polymer:fullerene bulk-heterojunction organic solar cells. *Journal of Applied Physics*, **2014**, 115, 124504.
- [2] B. Tremolet de Villers et al., Improving the reproducibility of P3HT: PCBM solar cells by controlling the PCBM/cathode interface. *The Journal of Physical Chemistry C*, **2009**, 113, 18978-18982.
- [3] H. C. Wong et al., Morphological stability and performance of polymer-fullerene solar cells under thermal stress: the impact of photoinduced PC₆₀BM oligomerization. *ACS Nano*, **2014**, 8, 1297-1308.
- [4] L. Chang et al., Effect of trace solvent on the morphology of P3HT: PCBM bulk heterojunction solar cells. *Advanced Functional Materials*, **2011**, 21, 1779-1787.
- [5] S. Kwon et al., Effect of processing additives on organic photovoltaics: Recent progress and future prospects. *Advanced Energy Materials*, **2017**, 7, 1601496.
- [6] J. K. Lee et al., Processing additives for improved efficiency from bulk heterojunction solar cells. *Journal of the American Chemical Society*, **2008**, 130, 3619-3623.
- [7] C. Wang et al., Energy level and thickness control on PEDOT:PSS layer for efficient planar heterojunction perovskite cells. *Journal of Physics D: Applied Physics*, **2017**, 51, 025110.
- [8] Y.-S. Hsiao et al., Improving the light trapping efficiency of plasmonic polymer solar cells through photon management. *The Journal of Physical Chemistry C*, **2012**, 116, 20731-20737.
- [9] M. H. Hsu et al., Balanced carrier transport in organic solar cells employing embedded indium-tin-oxide nanoelectrodes. *Applied Physics Letters*, **2011**, 98, 37.
- [10] D. D. S. Fung et al., Optical and electrical properties of efficiency enhanced polymer solar cells with Au nanoparticles in a PEDOT–PSS layer. *Journal of Materials Chemistry*, **2011**, 21, 16349-16356.
- [11] X. Y. Li et al., The solvent treatment effect of the PEDOT: PSS anode interlayer in inverted planar perovskite solar cells. *RSC Advances*, **2016**, 6, 24501-24507.
- [12] J. Wang et al., Design principles for nanoparticle plasmon-enhanced organic solar cells. *Nanoscale Research Letters*, **2018**, 13, 211.
- [13] E. J. Hoekstra et al., Release of bisphenol A from polycarbonate—a review. *Critical reviews in food science and nutrition*, **2013**, 53, 386-402.

Chapter 5

Plasmonic perovskite solar cells

5.1 Introduction

This chapter reports the experimental work concerning the integration of plasmonic anisotropic gold nanoparticles in perovskite solar cells. The aim was to study the effects produced by these nanoparticles on devices based on photoactive materials whose photogeneration and charge transport mechanisms are different with respect to organic semiconductors.

Perovskite solar cells are one of the most promising photovoltaic technologies because of their excellent photovoltaic performances, low cost and compatibility with large scale roll-to-roll production. The presence of toxic lead in perovskite is, besides their stability, one of the main limiting factors towards the commercialization of solar devices based on these materials. The integration of plasmonic nanoparticles could allow to reduce the thickness of the active layer of the devices and in turns the lead content without decreasing their efficiency. Furthermore, the use of metallic nanoparticles could permit to obtain high efficient semi-transparent perovskite solar cells that can be applied as Building Integrated Photovoltaics or integrated into tandem devices.

An inverted planar device architecture was chosen as a reference cell because its fabrication is compatible with low temperature solution processes required for the integration of the nanoparticles. Since the PEDOT:PSS can be used to make the HTL of this architecture, it was possible to exploit the experience acquired previously regarding the integration of nanoparticles in organic solar cells. On the other hand, as reported in chapter 3, the versatile method for the synthesis of the nanoparticles has allowed to adapt their optical and morphological properties to the perovskite-based devices.

A cell structure glass/ITO/PEDOT:PSS/CH₃NH₃PbI_{3-x}Br_x/PC₆₁BM/BCP/Al was chosen as a reference, because its fabrication, previously optimized, was highly reproducible allowing to highlight the effects produced by the nanoparticles. Although Au@PVP nanoparticles were introduced at different concentrations in the PEDOT:PSS, no beneficial effects were observed. It was not possible to investigate the effects of the nanoparticles in similar cells

with a reduced active layer thickness because of the lack of reproducibility of the devices due to the low perovskite film quality. Therefore, since the perovskite film growth depends, among others, on the substrate, the PEDOT:PSS was replaced with Poly[*N,N'*-bis(4-butylphenyl)-*N,N'*-bis(phenyl)-benzidine] (poly-TPD). In this way, it was possible to optimize the fabrication of a new reference perovskite solar device and to investigate the effects of plasmonic nanoparticles integrated in this cell. Due to the solvent incompatibility with the PVP-stabilized nanoparticles, it was possible to fabricate devices in which the nanoparticles were only deposited on the poly-TPD film and not within it.

The development of inverted perovskite based solar cells has been performed in Lecce at the Device Lab of the Nanotechnology Institute of CNR, because the people working there has a huge experience in that field since they have developed perovskite based devices for many years.

5.2 Plasmonic perovskite solar cells integrating anisotropic Au@PVP nanoparticles in PEDOT:PSS

5.2.1 Device fabrication

ITO-coated glass substrates 4L etched (sheet resistivity 12 Ω /sq, Visiontech) were sequentially cleaned by ultrasonication in deionized water, 2-propanol and acetone for 10 minutes. Substrates were immersed in a mixture of hydrogen peroxide (H_2O_2), ammonia (NH_3) and ultrapure water (1:1:5 v/v) at 80°C for 10 minutes in order to remove organic contamination, then rinsed ten times in water prior next depositions.

To prepare anisotropic gold nanoparticle dispersions in PEDOT:PSS (1:6 weight ratio, suspension in water, solid content 1.3 - 1.7 % w/V, Heraeus Clevis PVP Al 4083, H.C. Starck), 0.5 mL, 1 mL and 2 mL of an aqueous dispersion of Au@PVP nanoparticles were concentrated by centrifugation (as reported in paragraph 4.3) and each one was added respectively to 1 mL of PEDOT:PSS previously filtered by using a 0.45 μm PVDF syringe filter. After homogenization by a vortex mixer, the dispersions were deposited by spin coating at 3000 rpm for 60 s and the substrates were annealed at 140 °C for 15 minutes. By adopting the same deposition and thermal treatment conditions a reference sample was prepared with a pristine PEDOT:PSS dispersion.

All samples were transferred to a nitrogen filled glovebox to complete the device fabrications.

A perovskite precursor solution 30 wt% was previously prepared by dissolving 461 mg of lead iodide (PbI_2 , ultra dry, 99.999% metals basis, Alfa Aesar) and 159 mg of methylammonium iodide ($\text{CH}_3\text{NH}_3\text{I}$, >99%, dyesol) in 1.4 mL of a 2:1 v/v mixture of γ -butyrolactone (GBL, >99%, Sigma Aldrich) and dimethyl sulfoxide (DMSO, 99.8%, Sigma-Aldrich) and stirring for 12 h.

The solution was spin coated onto PEDOT:PSS film by a consecutive two-step process at 1000 rpm and 4000 rpm for 20 s and 60 s, respectively, with a dripping of dichlorometane ($\geq 99.8\%$, Sigma-Aldrich) 15 s before the end of the deposition. The samples were annealed at 100 °C for 10 minutes and then allowed to cool to room temperature.

A solution previously prepared dissolving 25 mg of PC_{61}BM (Nano-C) in 1 mL of chlorobenzene (CB, 99.8%, Sigma Aldrich), was spin-coated on the perovskite layer at 1000 rpm for 60 s. Then, 5 nm of bathocuproine (BCP, LT-E304 Lumtec) and 100 nm of aluminum

(Al pellets, 99.999%, Lesker) were thermally evaporated at a pressure of 5×10^{-6} mbar to form the back contact of the devices. Finally, the devices were characterized under an irradiance of 1000 W/m^2 at air mass (AM) 1.5G. Acquiring the J-V curves from positive to negative voltage (reverse scan) and from negative to positive voltage (forward scan), for all the samples no hysteresis was observed. Therefore, only the J-V curves recorded in reverse scan are shown below.

5.2.2 Characterization and results

Plasmonic devices were prepared using Au@PVP nanoparticles synthesized adding $45 \mu\text{L}$ of H_2O_2 during their growth step.

The absorption spectrum of the purified aqueous dispersion and the TEM micrograph of the nanoparticles are showed in figure 5.1 and figure 5.2, respectively. The calculated concentration was 5.9×10^{11} particles/mL.

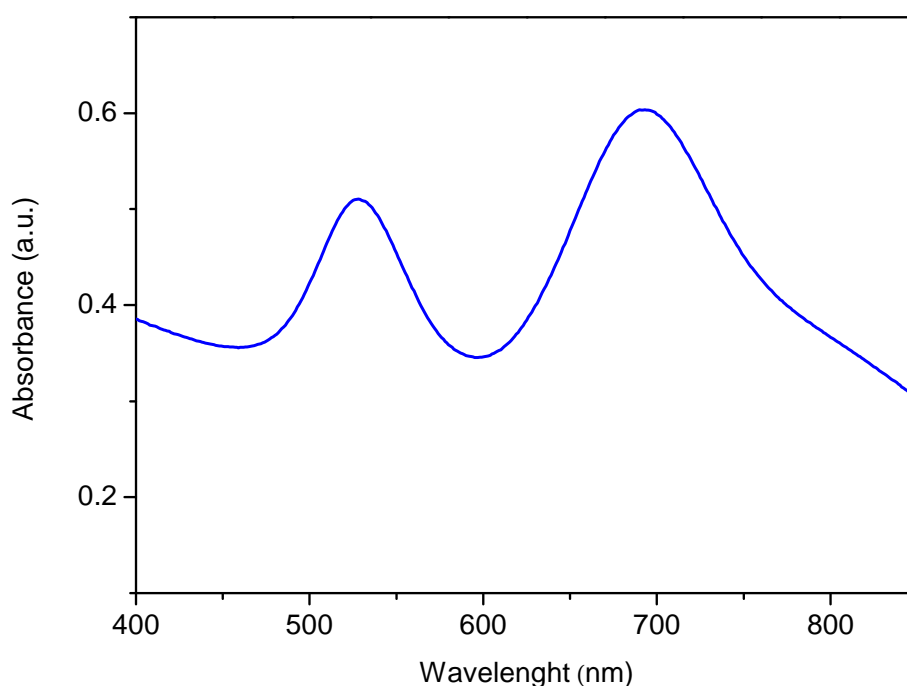


Figure 5.1 Absorption spectrum of Au@PVP nanoparticles dispersion prepared by adding $45 \mu\text{L}$ of H_2O_2 during the synthesis.

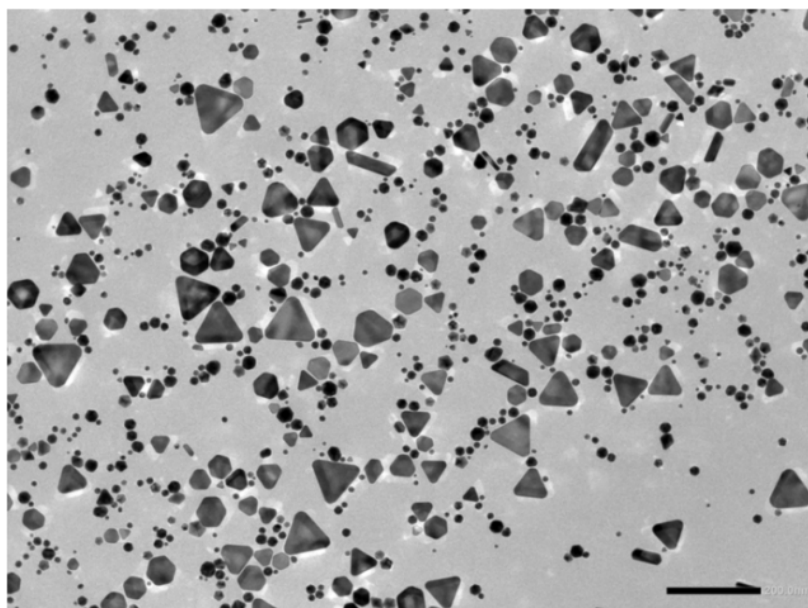


Figure 5.2 TEM micrograph of the Au@PVP nanoparticles prepared by adding 45 μL of H_2O_2 during the synthesis (scale bar correspond to 200 nm).

Table 5.1 summarizes the principal figures of merit of the devices with different concentrations of Au@PVP nanoparticles in PEDOT:PSS, while figure 5.3 reports the reverse current density versus voltage scans of the samples.

The concentrations of the Au@PVP nanoparticles in PEDOT:PSS are indicated as $C_0 = 0$ nanoparticles/mL; $C_1 = 2.95 \times 10^{11}$ nanoparticles/mL; $C_2 = 5.90 \times 10^{11}$ nanoparticles/mL; $C_3 = 1.18 \times 10^{12}$ nanoparticles/mL.

Table 5.1 Summary of the average photovoltaic parameters of the devices glass/ITO/PEDOT:PSS/ $\text{CH}_3\text{NH}_3\text{PbI}_3$ /PC₆₁BM/BCP/Al with different concentrations of Au@PVP nanoparticles in PEDOT:PSS. Each value represents the average of 8 replicates.

Device	Description	FF	V_{oc} (V)	$-J_{sc}$ (mA/cm^2)	PCE (%)
H_{REF}	PEDOT:PSS + Au@PVP (C_0)	0.81 ± 0.03	0.81 ± 0.02	13.95 ± 0.38	9.17 ± 0.48
H1	PEDOT:PSS + Au@PVP (C_1)	0.82 ± 0.04	0.81 ± 0.03	13.28 ± 0.34	8.80 ± 0.39
H2	PEDOT:PSS + Au@PVP (C_2)	0.82 ± 0.04	0.79 ± 0.02	13.22 ± 0.37	8.61 ± 0.44
H3	PEDOT:PSS + Au@PVP (C_3)	0.80 ± 0.03	0.80 ± 0.03	12.10 ± 0.41	7.74 ± 0.46

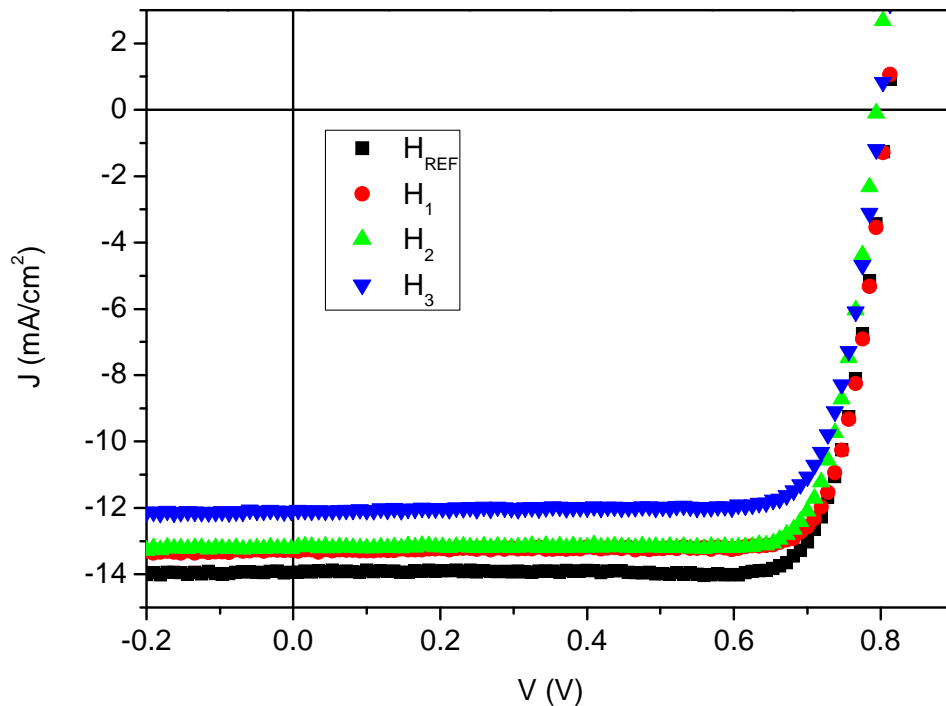


Figure 5.3 Representative J-V curves of the devices glass/ITO/PEDOT:PSS/CH₃NH₃PbI₃/PC₆₁BM/BCP/Al with different concentrations of Au@PVP nanoparticles in PEDOT:PSS.

It can be observed that the incorporation of the nanoparticles produces a reduction of the performance of the cells, especially in terms of J_{SC} whose value decreases with increasing the concentration of nanoparticles. The V_{OC} is not influenced by the presence of the nanoparticles in the PEDOT:PSS, while the FF is slightly greater in plasmonic devices C_1 e C_2 , but at higher nanoparticle concentration its value decreases.

To investigate the optical effects on the cells deriving from the incorporation of the nanoparticles in the PEDOT:PSS layer, absorption spectra of samples glass/ITO/PEDOT:PSS + Au@PVP nanoparticles and samples glass/ITO/PEDOT:PSS + Au@PVP nanoparticles/CH₃NH₃PbI₃, prepared in the same conditions of the corresponding complete devices, were acquired (using glass/ITO as baseline). From figure 5.4, relative to the samples glass/ITO/PEDOT:PSS + Au@PVP nanoparticles, it can be deduced that there are no significant differences in the intensity of the spectra at the different concentrations with respect to the reference, therefore the contribution of light scattering or the intrinsic absorption of nanoparticles is negligible.

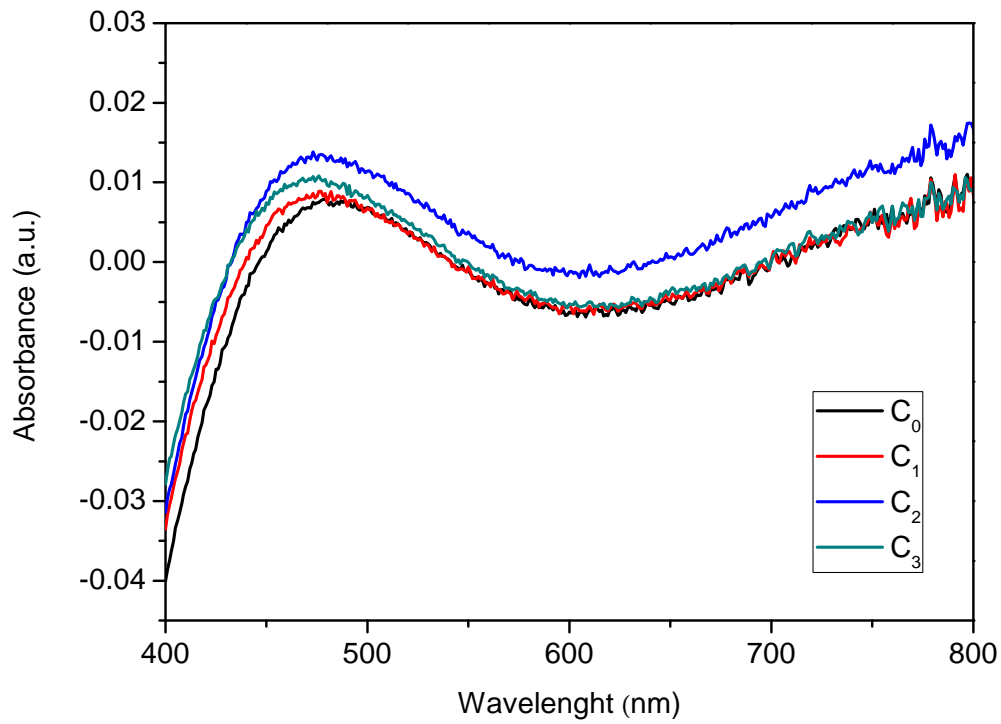


Figure 5.4 Absorption spectra of samples glass/ITO/PEDOT:PSS + Au@PVP nanoparticles at different concentrations.

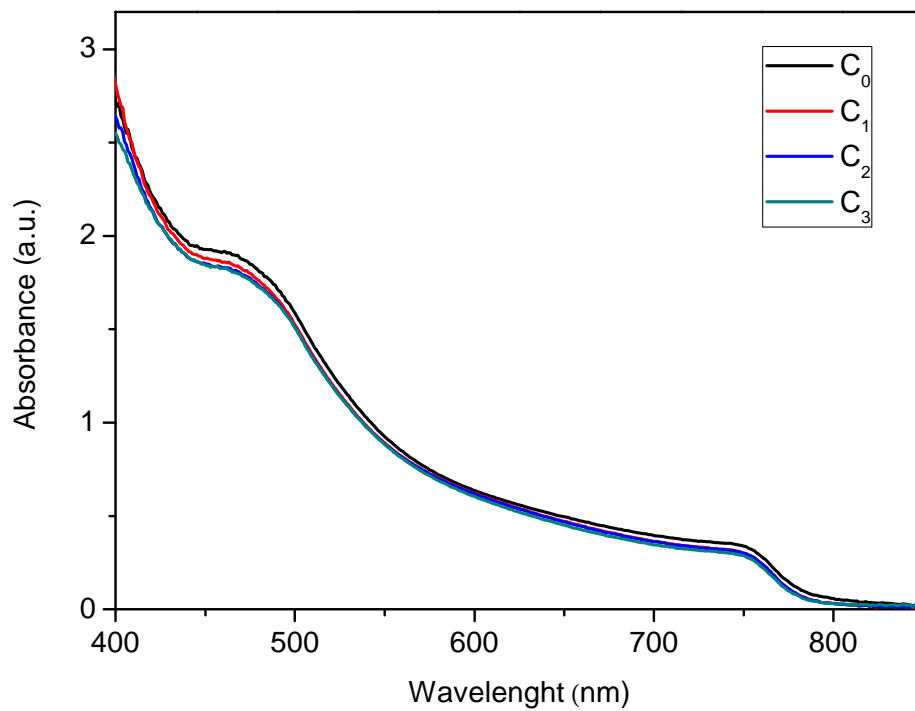


Figure 5.5 Absorption spectra of samples glass/ITO/PEDOT:PSS + Au@PVP nanoparticles/CH₃NH₃PbI₃ with different concentrations of Au@PVP nanoparticles in PEDOT:PSS.

By observing figure 5.5, relative to the samples glass/ITO/PEDOT:PSS + Au@PVP nanoparticles/ $\text{CH}_3\text{NH}_3\text{PbI}_3$, it is evident that the incorporation of the nanoparticles does not produce any enhancement of light absorption of the cells. This means that the absorption of the active layer is not influenced by the near-field of the nanoparticles or that its contribution is extremely low compared to the intrinsic absorption of the perovskite. From the electrical characterizations it can be concluded that increasing the concentration of nanoparticles in PEDOT:PSS to obtain more intense plasmonic effects is not advantageous for improving cell efficiencies, because competitive detrimental electrical effects reduce their performances.

To investigate if the effects of the nanoparticles were not evident due to the strong absorption of the perovskite, it was thought to reduce the thickness of the active layer of the cells. A preliminary study to optimize the active layer deposition using a 20 wt% $\text{CH}_3\text{NH}_3\text{PbI}_3$ precursor solution was made adapting the deposition parameters used for the 30 wt% $\text{CH}_3\text{NH}_3\text{PbI}_3$ precursor solution. Afterwards, reference solar cells without nanoparticles were made following the procedure reported in paragraph 5.2.1, with the exceptions just described. The fabricated solar devices showed very low efficiencies and several ones were short circuited. Moreover, no reproducibility was observed in a further set of devices fabricated. It was deduced, therefore, that the cause could be the low quality of the perovskite films obtained on the PEDOT:PSS. The incomplete perovskite coverage on PEDOT:PSS and the presence of voids in very thin active layer made the devices more susceptible to short circuit problems.

The crystal growth of the perovskite is strongly dependent on the composition and properties of the substrate on which it is deposited^[1,2]. In different works reported in literature^[3,4] the perovskite films deposited on PEDOT:PSS show pinholes or an incomplete surface coverage that lead to lower device performances. Moreover, the deposition of the perovskite on PEDOT:PSS produce grains of reduced size with respect to other substrates^[5] resulting in a higher density of grain boundaries. In these sites charge accumulations can occur resulting in potential barriers that reduce the current extraction.

In order to improve the quality of the thin films of perovskite, it was thought to replace the PEDOT:PSS with a different hole transport material (HTM), also considering that the use of PEDOT:PSS has different disadvantages. PEDOT:PSS is not an efficient electron-blocking material, since it has numerous intergap states that enhance recombination at the interface

with the active layer, determining an increase of the leakage currents^[6]. Furthermore, its hygroscopicity and acidity constitute limiting factors for the stability of the devices.

Among the several HTM used as alternative to the PEDOT:PSS^[7], it was chosen to adopt the poly-TPD. Since it has a LUMO level value of -2.4 eV ^[8], poly-TPD can efficiently block the electrons generated in the perovskite. Moreover, thanks to its hydrophobic nature, it preserves the perovskite from moisture damage. In literature, it was reported the deposition of high quality perovskite films on the poly-TPD through thermal evaporation method^[9]. Solution based deposition methods also permit to obtain good results^[5]. However, because the wettability of the perovskite precursor solution on a hydrophobic surface could not be optimal, a poly-TPD film pre-treatment aimed to make its surface hydrophilic could be necessary. To prevent the damaging of the poly-TPD layer the hydrophilicizing process must be bland. The use of poly-TPD does not allow the integration of Au@PVP nanoparticles within the HTL of the cells because it is soluble only in apolar solvents, such as CB, in which the nanoparticles are instable. However, this is not a limit because solvents used to disperse the nanoparticles do not dissolve the poly-TPD and therefore the Au@PVP nanoparticles can be deposited on its surface by spin coating without damaging it.

5.3 Plasmonic perovskite solar cells integrating anisotropic Au@PVP nanoparticles at the poly-TPD/perovskite interface

A preliminary optimization of the fabrication of a reference device glass/ITO/poly-TPD/CH₃NH₃PbI₂Br/PC₆₁BM/BCP/Al was necessary before the manufacture of plasmonic solar cells integrating Au@PVP nanoparticles at the poly-TPD/perovskite interface.

5.3.1 Device fabrication

ITO-coated glass substrates 4L etched (Visiotech) were sequentially cleaned by ultrasonication in deionized water, 2-propanol and acetone for 10 minutes. Substrates were immerse in a mixture of hydrogen peroxide (H₂O₂), ammonia (NH₃) and ultrapure water (1:1:5 v/v) at 80 °C for 10 minutes in order to remove organic contamination, then rinsed ten times in water prior next depositions.

Poly-TPD (Lumtec LT-N149 MW > 20 KDa) solution in chlorobenzene (2.5 mg/mL), previously prepared, was spin coated at 4000 rpm for 30 s on the substrates, that were subsequently annealed at 150 °C for 30 min and UV-irradiated for 30 min to promote the poly-TPD cross-linking.

Immediately before the deposition of the perovskite film, each substrate was subject to air plasma (Diener Electronics) treatment for 26 s with variable power intensity in the range 10-60%. As a reference, a sample was not treated with plasma. All samples were transferred to a nitrogen filled glovebox to complete the fabrication of the devices. A perovskite precursor solution 30 wt% was previously prepared by dissolving 461 mg of PbI₂ and 112 mg of methylammonium bromide (CH₃NH₃Br, >99%, dyesol) in 1.33 mL of dimethylformamide (DMF) with 71 µL of DMSO and stirring for 4 h. The solution was spin coated onto poly-TPD film at 4000 rpm for 200 s, with a dripping of toluene after 10 s from the beginning of the rotation. The samples were annealed at 100 °C for 10 minutes and then allowed to cool to room temperature. A solution previously prepared dissolving 25 mg of PC₆₁BM in 1 mL chlorobenzene was spin-coated on the perovskite layer at 1000 rpm for 60 s. Then, a BCP solution 0.5 mg/mL in 2-propanol, was spin coated at 6000 rpm for 20 s. Finally, 100 nm of Al were thermally evaporated at a pressure of 5×10^{-6} mbar to form the back contact of the devices. The devices were characterized under an irradiance of 1000 W/m² at air mass (AM) 1.5G.

5.3.2 Characterization and results

Representative J-V curves of the devices resulting from the electrical characterizations are shown in figure 5.6.

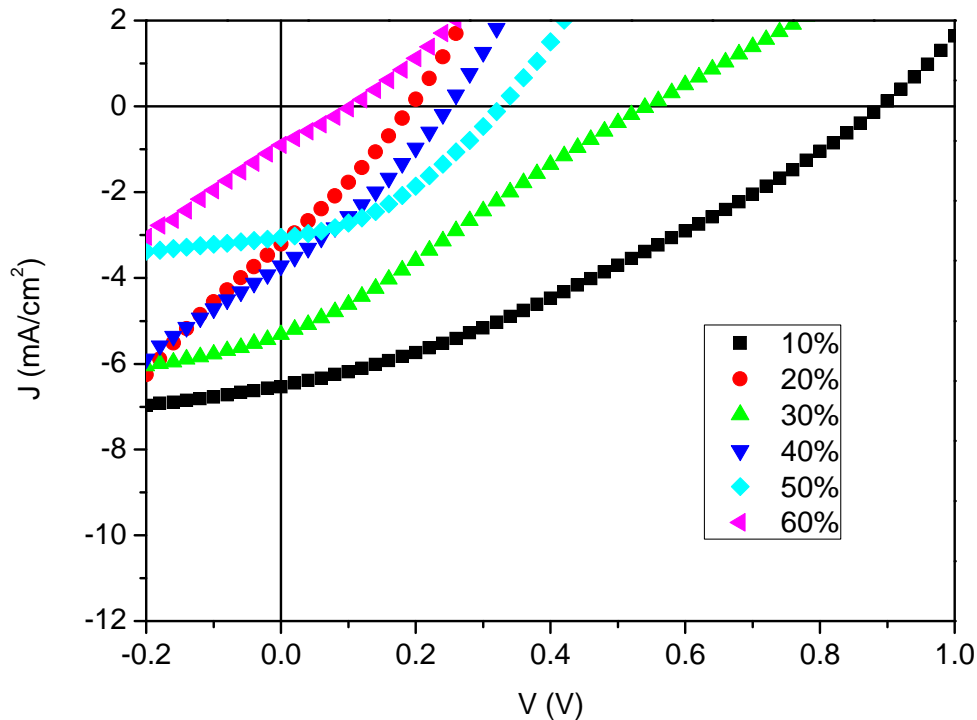


Figure 5.6 Representative J-V curves of the devices glass/ITO/poly-TPD/ $\text{CH}_3\text{NH}_3\text{PbI}_2\text{Br}$ /PC₆₁BM/BCP/Al in which poly-TPD was treated with air plasma at variable power intensity in the range 10-60%.

The curve relative to the sample without plasma treatment was not reported because it was not possible to obtain a perovskite film due the high hydrophobicity of the poly-TPD.

The devices with the best performances are those obtained using poly-TPD treated for 26 s with air plasma at a power intensity of 10%. However such devices exhibit a high series resistance as can be observed from the characteristic curves. This could be due to the possible degradation of the poly-TPD as effect of the plasma treatment. On the other hand, the power of the plasma could not be further reduced otherwise its uniformity was not guaranteed. Furthermore, it was not possible to set a plasma time shorter than 26 seconds. Another possible explanation of the results could be that the poly-TPD used has a low average molecular weight, so it could be damaged by the solvent during the perovskite deposition^[10].

It was decided, therefore, to use a poly-TPD with a higher average molecular weight (poly-TPD SOL2420H, MW= 80-150 KDa). In this case, good quality perovskite films were obtained

directly on annealed and UV-treated poly-TPD films without the need for plasma treatment. To investigate the effects of the incorporation of Au@PVP nanoparticles at the poly-TPD/perovskite interface, Au@PVP nanoparticles with different average sizes, called Au@PVP_S and Au@PVP_L were synthesized using 45 and 15 μL of H_2O_2 during the growth step. Moreover, to study how the solvent used to disperse the nanoparticles affect the device performances, each Au@PVP nanoparticle dispersion was divided in two aliquots, which were purified, following the procedure described in paragraph 3.2.2 using ethanol and water as solvents. In this way it was possible to obtain for both Au@PVP_S and Au@PVP_L two different dispersions, one in ethanol and the other in water. The nanoparticles had a concentration of 1.24×10^{12} nanoparticles/mL. The integration of the nanoparticles at the poly-TPD/perovskite interface was achieved by spin coating 100 μL of the Au@PVP dispersions on the poly-TPD film at 1200 rpm for 60 s. The samples were subsequently annealed for 5 min at 150 $^\circ\text{C}$ in order to remove the solvent. The devices were completed following the procedure described above. As references, solar cells were made using poly-TPD films on which pure ethanol or pure water, instead of the nanoparticles dispersion, was spin coated.

Table 5.2 summarizes the photovoltaic parameters of the fabricated devices, while in figure 5.7 are reported their representative J-V curves.

Table 5.2 Summary of the average photovoltaic parameters of the devices glass/ITO/poly-TPD/(nanoparticles)/ $\text{CH}_3\text{NH}_3\text{PbI}_2\text{Br}$ (30 wt%)/ PC_{61}BM /BCP/Al obtained integrating Au@PVP_L and Au@PVP_S nanoparticles dispersed in water and ethanol at the poly-TPD/perovskite interface. Each value represents the average of 8 replicates.

Device	Description	FF	V_{oc} (V)	$-J_{sc}$ (mA/cm^2)	PCE (%)
M_{REF_W}	Poly-TPD + water	0.48 ± 0.04	1.06 ± 0.03	16.12 ± 0.36	8.09 ± 0.39
M1	Poly-TPD + Au@PVP_S in water	0.49 ± 0.03	1.03 ± 0.02	15.78 ± 0.43	7.97 ± 0.41
M2	Poly-TPD + Au@PVP_L in water	0.52 ± 0.04	0.97 ± 0.03	16.02 ± 0.37	8.05 ± 0.34
M_{REF_ET}	Poly-TPD + ethanol	0.62 ± 0.03	1.10 ± 0.02	12.90 ± 0.39	8.81 ± 0.38
M3	Poly-TPD + Au@PVP_S in ethanol	0.60 ± 0.03	1.11 ± 0.03	17.61 ± 0.40	11.75 ± 0.36
M4	Poly-TPD + Au@PVP_L in ethanol	0.55 ± 0.04	1.10 ± 0.03	16.23 ± 0.42	9.72 ± 0.39

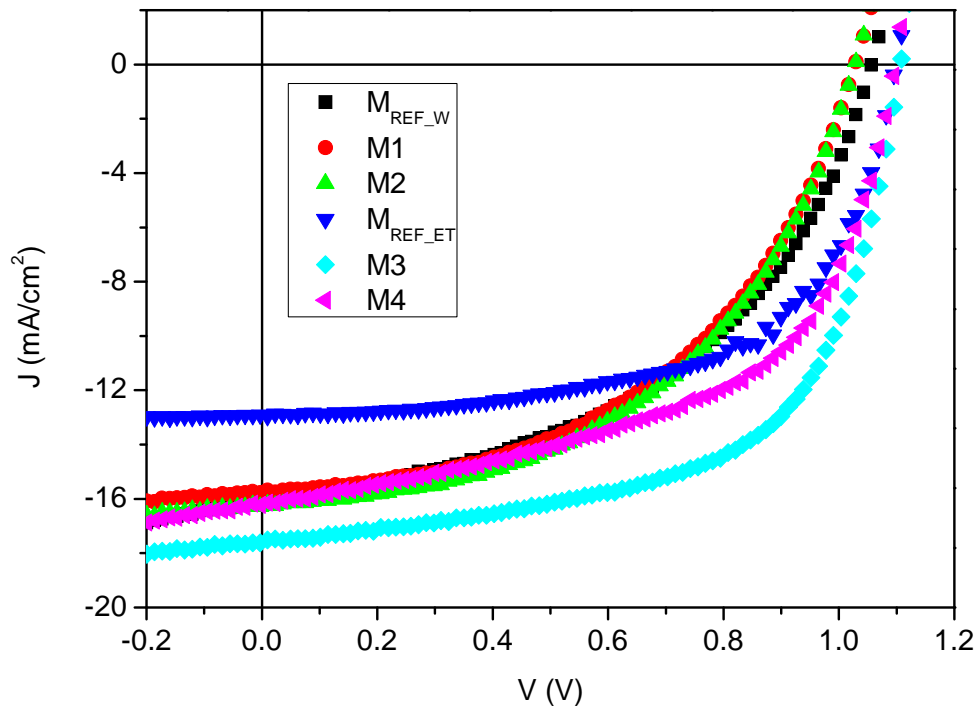


Figure 5.7 Representative J-V curves of the devices glass/ITO/poly-TPD/(nanoparticles)/CH₃NH₃PbI₂Br (30wt%)/PC₆₁BM/BCP/Al obtained integrating Au@PVP_L and Au@PVP_S nanoparticles dispersed in water and ethanol at the poly-TPD/perovskite interface.

It is evident that the plasmonic devices obtained using aqueous dispersions of Au@PVP nanoparticles do not show any improvement with respect to the reference device. On the other hand, when Au@PVP nanoparticles are deposited on poly-TPD from dispersions in ethanol, the performances of the devices are notably improved compared to that of the reference device. In particular, in the case of Au@PVP_S an efficiency enhancement of about 33% was observed, while for Au@PVP_L the increase is of about 10%. The incorporation of the nanoparticles leads in both cases to a remarkable enhancement of the J_{SC} value. The V_{OC} is not affected by the presence of nanoparticles, while the FF decreases in plasmonic devices. The FF reduction is more significant in devices with Au@PVP_L nanoparticles with respect to those integrating Au@PVP_S nanoparticles.

Following the procedure described above, a further set of devices was made with the aim to investigate the effects of the incorporation of plasmonic nanoparticles in solar cells with a reduced thickness of the perovskite active layer. In this case a 20 wt% CH₃NH₃PbI₂Br precursor solution was used. Table 5.3 summarizes the photovoltaic parameters of the fabricated devices, while in figure 5.8 are reported their representative J-V curves.

Table 5.3 Summary of the average photovoltaic parameters of the devices glass/ITO/poly-TPD/(nanoparticles)/CH₃NH₃PbI₂Br (20 wt%)/PC₆₁BM/BCP/Al obtained integrating Au@PVP_L and Au@PVP_S nanoparticles dispersed in water and ethanol at the poly-TPD/perovskite interface. Each value represents the average of 8 replicates.

Device	Description	FF	V _{oc} (V)	-J _{sc} (mA/cm ²)	PCE (%)
N _{REF_W}	Poly-TPD + water	0.52 ± 0.03	0.97 ± 0.02	12.02 ± 0.38	6.04 ± 0.43
N1	Poly-TPD + Au@PVP_S in water	0.51 ± 0.03	1.07 ± 0.03	10.04 ± 0.42	5.43 ± 0.45
N2	Poly-TPD + Au@PVP_L in water	0.48 ± 0.03	1.06 ± 0.02	12.09 ± 0.40	6.07 ± 0.41
N _{REF_ET}	Poly-TPD + ethanol	0.43 ± 0.02	1.02 ± 0.03	12.74 ± 0.39	5.61 ± 0.37
N3	Poly-TPD + Au@PVP_S in ethanol	0.62 ± 0.03	1.07 ± 0.03	14.68 ± 0.36	9.73 ± 0.36
N4	Poly-TPD + Au@PVP_L in ethanol	0.64 ± 0.03	1.01 ± 0.04	12.68 ± 0.40	8.14 ± 0.39

As observed for the previous set of solar devices, also in this case the use of aqueous dispersions for the integration of Au@PVP nanoparticles at poly-TPD/perovskite interface have not produced any improvement in cell performances.

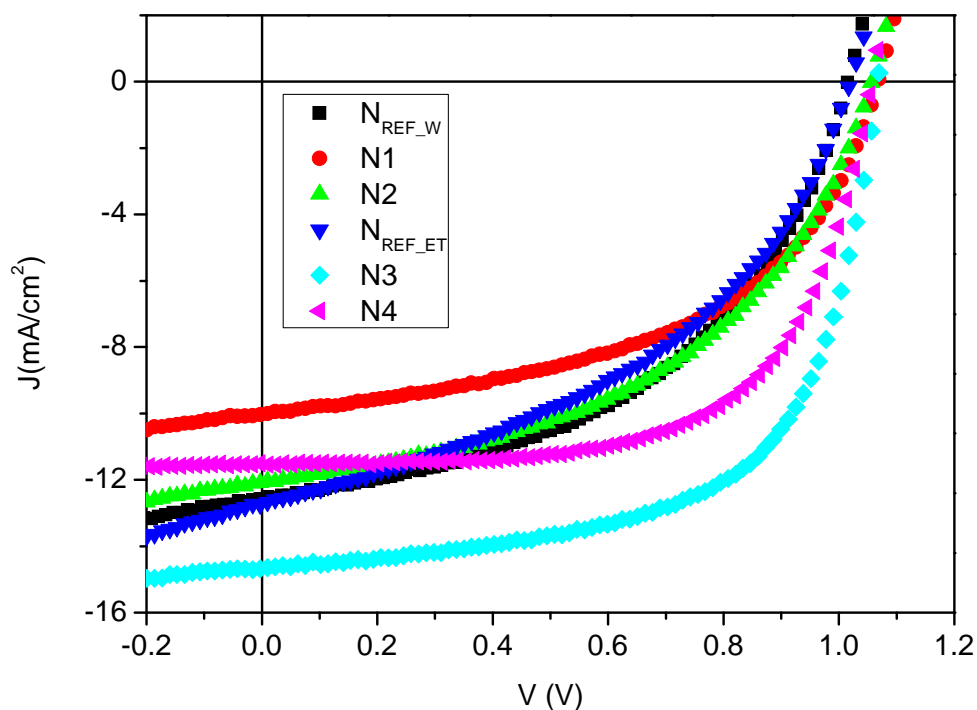


Figure 5.8 Representative J-V curves of the devices glass/ITO/poly-TPD/(nanoparticles)/CH₃NH₃PbI₂Br (20wt%)/PC₆₁BM/BCP/Al obtained integrating Au@PVP_L and Au@PVP_S nanoparticles dispersed in water and ethanol at the poly-TPD/perovskite interface.

On the other hand, the deposition of Au@PVP nanoparticles dispersed in ethanol has permit to greatly increase the efficiency of the devices. An efficiency enhancement of about 73% was obtained through the incorporation of Au@PVP_S nanoparticles, while the improvement was of about 45% using Au@PVP_L nanoparticles. The deposition of Au@PVP_S and Au@PVP_L nanoparticles from ethanol dispersions produces a remarkably enhancement of the FF of the devices. In addition, for Au@PVP_S nanoparticles also a notable improvement of the J_{SC} was observed.

Optical, morphological and structural characterizations to establish the effects deriving from the integration of Au@PVP nanoparticles in perovskite solar cells are ongoing. In figure 5.9 are reported the first SEM analysis achieved on samples glass/ITO/poly-TPD (+ water or Au@PVP_S in water) and glass/ITO/poly-TPD (+ water or Au@PVP_S in water)/perovskite (30 wt%).

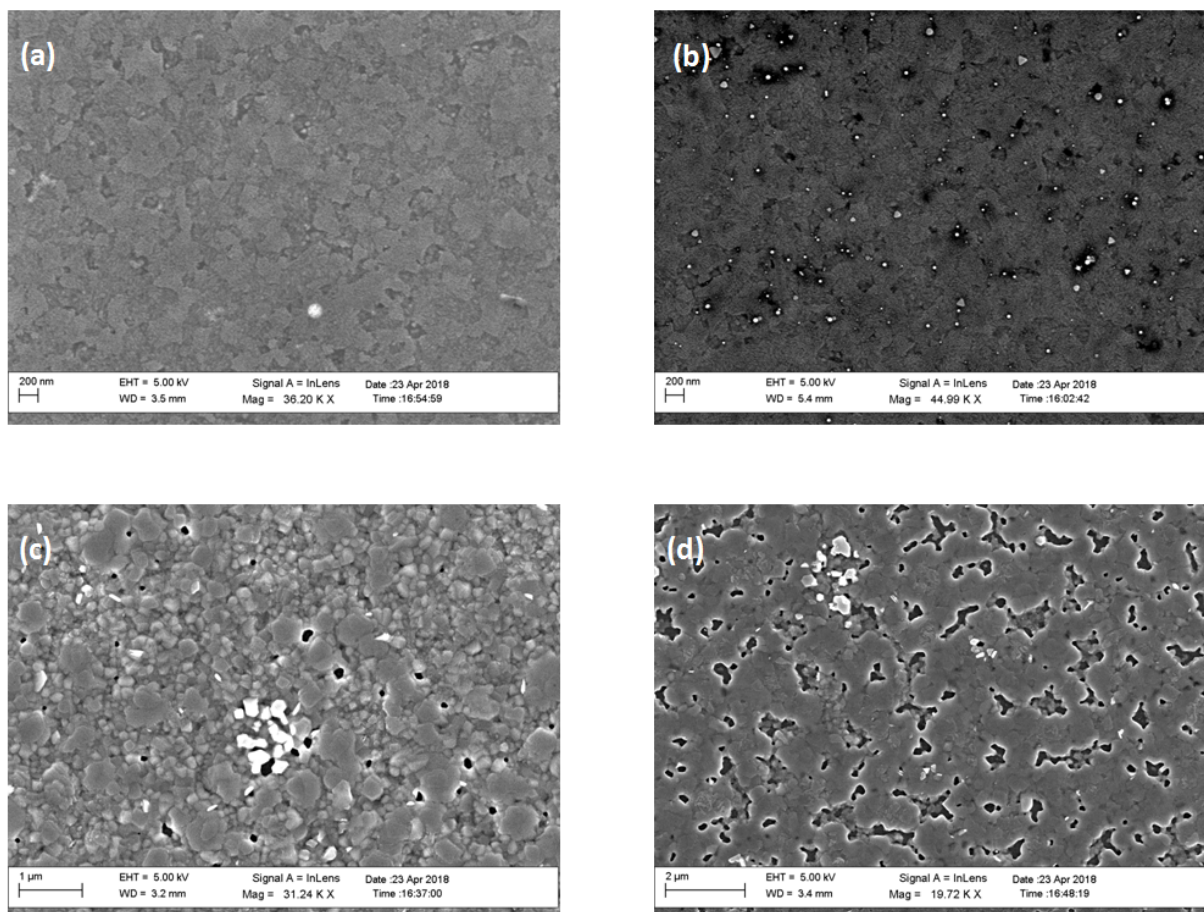


Figure 5.9 SEM micrographs of the samples glass/ITO/poly-TPD (+ water) (a), glass/ITO/ poly-TPD (+Au@PVP_S in water) (b), glass/ITO/poly-TPD (+ water)/ perovskite (30 wt%) (c), glass/ITO/poly-TPD (+ Au@PVP_S in water)/perovskite (30 wt%) (d).

It can be observed that the presence of the nanoparticles on poly-TPD leads to a perovskite film with larger grain cluster size with respect to the film obtained on poly-TPD on which only water was deposited. This could lead to an enhancement of the charge transport properties of the perovskite as a consequence of a reduced presence of grain boundaries. Moreover, Au@PVP_S nanoparticles on poly-TPD allow to obtain a perovskite film without voids, which are instead clearly evident in perovskite film deposited on poly-TPD treated with water. The nanoparticles could act as nucleating agents for the perovskite. In particular, the PVP on their surface could interact with the perovskite precursor improving the film crystallization. The larger crystal grains and the absence of voids should lead to an enhancement of the cell performances. However, from the electrical characterization no improvements were observed in devices in which Au@PVP nanoparticles were deposited from aqueous dispersions. Therefore, water could produce detrimental effects that counterbalance the beneficial effects deriving from the presence of the nanoparticles. The ongoing characterizations will permit to fully understand the effects produce from the integration of Au@PVP nanoparticles in perovskite solar cells and how the solvent in which they are dispersed affects the performance of the devices.

5.4 References

- [1] Z. K. Wang et al., Improved hole interfacial layer for planar perovskite solar cells with efficiency exceeding 15%. *ACS applied materials & interfaces*, **2015**, 7, 9645-9651.
- [2] Q. Chen et al., Planar heterojunction perovskite solar cells via vapor-assisted solution process. *Journal of the American Chemical Society*, **2013**, 136, 622-625.
- [3] S. Bai et al., Organometal halide perovskites for photovoltaic applications. *Advanced Functional Materials*, **2015**, 535-566.
- [4] J. You et al., Moisture assisted perovskite film growth for high performance solar cells. *Applied Physics Letters*, **2014**, 105, 183902.
- [5] D. Zhao et al., High-Efficiency Solution-Processed Planar Perovskite Solar Cells with a Polymer Hole Transport Layer. *Advanced Energy Materials*, **2015**, 5, 1401855.
- [6] K. Tvingstedt et al., Removing Leakage and Surface Recombination in Planar Perovskite Solar Cells. *ACS Energy Letters*, **2017**, 2, 424-430.
- [7] T. Liu et al., Inverted perovskite solar cells: progresses and perspectives. *Advanced Energy Materials*, **2016**, 6, 1600457.
- [8] O. Malinkiewicz et al., Metal-Oxide-Free Methylammonium Lead Iodide Perovskite-Based Solar Cells: the Influence of Organic Charge Transport Layers. *Advanced Energy Materials*, **2014**, 4, 1400345.
- [9] O. Malinkiewicz et al., Perovskite solar cells employing organic charge-transport layers. *Nature Photonics*, **2014**, 8, 128.
- [10] M. J. Jo et al., Effect of Poly-TPD Molecular Weight on the Characteristics of Quantum-Dot Light-Emitting Devices. *Journal of Nanoscience and Nanotechnology*, **2015**, 15, 5066-5069.

Chapter 6

Conclusions and future works

Organic and perovskite solar cells are particularly interesting photovoltaic technologies for their potential to overcome the traditional silicon-based photovoltaic devices, whose diffusion has been limited by the high costs of production. The use of cheap semiconductors with optical and electrical properties that can be modified by changing their chemical composition, the fabrication through solutions-based and low temperature processes compatible with roll-to-roll techniques also on flexible substrates, the possibility to obtain semitransparent cells, make them particularly attractive for the reduced production costs and for the extension of their applications, like in portable devices or for building integration. For these reasons, the research efforts aim to improve these alternative photovoltaic technologies, by developing strategies that permit to increase the low efficiency of organic solar cells, limited, among other causes, by the poor light absorption of the thin active layer, and to reduce the presence of toxic lead in perovskite solar cells while preserving their high efficiencies.

The integration of plasmonic nanoparticles in solar cells is an effective and versatile method to enhance their light trapping ability exploiting plasmonic effects such as light scattering and near-field enhancement, without the need to increase the thickness of the active layer. This is particularly useful for organic solar cells, in which the thickness of the active layer is limited by the low charge mobility and the short exciton diffusion length of organic semiconductors. On the other hand, the incorporation of nanoparticles in perovskite solar cells could allow to compensate the light absorption losses in devices fabricated with a very thin active layer with the aim to reduce the lead content.

In this thesis, appropriately synthesized plasmonic anisotropic gold nanoplates were integrated in organic and perovskite solar cells and their effects on the properties and performances of the devices were investigated. The choice to employ this typology of nanoparticles derives from their particular plasmonic properties and the possibility to be incorporated in the cells with a minimal morphological disturbance to their multilayer thin

film structures. Moreover, to the best of our knowledge, the application of gold nanoplates in organic and perovskite solar cells had never been reported.

In the first part of the thesis, the synthesis and characterization of gold nanoplates sterically stabilized by a polyvinylpyrrolidone coating (Au@PVP) were accomplished. The nanoparticles, obtained through a seed-mediated synthetic protocol, had prevalently a form of triangular nanoplates with a wide size distribution, but also hexagonal nanoplates and small nanospheres were present among the products. Multiple plasmonic bands with a large bandwidths appeared in the absorption spectra of the nanoparticles due to their anisotropic shapes and size distribution. By changing the concentration of the reactants, it was possible to tune the average size of the nanoparticles and to adapt their properties to the particular solar devices in which they have been integrated.

Metallic nanoparticles in contact with the active layer of solar devices can lead to exciton quenching or act as charge recombination centers if they are not electrically insulated. For these reasons, a procedure to cover the Au@PVP nanoparticles with an insulating silica shell was implemented adapting the conditions of the Stöber method and exploiting the ability of the PVP to act as a primer. Since the near-field decays with the distance from the surface of the nanoparticles, the lowest thickness of the shell sufficient to insulate the metallic core was required. Numerous experiments were performed to establish the optimal conditions for the formation of a thin silica shell around the Au@PVP nanoparticles and for the subsequent purification of the products.

In the second part of the work, the fabrication of organic solar cells with the structure glass/ITO/PEDOT:PSS/P3HT:PC₆₁BM/Al was optimized, before the integration of the plasmonic nanoparticles, to obtain reproducible reference device. The nanoparticles have been initially added to the PEDOT:PSS dispersion before its deposition. However, the plasmonic devices showed lower performance compared to the reference. It was observed that increasing the concentration of the dispersion of nanoparticles, before its addition to PEDOT:PSS dispersion, permitted to obtain plasmonic devices with performance slightly better than the reference, probably because in this way the concentration of PEDOT:PSS dispersion was only slightly changed. Therefore, a study was conducted on the effects of the nanoparticles, added at different concentration in PEDOT:PSS, on the properties and performances of the solar cells. The device efficiencies increased with the concentration of the nanoparticles up to an optimal concentration, beyond which a decrease of the overall

performances was observed. This trend was justified by the fact that the nanoparticles integrated in the cells produced optical, electrical and morphological effects. Therefore, although the light harvesting increased with the nanoparticles concentration due to their plasmonic effects, over the optimal concentration electrical and morphological effects determined a lowering of the cells performance. At the optimal concentration an efficiency enhancement of about 15% was obtained respect to the reference device.

The Au@PVP nanoparticles have been subsequently deposited at the PEDOT:PSS/P3HT:PC₆₁BM interface, in order to increase the influence of the near-field on the active layer. The obtained plasmonic devices showed notable lower performances respect to the reference and the reason was identified in the insufficient electrical insulation of the gold core by the PVP coating. In a further study, Au@SiO₂ nanoparticles with a thin silica shell (average thickness of about 3 nm) were integrated at the interface but, although an ameliorating effect was observed respect to the Au@PVP nanoparticles, the electrical insulation was not still optimal.

An interesting prosecution of this study could be the investigation of the effects produced by Au@SiO₂ nanoparticles with thicker silica shells, in order to identify the minimal thickness required to efficiently insulate the metallic core in such a way to maximize the exploitation of the plasmonic properties of the nanoparticles in solar cells. Moreover, another interesting proposal could be the assembly of a set-up for the EQE measurement of the devices that permits to perform their characterization simulating the real operating conditions through a white light background source. In this way, in presence of the light bias, plasmons are excited and their effects on the extracted current at the different wavelengths can be studied.

In the third part, Au@PVP nanoparticles have been integrated at different concentrations in the HTL of an inverted perovskite solar cells with a structure glass/ITO/PEDOT:PSS/CH₃NH₃PbI_{3-x}Br_x/PC₆₁BM/BCP/Al. However, probably due to the high intrinsic absorption of perovskite, no improvement effects were observed either in the performance of the devices or in the light absorption of the active layers. For this reason, it was decided to move to thinner perovskite layers, even with the aim of obtaining semi-transparent devices. To get proper thin perovskite layers it has been necessary to replace the PEDOT:PSS with poly-TPD, a HTL commonly used in inverted perovskite cells. Due to the instability of Au@PVP nanoparticles in the solvent of the poly-TPD, the integration within it

was not possible. Instead, Au@PVP dispersions in ethanol and water were deposited on poly-TPD and the corresponding devices were fabricated. While the deposition of Au@PVP nanoparticles from water dispersion did not produce ameliorating effects in cell performances, a significant increase was observed in the devices integrating the nanoparticles deposited from ethanolic dispersion. Moreover, the efficiency enhancement increased by thinning the thickness of the active layer. In the best cases an efficiency enhancement of 33% e 73% were observed in plasmonic devices with the thicker and thinner active layers, respectively. The results obtained were particularly interesting because, in contrast with those relative to the organic solar cells in which Au@PVP nanoparticles were integrated at the PEDOT:PSS/P3HT:PC₆₁BM interface, no detrimental effects deriving from the low insulating ability of the PVP coating were observed.

The first SEM characterizations have shown that the nanoparticles led to an improvement of the perovskite film quality; in particular, larger grain size and absence of voids were observed respect to the film deposited on the poly-TPD without nanoparticles. These effects determinate an increase of diffusion length of charge transport in the perovskites and a reduction of the shunting paths, justifying the improved FF of the devices. Further investigations are required to explain the optical effects due to the nanoparticles and to discriminate if the increased valued of J_{sc} is related to plasmonic effects or a greater light absorption of the perovskite as a consequence of improved film quality. Also in this case, the possibility to perform EQE measurements with a light bias could provide useful information to identify the mechanisms involved in the efficiency enhancement.

Further studies could regard the deposition of Au@SiO₂ nanoparticles at the poly-TPD/perovskite interface with the aim to compare the results with those relative to the Au@PVP and to understand the role of nanoparticle coatings in the performance of the cells.

List of publications and conference presentation

Publications

- A. Servidio, R. Lento, L. Ricciardi, M. La Deda, A. Golemme and R. Termine, "Enhancement of organic solar cells efficiency by embedding plasmonic anisotropic gold nanoparticles in the hole transport layer", manuscript in preparation.
- A. Servidio, S. Masi, A. Rizzo, L. Ricciardi, M. La Deda, A. Golemme and R. Termine, "Optical, electrical and morphological effects of anisotropic gold nanoparticles integrated at the hole transport layer/active layer interface of perovskite solar cells", manuscript in preparation.

Poster presentations

- A. Servidio, R. Lento, L. Ricciardi, M. La Deda, F. Cofone, A. Golemme, R. Termine, "Enhancement of organic solar cells efficiency by plasmonic gold nanoplates embedded in the hole transport layer". *Novel Optical Materials and Applications - NOMA 2017*, June 2017, Cetraro (CS), Italy.
- A. Servidio, R. Lento, L. Ricciardi, M. La Deda, F. Cofone, A. Golemme, R. Termine, "Increasing Organic Solar Cells (OSCs) efficiency through plasmonic anisotropic gold nanoparticles incorporated in the hole transport layer". *Plasmonica 2017*, July 2017, Lecce (LE), Italy.